University of Bologna

Department of Electronics, Computer Science and Systems

XXIV PhD. Course in Electronics, Computer Science, and Telecommunications

ING-INF/03, 09/F2

Spectrum Management and Cognitive Radios

by

Alessandro Guidotti

Coordinator:
Prof. **Luca Benini**

Advisor:
Prof. **Giovanni Emanuele Corazza**

Co-advisor:
Ing. **Guido Riva**

March 2012

If we knew what it was we were doing,
it would not be called research, would it?

Albert Einstein

Contents

List of Figures

List of Tables

List of Acronyms

3GPP	3rd Generation Partnership Project
4G	4th Generation
AP	Access Point
APSK	Amplitude and Phase Shift Keying
ARPA	Agenzia Regionale Prevenzione e Ambiente dell'Emilia Romagna
ASEP	Average Symbol Error Probability
AWGN	Additive White Gaussian Noise
BS	Base Station
CCDF	Complementary Cumulative Distribution Function
CDF	Cumulative Distribution Function
CDMA	Code Division Multiple Access
CEPT	European Conference of Postal and Telecommunications Administrations
CPG PT-D	Conference Preparatory Group Project Team D
CR	Cognitive Radio
CSI	Channel State Information
CSTR	Cognitive Satellite Terrestrial Radio

DFS	Dynamic Frequency Selection
DSA	Dynamic Spectrum Access
DT	Detection Threshold
DVB-T	Digital Video Broadcasting - Terrestrial
ECC	Electronic Communications Committee
ERP	Effective Radiated Power
ETSI	European Telecommunications Standards Institute
FCC	Federal Communications Commission
GCQ	Gauss-Chebyshev Quadrature
GEO	Geostationary Earth Orbit
GPS	Global Positioning System
GS	Ground Station
HNM	Hidden Node Margin
HSTS	Hybrid Satellite-Terrestrial System
ICT	Information and Communication Technology
IEEE	Institute of Electrical and Electronic Engineers
IMT	International Mobile Telecommunications
INR	Interference-to-Noise-Ratio
ITU	International Telecommunication Union
ITU-R	ITU - Radiocommunication Sector
IR-UWB	Impulse Radio - UWB
LEO	Low Earth Orbit
Log-MGF	MGF of the Lognormal Power Sum
LOS	Line Of Sight

LP	Location Probability
LTE	Long Term Evolution
MAC	Medium Access Control
MEO	Medium Earth Orbit
MGF	Moment Generating Function
MPSK	M-ary Phase Shift Keying
MS	Mobile Station
Ofcom	UK Office of Communications
OFDM	Orthogonal Frequency Division Multiplexing
PAN	Personal Area Network
PC	Power Control
pdf	Probability Density Function
PGFL	Probability Generating Functional
PHY	Physical Layer
PMSE	Programme Making and Special Events
PP	Point Process
PPP	Poisson Point Process
PU	Primary User
QAM	Quadrature Amplitude Modulation
QoS	Quality of Service
QPSK	Quadrature Phase Shift Keying
REM	Radio Environment Map
ROC	Receiver Operating Characteristic
RPC	Reference Planning Configuration

SINR	Signal-to-Interference plus Noise-Ratio
SNR	Signal-to-Noise-Ratio
SU	Secondary User
TETRA	Terrestrial Trunked Radio
UE	User Equipment
UHF	Ultra High Frequency
UMTS	Universal Mobile Telecommunications System
UWB	Ultra Wide-Band
VHF	Very High Frequency
WRAN	Wireless Regional Area Network
WRC-07	World Radiocommunications Conference 2007

List of Symbols

$\lvert\cdot\rvert$	Lebesgue measure
$\lVert\cdot\rVert$	Norm
$\mathbf{1}(\mathrm{n})$	Unit function
$\alpha > 2$	Exponent of the power exponential-decaying path-loss law
$b_0, b_I > 1$	Exponents of the amplitude exponential-decaying path-loss law for the intended and interfering links, respectively
$b(x,r)$	$\left\{y \in \mathbb{R}^d : \lVert y-x\rVert \leq r\right\}$, d-dimensional ball centered in x with radius r
$b(x,r,t)$	$\left\{y \in \mathbb{R}^d : r \leq \lVert y-x\rVert \leq t\right\}$, d-dimensional annular region centered in x with inner radius t and outer radius $r < t$
$b_i, i = 1,\ldots,M$	Squared amplitudes of the modulation normalized symbols
$c_d \triangleq \lvert b(0,1)\rvert$	$\frac{\pi^{d/2}}{\Gamma\left(1+\frac{d}{2}\right)}$, volume of the d-dimensional ball centered in the origin with unit radius
$C(A \times Y)$	Campbell measure
$C^!(A \times Y)$	Reduced Campbell measure
csc	Cosecant function
d	Number of dimensions of the Euclidean space
D_i	Transmission delay of the i-th interferer at the intended receiver
$\delta_x(A)$	Dirac measure of the point x in the subset $A \subset \mathbb{R}^d$
$\mathbb{E}\{X\}$	Expectation of the random variable X
E_0, E_I	Energy per symbol of the intended and interfering transmitter, respectively
$\mathrm{E}_{\mathrm{med}}$	Median field strength
erf	Error function

erfc	Complementary error function
$f_X(x)$	Probability density function of the random variable X
$F_X(x)$	Cumulative Distribution Function of the random variable X
$\widehat{f}_X(s)$	Laplace transform of the pdf of X
$\widehat{F}_X(s)$	Laplace transform of the CDF of X
${}_1F_1(a;b;z)$	Kummer confluent hypergeometric function
${}_2F_1(a;b;c;z)$	Gauss' hypergeometric function
${}_pF_q(\mathbf{a}_p;\mathbf{b}_q;z)$	Generalized hypergeometric function
Φ	Point Process
Φ^p	Thinned Point Process with the thinning function p
G	Antenna gain
$G_{p,q}^{m,n}\left(z \middle\vert \begin{matrix}\mathbf{a_p}\\ \mathbf{b_q}\end{matrix}\right)$	Meijer-G function
$\mathcal{G}[\mu]$	Probability Generating Functional
γ_0, γ_I	SNR on the intended and interfering links, respectively
$\Gamma(x)$	Gamma function
$\Gamma(a,x)$	Upper incomplete Gamma function
$\gamma(a,x)$	Lower incomplete Gamma function
h	Complex channel gain
$\tilde{h} = h/\sqrt{\Omega}$	Normalized channel gain
$\mathcal{H}(\cdot)$	Heaviside function
$\mathcal{I}_\Phi$	Aggregate interference power of the PPP Φ
$\mathcal{I}(t)$	Bandpass aggregate interference of the PPP Φ
$\mathcal{I}$	Baseband aggregate interference of the PPP Φ
I_ν	Modified Bessel function of the 1st kind and order ν
$\Im$	Imaginary part
j	$\sqrt{-1}$
J_ν	Bessel function of the 1st kind and order ν
$\mathrm{K_M}$	Modulation factor
κ_0, κ_I	path-loss environment-dependent constants
$\ell : \mathbb{R}^d \to \mathbb{R}^+$	Path-loss law
$\mathcal{L}_X(s)$	Laplace functional of the random variable X
λ, Λ	Density and density measure of the PPP Φ, respectively
M	Multilevel modulation order
$\mathcal{M}_X(s)$	Moment Generating Function
$\mathcal{M}_{S^{(N_p)}}(p)$	Moment Generating Function of the Lognormal power sum
m_0, m_I	Nakagami-m fading parameter on the intended and interfering links, respectively

N_0	Noise spectral density
$\mathbb{P}\{A\}$	Probability of event A
$\mathbb{P}^x$	Palm distribution of the Point Process Φ
$\mathbb{P}^{!x}$	Reduced Palm distribution of the Point Process Φ
p	Transmisssion probability
p_c	Coverage probability
$\{\psi_1(t), \psi_2(t)\}$	Orthonormal base of a coeherent demodulator
$Poisson(W)$	Poisson process with parameter W
q_i	i-th realization of the binomial process describing the probability of transmission of the network nodes
$\mathbb{R}^d$	d-dimensional Euclidean space
R_0, R_i	Distance between the intended BS and the i-th interfering BS from the intended receiver, respectively
$\Re$	Real part
$\mathcal{R}$	Average achiveable rate
$\mathcal{S}(\delta, \beta, \gamma, \mu)$	Stable random variable with characteristic exponent δ, skew parameter β, dispersion parameter γ, and location parameter μ
$S^{(N_p)}$	Lognormal power sum
σ_N^2	AWGN power
σ_{log}	Lognormal fading standard deviation on the intended link
σ_I	Lognormal fading standard deviation on the interfering links
$\mathcal{U}$[A, B]	Uniform distribution on the set [A,B]
$u(t)$	Unit step function
$w(t)$	Bandpass noise signal
$\Omega = \mathbb{E}_{\lvert h\rvert^2}\left\{\lvert h\rvert^2\right\}$	Mean value of the complex channel gain

Introduction

This thesis is the outcome of the work performed within a Ph.D. course in telecommunications engineering. The main research topic is focused on spectrum management and cognitive radios.

Spectrum management, and all of its related challenges, were born in the summer of 1895, in Villa Griffone near the city of Bologna. Guglielmo Marconi, just 20 years old, transmitted a signal over a hill, at a distance of approximately 2.4 km. Mr. Mignani, a friend who was waiting on the other side of the hill, fired a shot into thin air as soon as the signal was received. That sound changed the world, and it told Marconi that his dream, one day, would have been realized: letting people all around the world communicate among them, at any time...a prophetic thought.

More than a century has passed since that shot, and the frequency spectrum used for the first time in 1895 has become one of the most valuable and scarce resources in the world. As a matter of facts, Marconi's first broadcast transmission was a point-to-point affair, from England to Nova Scotia. It was the radio equivalent of flying an airline's passengers across the Atlantic once at a time. Today, we pack radio waves into the air as tightly as economy seats on a 747, and actually we have no other choice. Wireless communications and Internet services have had a pervasive diffusion into our society, and they profoundly affected our everyday life. Furthermore, new technologies, like Wi-Fi, Bluetooth, WiMAX, LTE, keep coming along in what seems to be an unlimited plethora of wireless services.

In order to avoid interference among all these communication systems, the commonly used paradigm was that of splitting the available spectrum into fixed non-overlapping blocks, and assign each of them to a specific service. However, the ever increasing demand for new services from users who want high-quality, broadband and multimedia services while on the move, is straining the efficiency of this static

spectrum allocation approach, which leaves a significant percentage of frequencies unused. Among all the possible solutions to this problem, the following two are receiving most of the attention in the industrial, academical and regulatory environments: (i) implementing new technologies which are either capable of accessing the temporarily/locally unused bands without interfering with the licensed services on these bands, like Cognitive Radios, or permit a deeper exploitation of the available channels, like femto-cell based communications; or (ii) release some spectrum bands thanks to new services which provide a higher spectral efficiency, like the DVB-T, and allocate them to new wireless systems.

These two approaches in spectrum management are promising, but also introduce novel coexistence and interference management challenges to deal with. In particular, the deployment of devices such as Cognitive Radios or femto-cells, which are characterized by the inherent unplanned, irregular and random locations of the network nodes, require advanced mathematical techniques in order to explicitly model their spatial distribution. In such context, the system performance and its optimization are strongly dependent on this spatial configuration. Furthermore, the aggregate network interference generated by such systems on the licensed services is a crucial effect to be accurately investigated. On the other hand, allocating some released spectrum bands to other wireless services poses severe coexistence issues with all the pre-existing services on the same or adjacent spectrum bands.

Thesis Outline

In this thesis, the two above mentioned methodologies for better spectrum usage are investigated. In particular, the thesis outline is as follows:

- in Part I, Stochastic Geometry theory, which is introduced in Appendix A, is applied to the modeling of network interference generated by a cognitive network, in order to derive simple expressions of several performance metrics. In Chapter 1, the Moment Generating Function of the aggregate interference power is obtained in closed form for several network configuration and fading conditions. In Chapter 2, this MGF is used to find the coverage probability of a typical cognitive network with randomly located nodes. In Chapter 3, by using once again the previously derived MGF, a single-integral expression of the average achievable rate in a cognitive network is computed. Finally, in Chapter 4, the Average Symbol Error Probability of an intended cognitive network

in the presence of network interference is examined. This study is performed for both synchronous and asynchronous systems. It is worthwhile underlining that all these mathematical frameworks are applicable to generalized fading conditions and network configurations;

- in Part II, the focus is on the regulatory aspects of the two above outlined solutions to inefficient spectrum usage. In Chapter 5, coexistence and interference challenges between LTE mobile systems and the DVB-T service are analyzed, in order to cope with the new spectrum allocations decided by the Electronic Communications Committee, which made available the Digital Dividend bands (*i.e.* the bands released thanks to the switch from analogue to digital TV broadcasting) to mobile broadband services. In Chapter 6, some of the studies performed inside the regulatory activity of CEPT SE43 are presented, providing an estimation of the amount of spectrum potentially available to Cognitive Radios and a thorough analysis of the Hidden Node problem. For further details on these two concepts, the reader might refer to Appendix C. Finally, Chapter 7 provides a study on the extension of cognitive technologies to Hybrid Satellite Terrestrial Systems.

Original Contributions

The activities performed during the three years of this doctorate study led me to obtain original scientific contributions in several fields. With reference to the subjects of Part I, the main contributions are the following:

- derivation of a closed-form expression of the Moment Generating Function of the aggregate interference power, over Rayleigh, Nakagami-m and non fading channels for several network configurations [1];
- definition of mathematical frameworks, substantiated by extensive Monte Carlo simulations, providing the following metrics in cognitive networks over generalized fading channels:
  - a closed-form expression of the coverage probability. In previous works, remarkable results were obtained, leading to a single-integral expression over Rayleigh fading channels [22]. In the mathematical framework proposed in this thesis, a simple closed-form expression is obtained, which also allows to derive a closed-form of the Upper Bound [1];

  - a single-integral expression of the average achievable rate. This result is of notable importance, as in previous studies a three-fold integral expression was computed. Moreover, this framework is useful only for Rayleigh fading channels [22]. On the other hand, the mathematical framework obtained during my doctorate provides a single-integral expression, which can be easily computed via numerical integration. Furthermore, this formula is applicable to arbitrary fading distributions, rather than being useful for Rayleigh fading only [1, 2];
  - a single-integral expression of the Average Symbol Error Probability. Recently, an interesting framework applicable to many scenarios was proposed. However, this framework is semi-analytical and Monte Carlo methods are required to remove conditioning over network interference [23]. In my doctorate, moving from this work, a novel mathematical framework was obtained. In particular, it provides a single-integral expression of the ASEP subject to network interference and noise, which is exact and does not require lengthy Monte Carlo methods for its computation [3].

Regarding the coexistence of heterogeneous wireless communication systems, the most important contributions are:

- definition of a versatile methodology to take into account both the interference from a LTE mobile system towards a DVB-T system, and vice versa [4–9];
- study on the advantages in the use of the 800 MHz band for broadband wireless service, with respect to those at 2100 MHz and 2600 MHz [10];
- analysis of the potential amount of spectrum available for opportunistic access in an Italian region where the DVB-T system has already been deployed [11];
- analysis and characterization of the Hidden Node Margin, in order to properly identify the presence of licensed signals when deploying Cognitive Radio systems [12, 13];
- introduction of a 3-dimensional spectrum monitoring concept when considering cognitive functionalities in satellite-terrestrial systems [14].

It is worthwhile highlighting that the activities related to bullets 1-4 were performed inside European regulatory groups, CEPT SE43 and CPG PT-D, as Italian Administration representative.

Part I

Interference Modeling of Distributed Wireless Networks using Stochastic Geometry

A correct modeling of network interference is a key issue in current and next-generation networks, as it allows the study and the development of many fundamental techniques, like interference mitigation, the control of electromagnetic emissions, the design of communication systems, etc [23]. In particular, in cognitive radio networks, which envisage the deployment of different communication devices sharing the same spectrum, network interference is becoming the key dominant factor, as it significantly affects and severely degrades the achievable performance. This interference might be mitigated in systems with a centralized control, where the coordinator is able to assign different channelizations and power levels to the network nodes [24]. However, this is not possible in many emerging systems, like cognitive radio networks, where a centralized control is often not feasible, and there is the need for a distributed resource allocation. Moreover, the main requirement for a cognitive radio network is that it must not generate harmful interference on the primary users operating on the same frequencies. Network interference is thus a crucial aspect in the deployment of next-generation networks, in particular for cognitive radio networks, and its characterization is of critical importance.

When modeling network interference, there are three main factors which have to be taken into account: (i) the spatial distribution of the randomly located interferers in the network; (ii) the transmission characteristics of these interferers, *e.g.* modulation, power, activity, etc.; and (iii) the propagation characteristics of the wireless medium, *i.e.* path-loss, shadowing and multipath fading. The spatial location of the interferers might be modeled deterministically (*e.g.* using hexagonal grids), but this is possible only when the location of the nodes is known or it can be constrained to a fixed structure. This is not the case for cognitive radio networks, where the inherent unplanned, irregular, and random locations of secondary nodes require advanced mathematical techniques in order to explicitly model their spatial distribution. In this context, system performance and optimization depend critically on the spatial configurations of the nodes [25]. The analysis of such systems usually requires extensive, complex, and time-consuming system-level simulations to average over the spatial distributions of the network nodes. Thus, new "spatial average" performance metrics, which take into account the randomness of the spatial positions, are needed for a practical and pragmatic network planning, and a statistical modeling of the spatial locations of the interferers seems to better suite these requirements.

In this context, Stochastic Geometry has been shown to be a useful, powerful and flexible mathematical tool to address all these challenging problems. It is a

branch of applied probability strictly related to Point Processes theory, and its application to the modeling of communication networks is relatively new. In its simplest application, Stochastic Geometry consists in considering the network as a snapshot of a stationary random model in the Euclidean space, where the locations of the nodes are the realizations of a given Point Process [26]. This approach allows to estimate several spatial averages which provide the dependencies of some key network performance characteristics (*e.g.* coverage, rate, stability, etc.) as functions of a small number of parameters, like the density of the underlying Point Process or the parameters of the communication protocol being considered. Among all the possible node distribution models, the one in which nodes are distributed as a homogeneous Poisson Point Process is probably the most used, due to its complete spatial randomness and to its independence properties [22–32]. More recently, also Poisson Cluster Processes, *i.e.* processes where "parent nodes" are distributed as a Poisson Point Process with each of them being the center of a second process, have been introduced to model network interference [33, 34] in ad hoc networks.

In this Part, the application of Poisson Point Process theory to the characterization of network interference will be provided. In particular, the Moment Generating Function of the aggregate interference will be evaluated in closed form over generalized fading channels and in several network configurations. This function will be applied to the derivation of closed-form and single-integral expressions of coverage probability and average achievable rate respectively. Furthermore, a simple mathematical framework will be introduced for the computation of the Average Symbol Error Probability, for which a single-integral expression will be provided. For a short introduction to Point Process theory and Poisson Point Processes, the reader might refer to Annex A.

Chapter 1

Characterization of the Aggregate Interference Power

The modeling of wireless networks using Poisson Point Processes (PPP) is a recent research topic. However, it was shown in [24, 27] that interference in large wireless networks has strong similarities with *Shot Noise* processes, which have been deeply investigated in the past decades. Thanks to this similarity, several studies were performed in order to properly characterize the aggregate interference in those networks where nodes are randomly distributed, like cognitive radio networks. In particular, in [28] the authors provide an analysis of the probability of harmful interference towards primary receivers and the performance of cooperative spectrum sensing by deriving the characteristic function and the cumulants of the aggregate interference. In [29], these two functions are obtained for different spatial reuse protocols, showing that the aggregate interference follows a truncated-stable distribution. Finally, in [30], the authors study the distribution of the channel gain in a Poisson network of finite area, obtaining a closed-form expression of any moment of the interference. In the following, the focus will be on the Moment Generating Function (MGF) of the aggregate interference. More specifically, a comparison between aggregate interference and shot noise is provided. After this introduction, starting from the results obtained in [27, 31], a closed-form expression of the MGF of the aggregate interference over Nakagami-m, Rayleigh, and non fading channels and for different network deployments will be provided. The characterization of aggregate interference with the MGF will allow to introduce simple frameworks for the evaluation of several key network performance metrics in the following chapters.

1.1 System Model and Problem Statement

A cognitive wireless network in which nodes are distributed according to a homogeneous PPP Φ in the Euclidean space $\mathbb{R}^d$, with density λ, is considered. The focus will be on evaluating the aggregate interference power at a generic location $y \in \mathbb{R}^d$. Thanks to Slivnyak's theorem (Theorem A.3 in Section A.3), it can be assumed $y \equiv o$, where o is the origin of the space, without any loss of generality, as the distribution of a PPP is not affected by the choice of the measurement point. In this context, the aggregate interference power is given by:

$$\mathcal{I}_\Phi = \sum_{\mathbf{x}_i \in \Phi} q_i b_i |h_i|^2 = \sum_{\mathbf{x}_i \in \Phi} q_i b_i |\tilde{h}_i|^2 \ell(\|\mathbf{x}_i\|) = \sum_{\mathbf{x}_i \in \Phi} q_i b_i |\tilde{h}_i|^2 \|\mathbf{x}_i\|^{-\alpha} \tag{1.1}$$

where the following assumptions hold:

- all nodes are assumed to be in fixed positions, *i.e.* node mobility is not taken into account: the performance metrics obtained in this work are the result of "spatial averages" over the nodes' locations, where in each snapshot these locations correspond to a realization of the PPP Φ;

- nodes are equipped with omni-directional antennas, and they operate with the same constant transmit power P_T. The transmission power can thus be taken into account after the characterization of the aggregate interference, as it is a deterministic value;

- the path-loss law $\ell(\|\mathbf{x}\|)$ follows an exponential-decaying model with exponent α, and the path-loss exponent is assumed to be the same for all the links, *i.e.* $\ell(\|\mathbf{x}_i\|) = R_i^{-\alpha}$ with $R_i = \|\mathbf{x}_i\|$ being the distance between the i-th node and the origin. In order to have a finite value of the mean interference, it is further required that $\alpha > d$ [32, 35, 36]. It is worthwhile noting that this is a necessary but not sufficient condition for keeping $\mathbb{E}\{\mathcal{I}_\Phi\}$ finite;

- the complex channel gains h_i, for $\mathbf{x}_i \in \Phi$, follow a generic fading distribution, and $f_{|h_i|^2}(\cdot)$ denotes the probability density function (pdf) of the channel square envelope. $\tilde{h}_i = h_i/\sqrt{\Omega_i}$ denotes the normalized channel gain, with $\Omega_i = \mathbb{E}_{|h_i|^2}\left\{|h_i|^2\right\} = \ell(\|\mathbf{x}_i\|) = R_i^{-\alpha}$ being the mean square value of h_i;

- each node decides whether to transmit or not, independently from the other nodes, with probability p. Thus, the coefficients q_i, for $\mathbf{x}_i \in \Phi$, representing

this decision are the realizations of a binomial process Q with transmission probability p, and their pdf is given by:

$$f_q(q) = p\delta(q=1) + (1-p)\delta(q=0) \tag{1.2}$$

As stated in Section A.2, this preserves the Poisson law and simply affects the PPP density, which becomes $\lambda' = p\lambda$;

- in each time slot, each node transmits a randomly chosen symbol belonging to a M-ary Quadrature Amplitude Modulation (MQAM), M-ary Phase Shift Keying (MPSK) or Amplitude and Phase Shift Keying (APSK) modulation of order M. Let b_j, $j = 1, \ldots, M$ denote the squared amplitudes of the normalized symbols. These coefficients are uniformly distributed and their pdf is:

$$f_b(b) = \frac{1}{M}\sum_{j=1}^{M}\delta(b - b_j) \tag{1.3}$$

The modulation coefficient of the symbol transmitted by the i-th interferer will be denoted as b_i, for $\mathbf{x}_i \in \Phi$, with $b_i \in \{b_j\}_{j=1}^{M}$.

During the last years, many approaches based on the Moment Generating Function were proposed in order to evaluate some key performance metrics for wireless networks over generalized fading channels. In order to apply these approaches to cognitive networks modeled as Poisson Point Processes, the purpose of this chapter is the derivation of an analytically tractable expression of the MGF of the aggregate interference $\mathcal{I}_\Phi$ in (1.1), which is defined as:

$$\mathcal{M}_{\mathcal{I}_\Phi}(s) = \mathbb{E}_{\mathcal{I}_\Phi}\left\{e^{-s\mathcal{I}_\Phi}\right\} = \mathbb{E}_{q,b,|\tilde{h}|^2,\|\mathbf{x}\|}\left\{e^{-s\mathcal{I}_\Phi}\right\} \tag{1.4}$$

In the following, the concept of shot noise is introduced together with the results obtained in [24, 27, 31], which show how it can be easily used to obtain the MGF of the aggregate interference power generated by a d-dimensional Poisson network. Furthermore, it can be noticed that the above MGF is equal to the Laplace transform of the random variable $\mathcal{I}_\Phi$. This similarity will be used in order to compute the MGF using the same procedure provided in Section A.2 for the Laplace functional and the Probability Generating Functional (PGFL). Once the MGF of $\mathcal{I}_\Phi$ is obtained, this framework will be extended by obtaining a closed from expression over Nakagami-m, Rayleigh and non fading channels, and for several network deployments.

1.2 Interference as Shot Noise

The framework used to evaluate the MGF of $\mathcal{I}_\Phi$ is based on the similarities between aggregate interference and shot noise. 1D shot noise is generated by the excitement of a memoryless linear filter with a train of impulses derived from a homogeneous PPP with arrival rate λ [27, 31, 35]:

$$Y(t) = \sum_j g(k_j, t - t_j) \tag{1.5}$$

The sequence of arrival times t_j is a Poisson random variable with rate λ, and the coefficients k_j are i.i.d. random variables independent of t_j. The impulse function $g(k,t)$ is assumed to be integrable over $(-\infty, +\infty)$ in order to make the sum in (1.5) converge in distribution. In [27] the authors observed as the above expression is equivalent to that of the interference in a 1D Poisson network with a power-decaying law. Consider equation (1.1) and assume that both the coefficients b_i and q_i are identically equal to 1. If the impulse response in (1.5) follows a power-decaying law, *i.e.* $g(k_j, t-t_j) = k_j|t - t_j|^{-\alpha}$, and by switching from the time domain to the spatial one, then the shot noise amplitude at time $t = 0$ is the same as the interference measured at the origin [31].

1.3 Moment Generating Function

The application of the 1D shot noise framework to the computation of the MGF of a d-dimensional Poisson Point Process is straightforward. The MGF of the interference provided in equation (1.4) can be written as:

$$\mathcal{M}_{\mathcal{I}_\Phi}(s) = \mathbb{E}_{q,b,|\tilde{h}|^2,\|\mathbf{x}\|}\left\{e^{-s\sum_{\mathbf{x}_i\in\Phi}\mathcal{I}_{\Phi_i}}\right\} = \mathbb{E}_{q,b,|\tilde{h}|^2,\|\mathbf{x}\|}\left\{e^{-s\sum_{\mathbf{x}_i\in\Phi} q_i b_i |\tilde{h}_i|^2 \|\mathbf{x}_i\|^{-\alpha}}\right\} \tag{1.6}$$

where the single components of the aggregate interference $\mathcal{I}_{\Phi_i}$ are independent. Considering a network where nodes are distributed according to a PPP in a d-dimensional annular region $b(o, R_1, R_2)$ centered in the origin, with inner radius R_1 and outer radius R_2, the MGF of the aggregate interference power can be evaluated according to the following procedure:

1. conditioning of the MGF on having k nodes: as the terms $\mathcal{I}_{\Phi_i}$ are independent, the conditioned MGF can be written as the product of k MGFs. Moreover, since the nodes are uniformly distributed, each of these MGFs has the same

form, yielding to:

$$\mathcal{M}_{\mathcal{I}_\Phi}(s)|_k = \left\{\mathcal{M}_{\mathcal{I}_{\Phi_i}}(s)\right\}^k = \left\{\mathbb{E}_{q,b,|\tilde{h}|^2,\|\mathbf{x}\|}\left\{e^{-sq_ib_i|\tilde{h}_i|^2\|\mathbf{x}_i\|^{-\alpha}}\right\}\right\}^k \tag{1.7}$$

2. taking into account the generic i-th MGF $\mathcal{M}_{\mathcal{I}_{\Phi_i}}$ and the Euclidean space $\mathbb{R}^d$, the expectations on the coefficients b_i and q_i are solved;

3. when solving the expectation on the nodes' distribution, the same procedure as for the evaluation of the Laplace functional (see Section A.2) is followed: write the MGF over a bounded subset $A \subset \mathbb{R}^d$, and then consider an increasing sequence of bounded subsets $A_k \to \mathbb{R}^d$. Please note that before solving the resulting integral, the deconditioning on having k nodes is performed, and the integration bounds are restricted in order to consider the d-dimensional annular region $b(o, R_1, R_2)$ defined above;

4. finally, the expectation on the fading pdf according to the desired channel model, also considering particular values of R_1 and/or R_2 (*i.e.* accounting for different network deployment areas), can be solved.

Following steps $(1)-(2)$, the expectation of the i-th MGF $\mathcal{M}_{\mathcal{I}_{\Phi_i}}$ on the modulation square amplitudes, whose pdf is provided in equation (1.2), can be solved as:

$$\begin{aligned}
\mathbb{E}_b\left\{\exp\left(-sq_ib_i|\tilde{h}_i|^2\|\mathbf{x}_i\|^{-\alpha}\right)\right\} &= \int \exp\left(-sq_ib|\tilde{h}_i|^2\|\mathbf{x}_i\|^{-\alpha}\right) f_b(b)\mathrm{d}b \\
&= \int \exp\left(-sq_ib|\tilde{h}_i|^2\|\mathbf{x}_i\|^{-\alpha}\right) \frac{1}{M}\sum_{j=1}^{M}\delta(b-b_j)\mathrm{d}b \\
&= \frac{1}{M}\sum_{j=1}^{M}\exp\left(-sb_jq_i|\tilde{h}_i|^2\|\mathbf{x}_i\|^{-\alpha}\right)
\end{aligned}$$

and then, by solving also the expectation over the coefficients q_i with pdf given by equation (1.3):

$$\begin{aligned}
\mathbb{E}_q\left\{\frac{1}{M}\sum_{j=1}^{M}\exp\left(-sb_jq_i|\tilde{h}_i|^2\|\mathbf{x}_i\|^{-\alpha}\right)\right\} &= \frac{1}{M}\sum_{j=1}^{M}\int \exp\left(-sb_jq|\tilde{h}_i|^2\|\mathbf{x}_i\|^{-\alpha}\right) \\
&\quad \times \left[p\delta(q=1)+(1-p)\delta(q=0)\right]\mathrm{d}q \\
&= (1-p)+\frac{p}{M}\sum_{j=1}^{M}\exp\left(-sb_j|\tilde{h}_i|^2\|\mathbf{x}_i\|^{-\alpha}\right)
\end{aligned}$$

As stated in step (3), the expectation on the nodes distribution can be performed with the same approach as that used in Section A.2: as the nodes of a Poisson Point Process in a compact subset $A \subset \mathbb{R}^d$ are uniformly distributed according to the law $\mathbb{P}\{x \in \cdot\} = \Lambda(\cdot)/\Lambda(A)$, this expectation can be written as:

$$\mathbb{E}_{\|\mathbf{x}\|}\left\{(1-p)+\frac{p}{M}\sum_{j=1}^{M}\exp\left(-sb_j|\tilde{h}_i|^2\|\mathbf{x}_i\|^{-\alpha}\right)\right\} =$$

$$=\int_A\left((1-p)+\frac{p}{M}\sum_{j=1}^{M}\exp\left(-sb_j|\tilde{h}_i|^2\|\mathbf{x}\|^{-\alpha}\right)\right)\frac{\Lambda(\mathrm{d}\mathbf{x})}{\Lambda(A)}$$

Deconditioning on the number of nodes, the MGF on the compact set A is given by:

$$\begin{aligned}
\mathcal{M}_{\mathcal{I}_\Phi}|_A &= \exp\left(-\Lambda(A)\right)\sum_{k=0}^{\infty}\frac{\Lambda(A)^k}{k!} \\
&\quad\times\left\{\mathbb{E}_{|\tilde{h}|^2}\left\{\int_A\left((1-p)+\frac{p}{M}\sum_{j=1}^{M}\exp\left(-sb_j|\tilde{h}|^2\|\mathbf{x}\|^{-\alpha}\right)\right)\frac{\Lambda(\mathrm{d}\mathbf{x})}{\Lambda(A)}\right\}\right\}^k \\
&= \exp\left(-\Lambda(A)\right)\sum_{k=0}^{\infty}\frac{\Lambda(A)^k}{k!\Lambda(A)^k} \\
&\quad\times\left\{\int_A\left(1-p+\frac{p}{M}\sum_{j=1}^{M}\mathbb{E}_{|\tilde{h}|^2}\left\{\exp\left(-sb_j|\tilde{h}|^2\|\mathbf{x}\|^{-\alpha}\right)\right\}\right)\Lambda(\mathrm{d}\mathbf{x})\right\}^k \\
&= \exp\left\{-\int_A\left(1-\frac{1}{M}\sum_{j=1}^{M}\mathbb{E}_{|\tilde{h}|^2}\left\{\exp\left(-sb_j|\tilde{h}|^2\|\mathbf{x}\|^{-\alpha}\right)\right\}\right)p\Lambda(\mathrm{d}\mathbf{x})\right\}
\end{aligned}$$

where $e^{-\Lambda(A)} = e^{-\int_A \Lambda(\mathrm{d}\mathbf{x})}$ and the well know series $\sum_{k=0}^{\infty}\frac{t^k}{k!} = e^t$ was used. Considering an increasing sequence of bounded subsets $A_k \to \mathbb{R}^d$ and using the monotone convergence theorem, the MGF in equation (1.6) can thus be written as:

$$\mathcal{M}_{\mathcal{I}_\Phi}(s) = \exp\left\{\int_{b(o,R_1,R_2)}\left(1-\frac{1}{M}\sum_{j=1}^{M}\mathbb{E}_{|\tilde{h}|^2}\left\{\exp\left(-sb_j|\tilde{h}|^2\|\mathbf{x}\|^{-\alpha}\right)\right\}\right)p\Lambda(\mathrm{d}\mathbf{x})\right\} \tag{1.8}$$

where the integration bounds were restricted to the d-dimensional annular region $b(o, R_1, R_2)$. By switching the order of the integration with both the expectation

and the summation, (1.8) can be written as:

$$\begin{aligned}\mathcal{M}_{\mathcal{I}_\Phi}(s) &= \exp\left\{\frac{1}{M}\sum_{j=1}^{M}\mathbb{E}_{|\tilde{h}|^2}\left\{\int_{b(o,R_1,R_2)}\left(1-\exp\left(-sb_j|\tilde{h}|^2\|\mathbf{x}\|^{-\alpha}\right)\right)p\Lambda(\mathrm{d}\mathbf{x})\right\}\right\} \\ &= \exp\left\{\frac{1}{M}\sum_{j=1}^{M}\mathbb{E}_{|\tilde{h}|^2}\left\{p\lambda\underbrace{\int_{R_1}^{R_2}c_d d\left(1-\exp\left(-sb_j|\tilde{h}|^2 r^{-\alpha}\right)\right)r^{d-1}\mathrm{d}r}_{\mathcal{Z}(s)}\right\}\right\}\end{aligned} \tag{1.9}$$

where $c_d = |b(o,R_1,R_2)| = \pi^{d/2}/\Gamma\left(1+\frac{d}{2}\right)$ is the Lebesgue measure of $b(o,R_1,R_2)$. The integral $\mathcal{Z}(s)$ was solved in closed-form[1] in [37, Eq.(19)] and used also in [27, Eq.(28)], [31, Eq.(2.11)], and is given by:

$$\begin{aligned}\mathcal{Z}(s) &= pc_dR_2^d\left[1-\exp\left(-sb_j|\tilde{h}|^2R_2^{-\alpha}\right)\right]-pc_dR_1^d\left[1-\exp\left(-sb_j|\tilde{h}|^2R_1^{-\alpha}\right)\right] \\ &\quad + pc_d\left(sb_j|\tilde{h}|^2\right)^{d/\alpha}\left[\Gamma\left(1-\frac{d}{\alpha},sb_j|\tilde{h}|^2R_2^{-\alpha}\right)-\Gamma\left(1-\frac{d}{\alpha},sb_j|\tilde{h}|^2R_1^{-\alpha}\right)\right]\end{aligned} \tag{1.10}$$

where $\Gamma(a,x)=\int_x^\infty t^{a-1}e^{-t}\mathrm{d}t$ is the upper incomplete Gamma function. Substituting (1.10) in (1.9), the MGF of the aggregate interference power is finally obtained:

$$\begin{aligned}\mathcal{M}_{\mathcal{I}_\Phi}(s) = \prod_{j=1}^{M}\exp\Big\{&p\lambda c_dR_1^d\mathbb{E}_{|\tilde{h}|^2}\left\{1-e^{-sb_j|\tilde{h}|^2R_1^{-\alpha}}\right\}-p\lambda c_dR_2^d\mathbb{E}_{|\tilde{h}|^2}\left\{1-e^{-sb_j|\tilde{h}|^2R_2^{-\alpha}}\right\} \\ &+ p\lambda c_d(sb_j)^{d/\alpha}\mathbb{E}_{|\tilde{h}|^2}\left\{|\tilde{h}|^{2d/\alpha}\Gamma\left(1-\frac{d}{\alpha},sb_j|\tilde{h}|^2R_1^{-\alpha}\right)\right\} \\ &- p\lambda c_d(sb_j)^{d/\alpha}\mathbb{E}_{|\tilde{h}|^2}\left\{|\tilde{h}|^{2d/\alpha}\Gamma\left(1-\frac{d}{\alpha},sb_j|\tilde{h}|^2R_2^{-\alpha}\right)\right\}\Big\}^{\frac{1}{M}}\end{aligned} \tag{1.11}$$

It is worthwhile noting how the modulation coefficients $\{b_j\}_{j=1}^M$ are taken into account in the MGF through the geometric mean of the MGF evaluated for each of

[1] Apart from the coefficients b_j, which however can be easily included in the final result.

the modulation symbols, *i.e.*

$$\mathcal{M}_{\mathcal{I}_\Phi}(s) = \left[\prod_{j=1}^{M} \mathcal{M}_{\mathcal{I}_\Phi,j}(sb_j)\right]^{\frac{1}{M}} \tag{1.12}$$

where $\mathcal{M}_{\mathcal{I}_\Phi,j}$ denotes the j-th term of the summation in (1.11). In the following, a constant envelope modulation (*e.g.* MPSK) with $b_i = 1\ \forall i$ will be considered, unless otherwise specified. In this case, the MGF in (1.11) can be simplified to:

$$\begin{aligned}\mathcal{M}_{\mathcal{I}_\Phi}(s) =& \exp\left\{pc_d\lambda R_1^d \mathbb{E}_{|\tilde{h}|^2}\left\{1 - e^{-s|\tilde{h}|^2 R_1^{-\alpha}}\right\} - pc_d\lambda R_2^d \mathbb{E}_{|\tilde{h}|^2}\left\{1 - e^{-s|\tilde{h}|^2 R_2^{-\alpha}}\right\}\right. \\ &+ pc_d\lambda s^{d/\alpha}\mathbb{E}_{|\tilde{h}|^2}\left\{|\tilde{h}|^{\frac{2d}{\alpha}}\Gamma\left(1 - \frac{d}{\alpha}, s|\tilde{h}|^2 R_1^{-\alpha}\right)\right\} \\ &\left.- pc_d\lambda s^{d/\alpha}\mathbb{E}_{|\tilde{h}|^2}\left\{|\tilde{h}|^{\frac{2d}{\alpha}}\Gamma\left(1 - \frac{d}{\alpha}, s|\tilde{h}|^2 R_2^{-\alpha}\right)\right\}\right\}\end{aligned} \tag{1.13}$$

1.3.1 Nakagami-m Fading Channels

In this section, a closed-form expression for the MGF in (1.13) for Nakagami-m fading channels is provided. In [27, 31] the authors provide only upper-bound approximations for Rayleigh fading channels or consider some simplified network shapes (*e.g.* $R_1 = 0$ and $R_2 = \infty$), while in [24, Eq.(3.21)] a closed-form is obtained only for $\alpha = 4$ and Rayleigh fading. In this thesis, an exact result on the annular region defined in the previous section when the interfering links experience Nakagami-m fading channels is obtained, which allows to evaluate the exact solution for Rayleigh fading (Section 1.3.2) and non fading (Section 1.3.3) scenarios as well.
When the interfering links experience Nakagami-m fading with the same parameter m_0, the pdf of the normalized fading coefficients $|\tilde{h}_i|^2$ is given by [36, Eq.(2.21)]:

$$f_{|\tilde{h}_i|^2}(\xi) = \frac{m_0^{m_0}\xi^{(m_0-1)}}{\Gamma(m_0)}e^{-m_0\xi} \tag{1.14}$$

With reference to (1.13), the following two expectations need to be computed:

$$\begin{aligned}\mathcal{T}_1 &= \mathbb{E}_{|\tilde{h}_i|^2}\left\{1 - \exp\left(-s|\tilde{h}_i|^2 R^{-\alpha}\right)\right\} \\ \mathcal{T}_2 &= \mathbb{E}_{|\tilde{h}_i|^2}\left\{|\tilde{h}_i|^{\frac{2d}{\alpha}}\Gamma\left(1 - \frac{d}{\alpha}, s|\tilde{h}_i|^2 R^{-\alpha}\right)\right\}\end{aligned}$$

$\mathcal{T}_1$ is obtained from the MGF of a Nakagami-m distribution [36, Eq.(2.22)]:

$$\mathcal{T}_1 = 1 - \mathcal{M}_{|\tilde{h}_i|^2}(sR^{-\alpha}) = 1 - \left(1 + \frac{sR^{-\alpha}}{m_0}\right)^{-m_0} \tag{1.15}$$

The evaluation of $\mathcal{T}_2$ is trickier, and requires the series expansion of the upper incomplete Gamma function. Combining [38, Eq.(6.5.3)] and [38, Eq.(6.5.4)], it can be written as:

$$\Gamma(a,x) = \Gamma(a) - \gamma(a,x) = \Gamma(a) - \Gamma(a)x^a\gamma^*(a,x)$$

where $\gamma(a,x) = \int_0^x t^{a-1}e^{-t}\mathrm{d}t$ is the lower incomplete Gamma function, and $\gamma^*(a,x)$ is a single valued analytic function possessing no finite singularities, with series development given by [38, Eq.(6.5.29)]:

$$\gamma^*(a,x) = e^{-x}\sum_{k=0}^{\infty}\frac{x^k}{\Gamma(a+k+1)}$$

Thus, the upper incomplete Gamma function has the following series expansion:

$$\Gamma(a,x) = \Gamma(a) - \Gamma(a)x^a e^{-x}\sum_{k=0}^{\infty}\frac{x^k}{\Gamma(a+k+1)} \tag{1.16}$$

and $\mathcal{T}_2$ can be written as:

$$\begin{aligned}
\mathcal{T}_2 &= \Gamma\left(1-\frac{d}{\alpha}\right)\mathbb{E}_{|\tilde{h}_i|^2}\left\{|\tilde{h}_i|^{\frac{2d}{\alpha}}\right\} \\
&\quad - \Gamma\left(1-\frac{d}{\alpha}\right)\mathbb{E}_{|\tilde{h}_i|^2}\left\{|\tilde{h}_i|^{\frac{2d}{\alpha}}\left(s|\tilde{h}_i|^2\right)^{(1-\frac{d}{\alpha})}e^{-s|\tilde{h}_i|^2R^{-\alpha}}\sum_{k=0}^{\infty}\frac{\left(s|\tilde{h}_i|^2R^{-\alpha}\right)^k}{\Gamma\left(k+2-\frac{d}{\alpha}\right)}\right\} \\
&= \Gamma\left(1-\frac{d}{\alpha}\right)\mathbb{E}_{|\tilde{h}_i|^2}\left\{|\tilde{h}_i|^{\frac{2d}{\alpha}}\right\} \\
&\quad - \Gamma\left(1-\frac{d}{\alpha}\right)\left(sR^{-\alpha}\right)^{(1-\frac{d}{\alpha})}\sum_{k=0}^{\infty}\frac{\left(sR^{-\alpha}\right)^k}{\Gamma\left(k+2-\frac{d}{\alpha}\right)}\mathbb{E}_{|\tilde{h}_i|^2}\left\{|\tilde{h}_i|^{(2k+2)}e^{-s|\tilde{h}_i|^2R^{-\alpha}}\right\}
\end{aligned}$$

where:

$$\begin{aligned}
\mathbb{E}_{|\tilde{h}_i|^2}\left\{|\tilde{h}_i|^{\frac{2d}{\alpha}}\right\} &\overset{(a)}{=} \frac{\Gamma\left(m_0+\frac{d}{\alpha}\right)}{\Gamma(m_0)m_0^{d/\alpha}} \\
\mathbb{E}_{|\tilde{h}_i|^2}\left\{|\tilde{h}_i|^{(2k+2)}e^{-s|\tilde{h}_i|^2R^{-\alpha}}\right\} &\overset{(b)}{=} \frac{m_0^{m_0}\Gamma\left(k+1+m_0\right)}{\Gamma(m_0)(m_0+sR^{-\alpha})^{(k+1+m_0)}}
\end{aligned} \tag{1.17}$$

with (a) following from [36, Eq.(2.23)] and (b) being a known integral. Solving the expectations in $\mathcal{T}_2$ with the above formulas yields to:

$$\begin{aligned}\mathcal{T}_2 &= \Gamma\left(1-\frac{d}{\alpha}\right)\frac{\Gamma\left(m_0+\frac{d}{\alpha}\right)}{\Gamma(m_0)m_0^{d/\alpha}} - \Gamma\left(1-\frac{d}{\alpha}\right)\left(sR^{-\alpha}\right)^{(1-\frac{d}{\alpha})} \\ &\quad\times\sum_{k=0}^{\infty}\left[\frac{\left(sR^{-\alpha}\right)^k}{\Gamma\left(k+2-\frac{d}{\alpha}\right)}\frac{m_0^{m_0}\Gamma\left(k+1+m_0\right)}{\Gamma(m_0)(m_0+sR^{-\alpha})^{(k+1+m_0)}}\right] \\ &= \Gamma\left(1-\frac{d}{\alpha}\right)\frac{\Gamma\left(m_0+\frac{d}{\alpha}\right)}{\Gamma(m_0)m_0^{d/\alpha}} - \left(sR^{-\alpha}\right)^{(1-\frac{d}{\alpha})} \\ &\quad\times\frac{m_0^{m_0}\Gamma(1+m_0)}{\Gamma(m_0)\left(1-\frac{d}{\alpha}\right)}\frac{{}_2F_1\left(m_0+1;1;2-\frac{d}{\alpha};\frac{s}{s+m_0R^{\alpha}}\right)}{\left(m_0+sR^{-\alpha}\right)^{(m_0+1)}} \qquad (1.18)\end{aligned}$$

where the well known relation $\Gamma(z+1) = z\Gamma(z)$ was used, ${}_2F_1(a;b;c;z)$ is the Gauss' hypergeometric function and the second equality follows from its infinite series representation given by [38, Eq.(15.1.1)]:

$${}_2F_1(a;b;c;z) = \frac{\Gamma(c)}{\Gamma(a)\Gamma(b)}\sum_{n=0}^{\infty}\frac{\Gamma(a+n)\Gamma(b+n)}{\Gamma(c+n)}\frac{z^n}{n!} \qquad (1.19)$$

Substituting the expectations obtained in (1.15) and (1.18) in equation (1.13):

$$\begin{aligned}\mathcal{M}_{\mathcal{I}_\Phi}(s) = \exp\Bigg\{ & pc_d\lambda R_1^d - pc_d\lambda R_2^d + \frac{pc_d\lambda R_2^d}{\left(1+\frac{sR_2^{-\alpha}}{m_0}\right)^{m_0}} - \frac{pc_d\lambda R_1^d}{\left(1+\frac{sR_1^{-\alpha}}{m_0}\right)^{m_0}} \\ & + pc_d\lambda s^{d/\alpha}\Gamma\left(1-\frac{d}{\alpha}\right)\frac{\Gamma\left(m_0+\frac{d}{\alpha}\right)}{\Gamma(m_0)m_0^{d/\alpha}} - pc_d\lambda s^{d/\alpha}\Gamma\left(1-\frac{d}{\alpha}\right)\frac{\Gamma\left(m_0+\frac{d}{\alpha}\right)}{\Gamma(m_0)m_0^{d/\alpha}} \\ & - pc_d\lambda s^{d/\alpha}\left(sR_1^{-\alpha}\right)^{(1-\frac{d}{\alpha})}\frac{m_0^{m_0}\Gamma(1+m_0)}{\Gamma(m_0)\left(1-\frac{d}{\alpha}\right)}\frac{{}_2F_1\left(m_0+1;1;2-\frac{d}{\alpha};\frac{s}{s+m_0R_1^{\alpha}}\right)}{\left(m_0+sR_1^{-\alpha}\right)^{(m_0+1)}} \\ & + pc_d\lambda s^{d/\alpha}\left(sR_2^{-\alpha}\right)^{(1-\frac{d}{\alpha})}\frac{m_0^{m_0}\Gamma(1+m_0)}{\Gamma(m_0)\left(1-\frac{d}{\alpha}\right)}\frac{{}_2F_1\left(m_0+1;1;2-\frac{d}{\alpha};\frac{s}{s+m_0R_2^{\alpha}}\right)}{\left(m_0+sR_2^{-\alpha}\right)^{(m_0+1)}}\Bigg\}\end{aligned}$$

which after some simplifications provides the following closed-form expression of the MGF of the aggregate interference power over Nakagami-m fading channels:

$$\begin{aligned}\mathcal{M}_{\mathcal{I}_\Phi}(s) = \exp&\left[pc_d\lambda R_1^d - pc_d\lambda R_2^d + \frac{pc_d\lambda R_2^d}{\left(1+\frac{sR_2^{-\alpha}}{m_0}\right)^{m_0}} - \frac{pc_d\lambda R_1^d}{\left(1+\frac{sR_1^{-\alpha}}{m_0}\right)^{m_0}}\right] \\ &\times \exp\left[-pc_d\lambda s R_1^{(d-\alpha)} \frac{m_0^{m_0}\Gamma(1+m_0)}{\Gamma(m_0)\left(1-\frac{d}{\alpha}\right)} \frac{{}_2F_1\left(m_0+1;1;2-\frac{d}{\alpha};\frac{s}{s+m_0R_1^\alpha}\right)}{\left(m_0+sR_1^{-\alpha}\right)^{(m_0+1)}}\right] \\ &\times \exp\left[pc_d\lambda s R_2^{(d-\alpha)} \frac{m_0^{m_0}\Gamma(1+m_0)}{\Gamma(m_0)\left(1-\frac{d}{\alpha}\right)} \frac{{}_2F_1\left(m_0+1;1;2-\frac{d}{\alpha};\frac{s}{s+m_0R_2^\alpha}\right)}{\left(m_0+sR_2^{-\alpha}\right)^{(m_0+1)}}\right]\end{aligned} \tag{1.20}$$

1.3.2 Rayleigh Fading Channels

The MGF of the aggregate interference power over Rayleigh fading channels can be easily obtained from equation (1.20) setting $m_0 = 1$:

$$\begin{aligned}\mathcal{M}_{\mathcal{I}_\Phi}(s) = \exp&\left[pc_d\lambda R_1^d \frac{sR_1^{-\alpha}}{1+sR_1^{-\alpha}} - pc_d\lambda R_2^d \frac{sR_2^{-\alpha}}{1+sR_2^{-\alpha}}\right] \\ &\times \exp\left[-pc_d\lambda s R_1^{(d-\alpha)} \frac{{}_2F_1\left(2;1;2-\frac{d}{\alpha};\frac{s}{s+R_1^\alpha}\right)}{\left(1+sR_1^{-\alpha}\right)^2\left(1-\frac{d}{\alpha}\right)}\right] \\ &\times \exp\left[pc_d\lambda s R_2^{(d-\alpha)} \frac{{}_2F_1\left(2;1;2-\frac{d}{\alpha};\frac{s}{s+R_2^\alpha}\right)}{\left(1+sR_2^{-\alpha}\right)^2\left(1-\frac{d}{\alpha}\right)}\right]\end{aligned} \tag{1.21}$$

Otherwise, the same procedure used for Nakagami-m fading channels can be applied by using the pdf of a Rayleigh distribution with unit mean [36, Eq.(2.7)]:

$$f_{|\tilde{h}_i|^2}(\xi) = e^{-\xi} \tag{1.22}$$

1.3.3 Non Fading Channels

The MGF of the aggregate interference power over non-fading channels is straightforward to be obtained, as it just requires setting $|\tilde{h}_i| = 1$ in (1.21) or $m_0 = 1$ and $|\tilde{h}_i| = 1$ in (1.13), consequently removing the expectations on $|\tilde{h}_i|^2$:

$$\begin{aligned}\mathcal{M}_{\mathcal{I}_\Phi}(s) = \exp&\left\{pc_d\lambda R_1^d\left[1-e^{-sR_1^{-\alpha}}\right] - pc_d\lambda R_2^d\left[1-e^{-sR_2^{-\alpha}}\right]\right. \\ &\left. + pc_d\lambda s^{d/\alpha}\Gamma\left(1-\frac{d}{\alpha}, sR_1^{-\alpha}\right) - pc_d\lambda s^{d/\alpha}\Gamma\left(1-\frac{d}{\alpha}, sR_2^{-\alpha}\right)\right\}\end{aligned} \tag{1.23}$$

1.3.4 Special Cases of the Network Deployment Area

In the present section, the MGF over Nakagami-m, Rayleigh and non fading channels starting from equations (1.13) and (1.23) is provided for particular values of R_1 and R_2 applying the expectations previously evaluated in (1.15), (1.17), and (1.18).

1.3.4.1 Infinite Area ($0 = R_1 < R_2 = \infty$)

Consider a cognitive network where nodes are deployed according to a PPP over an infinite area. The MGF can be evaluated by following the same procedure as for the annular region setting $R_1 = 0$ and $R_2 = \infty$ in equation (1.13):

$$\mathcal{M}_{\mathcal{I}_\Phi}(s) = \exp\left\{-pc_d\lambda s^{d/\alpha}\Gamma\left(1-\frac{d}{\alpha}\right)\mathbb{E}_{|\tilde{h}_i|^2}\left\{|\tilde{h}_i|^{\frac{2d}{\alpha}}\right\}\right\} \tag{1.24}$$

Nakagami-m fading:

$$\mathcal{M}_{\mathcal{I}_\Phi}(s) = \exp\left\{-pc_d\lambda s^{d/\alpha}\frac{\Gamma\left(1-\frac{d}{\alpha}\right)\Gamma\left(m_0+\frac{d}{\alpha}\right)}{\Gamma(m_0){m_0}^{d/\alpha}}\right\} \tag{1.25}$$

Rayleigh fading:

$$\mathcal{M}_{\mathcal{I}_\Phi}(s) = \exp\left\{-pc_d\lambda s^{d/\alpha}\frac{\pi\frac{d}{\alpha}}{\sin\left(\pi\frac{d}{\alpha}\right)}\right\} \tag{1.26}$$

where the well known equality $\Gamma\left(1-\frac{d}{\alpha}\right)\Gamma\left(1+\frac{d}{\alpha}\right) = \frac{\pi\frac{d}{\alpha}}{\sin\left(\pi\frac{d}{\alpha}\right)}$ was used. Note that (1.26) is the same as [24, Eq.(3.21)], which substantiates the validity of our approach.

No fading:

$$\mathcal{M}_{\mathcal{I}_\Phi}(s) = \exp\left\{-pc_d\lambda s^{d/\alpha}\Gamma\left(1-\frac{d}{\alpha}\right)\right\} \tag{1.27}$$

This formula evaluated for $\alpha = 4$ yields to [24, Eq.(3.18)]. It is worthwhile noting that by letting $m_0 \to \infty$ in equation (1.25), the above expression is obtained, as expected: a Nakagami-m fading channel tends to an Additive White Gaussian Noise (AWGN) channel when its parameter tends to infinity.

1.3.4.2 Finite Area ($0 = R_1 < R_2 < \infty$)

In this scenario, a closed ball centered in the origin, $b(o, R_2)$, is considered, and thus $R_1 = 0$ and R_2 is finite. From (1.13), the MGF is given by:

$$\begin{aligned}\mathcal{M}_{\mathcal{I}_\Phi}(s) = &\exp\left\{-pc_d\lambda R_2^d\mathbb{E}_{|\tilde{h}_i|^2}\left\{1-e^{-s|\tilde{h}_i|^2R_2^{-\alpha}}\right\}\right.\\ &\left.-\,pc_d\lambda s^{d/\alpha}\mathbb{E}_{|\tilde{h}_i|^2}\left\{|\tilde{h}_i|^{\frac{2d}{\alpha}}\Gamma\left(1-\frac{d}{\alpha}, s|\tilde{h}_i|^2R_2^{-\alpha}\right)\right\}\right\}\end{aligned} \tag{1.28}$$

Nakagami-m fading:

$$\mathcal{M}_{\mathcal{I}_\Phi}(s) = \exp\left\{ -pc_d\lambda R_2^d + \frac{c_d\lambda R_2^d}{\left(1+\frac{sR_2^{-\alpha}}{m_0}\right)^{m_0}} - pc_d\lambda s^{d/\alpha}\frac{\Gamma\left(1-\frac{d}{\alpha}\right)\Gamma\left(m_0+\frac{d}{\alpha}\right)}{\Gamma(m_0){m_0}^{d/\alpha}} + pc_d\lambda s{R_2}^{(d-\alpha)}\frac{{m_0}^{(m_0+1)}}{\left(1-\frac{d}{\alpha}\right)}\frac{{}_2F_1\left(m_0+1;1;2-\frac{d}{\alpha};\frac{s}{s+m_0R_2^\alpha}\right)}{\left(m_0+sR_2^{-\alpha}\right)^{(m_0+1)}} \right\} \tag{1.29}$$

where the well know relation $\Gamma(1+z) = z\Gamma(z)$ was applied.

Rayleigh fading:

$$\mathcal{M}_{\mathcal{I}_\Phi}(s) = \exp\left\{ -pc_d\lambda R_2^d\frac{sR_2^{-\alpha}}{1+sR_2^{-\alpha}} - pc_d\lambda s^{d/\alpha}\frac{\pi\frac{d}{\alpha}}{\sin\left(\pi\frac{d}{\alpha}\right)} + pc_d\lambda s{R_2}^{(2-\alpha)}\frac{{}_2F_1\left(2;1;2-\frac{d}{\alpha};\frac{s}{s+R_2^\alpha}\right)}{\left(1-\frac{d}{\alpha}\right)\left(1+sR_2^{-\alpha}\right)^2} \right\} \tag{1.30}$$

No fading:

$$\mathcal{M}_{\mathcal{I}_\Phi}(s) = \exp\left\{ -pc_d\lambda R_2^d\left[1-e^{-sR_2^{-\alpha}}\right] - pc_d\lambda s^{d/\alpha}\Gamma\left(1-\frac{d}{\alpha}\right)\right\} \tag{1.31}$$

1.3.4.3 Exclusion Region ($0 < R_1 < R_2 < +\infty$)

In this last scenario, a cognitive network deployed in an infinite space around the origin, with an exclusion ball around it with radius $R_1 \neq 0$, is considered. For the purpose of this thesis, this is the most important scenario, as the coverage probability and the average achievable rate will be evaluated in this case (see Chapter 2 and Chapter 3, respectively). In this scenario, the MGF is given by:

$$\mathcal{M}_{\mathcal{I}_\Phi}(s) = \exp\left\{ pc_d\lambda R_1^d\mathbb{E}_{|\tilde{h}_i|^2}\left\{1-e^{-s|\tilde{h}_i|^2R_1^{-\alpha}}\right\} - pc_d\lambda s^{d/\alpha}\Gamma\left(1-\frac{d}{\alpha}\right)\mathbb{E}_{|\tilde{h}_i|^2}\left\{|\tilde{h}_i|^{\frac{2d}{\alpha}}\right\} + pc_d\lambda s^{d/\alpha}\mathbb{E}_{|\tilde{h}_i|^2}\left\{|\tilde{h}_i|^{\frac{2d}{\alpha}}\Gamma\left(1-\frac{d}{\alpha},s|\tilde{h}_i|^2R_1^{-\alpha}\right)\right\}\right\} \tag{1.32}$$

Nakagami-m fading:

$$\mathcal{M}_{\mathcal{I}_\Phi}(s) = \exp\left\{ pc_d\lambda R_1^d - \frac{pc_d\lambda R_1^d}{\left(1+\frac{sR_1^{-\alpha}}{m_0}\right)^{m_0}} - pc_d\lambda s{R_1}^{(d-\alpha)}\frac{{m_0}^{(m_0+1)}}{\left(1-\frac{d}{\alpha}\right)}\frac{{}_2F_1\left(m_0+1;1;2-\frac{d}{\alpha};\frac{s}{s+m_0R_1^\alpha}\right)}{\left(m_0+sR_1^{-\alpha}\right)^{(m_0+1)}} \right\} \tag{1.33}$$

Rayleigh fading:

$$\mathcal{M}_{\mathcal{I}_\Phi}(s) = \exp\left\{ pc_d\lambda R_1^d \frac{sR_1^{-\alpha}}{1+sR_1^{-\alpha}} - pc_d\lambda s{R_1}^{(d-\alpha)} \frac{{}_2F_1\left(2;1;2-\frac{d}{\alpha};\frac{s}{s+R_1^\alpha}\right)}{\left(1-\frac{d}{\alpha}\right)\left(1+sR_1^{-\alpha}\right)^2} \right\} \tag{1.34}$$

No fading:

$$\begin{aligned}\mathcal{M}_{\mathcal{I}_\Phi}(s) = &\exp\left\{ pc_d\lambda R_1^d\left[1-e^{-sR_1^d}\right] - pc_d\lambda s^{d/\alpha}\Gamma\left(1-\frac{d}{\alpha}\right)\right. \\ &\left. + pc_d\lambda s^{d/\alpha}\Gamma\left(1-\frac{d}{\alpha}, sR_1^{-\alpha}\right)\right\}\end{aligned} \tag{1.35}$$

1.3.5 Simulation Complexity

From a practical point of view, the simulation of a Poisson cognitive network deployed over finite areas is straightforward. As stated in the previous sections, the points have to be uniformly distributed over this area, and their number is a Poisson random variable with density related to the network radius. However, when considering infinite areas (as those introduced in Sections 1.3.4.1 and 1.3.4.3), a simulation with infinite radius is not feasible, and it is thus necessary to truncate the simulation area introducing an error. In [32] the authors analyzed this problem, and provided two different solutions: (i) choosing the truncation radius such that the impact of the aggregate interference generated by the nodes located outside this radius is negligible; or (ii) add a correction term in order to account for the excluded nodes. In particular, in [32] the exact expression of the mean aggregate interference generated by the nodes located outside the simulated area is computed thanks to Campbell's Theorem (Theorem A.4 in Section A.3).

Consider the infinite area as in Section 1.3.4.1, and assume also that: (i) all nodes transmit symbols belonging to a constant envelope modulation (*i.e.* $b_j = 1, \forall j$); (ii) all nodes always transmit (*i.e.* $p = 1$); and (iii) there is no fading (*i.e.* $\left|\tilde{h}_i\right|^2 = 1$). In this scenario, the mean interference generated outside a closed d-dimensional ball $b(o, R_2)$ (*i.e.* outside the radius of the simulated area) can be evaluated applying

Campbell's Theorem as follows:

$$\begin{aligned}\mathbb{E}_{\mathbb{P}}\left\{\mathcal{I}_{\Phi}^{out}\right\} &= \mathbb{E}_{\mathbb{P}}\left\{\sum_{\mathbf{x}_i\in\mathbb{R}^d\setminus b(o,R_2)}\ell\left(\|\mathbf{x}_i\|\right)\right\} = \lambda\int\limits_{\mathbb{R}^d\setminus b(o,R_2)}\ell\left(\|\mathbf{x}\|\right)\mathrm{d}\mathbf{x}\\ &= c_d\lambda d\int\limits_{R_2}^{\infty} r^{d-\alpha-1}\mathrm{d}r = \left[\frac{c_d\lambda d}{\alpha-d}r^{d-\alpha}\right]_{R_2}^{\infty}\\ &\overset{(a)}{=} \frac{c_d\lambda d}{\alpha-d}{R_2}^{d-\alpha}\end{aligned} \tag{1.36}$$

where (a) follows from the assumption that $\alpha > d$ (see Section 1.1). The above mean value can be used either to find the radius such that the interference falling out of the simulation area is negligible (approach (i)), or as a correcting factor by simply adding it to the aggregate interference simulated with finite radius, *i.e.* $\mathcal{I}_{\Phi} = \mathcal{I}_{\Phi}^{sim} + \mathbb{E}_{\mathbb{P}}\left\{\mathcal{I}_{\Phi}^{out}\right\}$ (approach (ii)). It is worthwhile noting that the mean interference in (1.36) can not be used to evaluate the mean interference in the whole infinite area setting $R_2 = 0$. In this case, $r^{(d-\alpha)} \to \infty$ for $r \to 0$, because $\alpha > d$. As a matter of facts, moving a node location towards the origin makes its interference contribution explode due to the considered path-loss model. However, a simple solution to this problem was proposed in [24]. Consider a limited exponential-decaying path-loss model, *i.e.* $\ell(r) = \min\left(1, r^{-\alpha}\right)$, and $R_2 > 1$. In this case the mean interference in the simulated area is given by:

$$\mathbb{E}_{\mathbb{P}}\left\{\mathcal{I}_{\Phi}^{in}\right\} = c_d\lambda d\int\limits_{0}^{R_2} r^{d-1}\min\left(1, r^{-\alpha}\right)\mathrm{d}r = c_d\lambda + \frac{c_d\lambda d}{\alpha-d}\left(1-R_2^{d-\alpha}\right) \tag{1.37}$$

while that in the whole space is[2]:

$$\mathbb{E}_{\mathbb{P}}\left\{\mathcal{I}_{\Phi}\right\} = c_d\lambda d\int\limits_{0}^{\infty} r^{d-1}\min\left(1, r^{-\alpha}\right)\mathrm{d}r = c_d\lambda + \frac{c_d\lambda d}{\alpha-d} \tag{1.38}$$

By comparing (1.38) with (1.37), and assuming that the neglected interference shall be less than a given percentage ε, the simulated area radius R_2 must satisfy the following condition:

$$1 - R_2^{(d-\alpha)} > 1-\varepsilon \Longrightarrow R_2 > \varepsilon^{-\left(\frac{1}{\alpha-d}\right)} \tag{1.39}$$

It is worthwhile noting that the minimum value of radius such that the accuracy requirement is satisfied increases for decreasing values of the propagation exponent

[2]Note that it is equal to the sum of (1.36) and (1.37), as in the former one the minimum value $\ell(r) = 1$ does not appear assuming $R_2 > 1$.

α. For example, with $d = 2$, $\alpha = 4$ and $\varepsilon = 10^{-3}$ we have that $R_2 > 32$, while in the same conditions for $\alpha = 2.5$ the radius is in the order of 10^6.

1.3.6 Numerical Results

In this section, the analytical framework obtained for the Moment Generating Function is compared to Monte Carlo simulations for a 2D Poisson cognitive network, which is the case of major interest. In each simulation, $N \sim Poisson(\pi\lambda R_2^2)$ nodes were uniformly distributed in the considered area, and the aggregate interference power was measured at the origin of the Euclidean plane. The MGF was then obtained by averaging over many iterations, in which the fading coefficients (if considered) took different values, according to Nakagami-m and Rayleigh distributions. All the results shown in this section were obtained with $\alpha = 4, 5$, and the truncation radius for the simulation setup was chosen according to equation (1.39). However, note that all the closed-form expression previously obtained are valid for any $\alpha > 2$ and any dimension order d.

First of all, consider equation (1.11) which shows the dependency of the MGF on the modulation type/order. It was shown that it can be evaluated as a geometric mean (equation (1.12)), where each term is given by the MGF itself evaluated at (sb_j). In case of an infinite area, it can be written as:

$$\mathcal{M}_{\mathcal{I}_\Phi} = \left[\prod_{j=1}^{M} \exp\left\{-pc_d\lambda s^{d/\alpha}\Gamma\left(1-\frac{d}{\alpha}\right)\mathbb{E}_{|\tilde{h}_i|^2}\left\{|\tilde{h}_i|^{\frac{2d}{\alpha}}\right\}\right\}\right]^{\frac{1}{M}}$$

By writing the product of an exponential as the exponential of the sum, this expression can be simplified to the following form:

$$\mathcal{M}_{\mathcal{I}_\Phi} = \exp\left\{-K_M pc_d\lambda s^{d/\alpha}\Gamma\left(1-\frac{d}{\alpha}\right)\mathbb{E}_{|\tilde{h}_i|^2}\left\{|\tilde{h}_i|^{\frac{2d}{\alpha}}\right\}\right\} \tag{1.40}$$

where K_M is a modulation factor which has the same effect on the MGF as those of the transmission probability p and the density λ, and is given by:

$$K_M = \frac{1}{M}\sum_{j=1}^{M} b_j^{d/\alpha} \tag{1.41}$$

In Table 1.1 some values of this factor are provided for $d = 2, 3$ and $\alpha = 3, 4, 5$. The values of K_M are all quite close to unity, and this is reflected in a slight difference between the MGFs for different modulation type and order. In particular, the MGF takes lower values for lower K_M, and this will be confirmed by the results obtained

	d = 2		**d = 3**	
Modulation	$\boldsymbol{\alpha}$	$\mathbf{K_M}$	$\boldsymbol{\alpha}$	$\mathbf{K_M}$
MPSK	3	1.0000	3	1.0000
	4	1.0000	4	1.0000
	5	1.0000	5	1.0000
16-APSK	3	0.9883	3	1.0000
	4	0.9870	4	0.9901
	5	0.9877	5	0.9875
16-QAM	3	0.9432	3	1.0000
	4	0.9472	4	0.9633
	5	0.9476	5	0.9509
64-QAM	3	0.9490	3	1.0000
	4	0.9392	4	0.9581
	5	0.9393	5	0.9437

Table 1.1: Modulation factor K_M for $d = 2, 3$ and $\alpha = 3, 4, 5$.

for varying λ or p. For this reason, constant envelope modulations will be considered in the following unless otherwise specified. Please note that this simplification is valid only for infinite areas. For all the other scenarios, the geometric mean has to be evaluated as in (1.12). Nonetheless, in the other scenarios the differences for varying modulation type and/or order are negligible as well.
The behaviour of the Moment Generating Function can thus be analyzed for several values of p and λ, assuming a modulation with constant envelope is being used. Moreover, the product $p\lambda$ can be directly taken into account, as the two factors have the same effect on the MGF: in all of the closed-form expression of the MGF provided in Section 1.3, considering $\lambda = 0.1$ and $p = 1$ is the same as considering $\lambda = 1$ and $p = 0.1$. This is due to the thinning property of a Poisson Point Process, as shown in Section A.2 (see Proposition A.4). Furthermore, an annular region will be considered, as it is the most general case: all the other scenarios are originated by this one for particular values of R_1 and R_2. From Figures 1.1-1.3 the following general trends can be observed:

- the MGF takes lower values for decresing α, *i.e.* better channel conditions. This can be easily explained considering its definition in equation (1.4). Improving the channel conditions increases the aggregate interference level, and thus it increases the negative exponent of an exponential function as well, consequently providing lower values of the MGF;

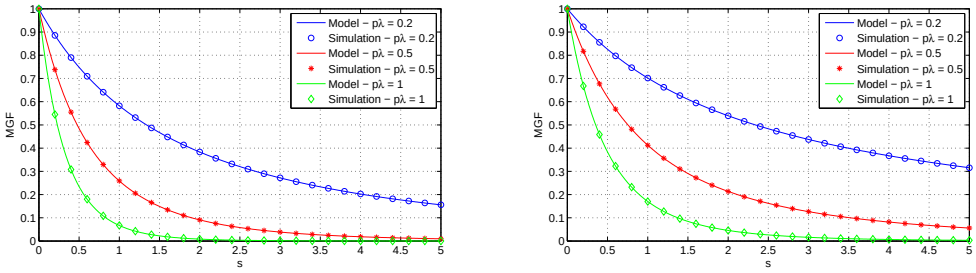

(a) $\alpha = 4$ (b) $\alpha = 5$

Figure 1.1: Moment Generating Function in an annular region over non fading channels. Analytical model given by (1.23). Setup: i) $\alpha = 4, 5$; ii) $p\lambda = 0.2, 0.5, 1$; and iii) $R_1 = 1$, $R_2 = 32$.

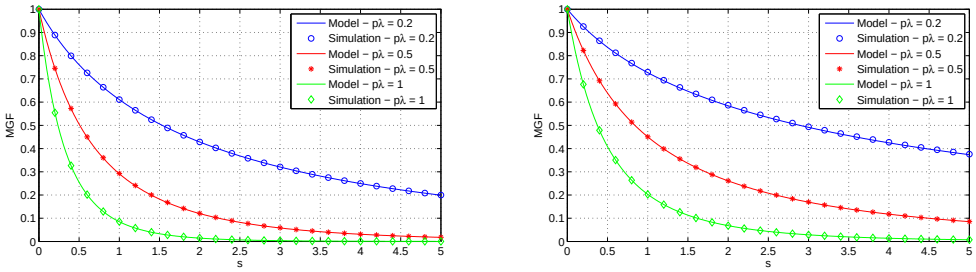

(a) $\alpha = 4$ (b) $\alpha = 5$

Figure 1.2: Moment Generating Function in an annular region over Rayleigh fading channels. Analytical model given by (1.21). Setup: i) $\alpha = 4, 5$; ii) $p\lambda = 0.2, 0.5, 1$; and iii) $R_1 = 1$, $R_2 = 32$.

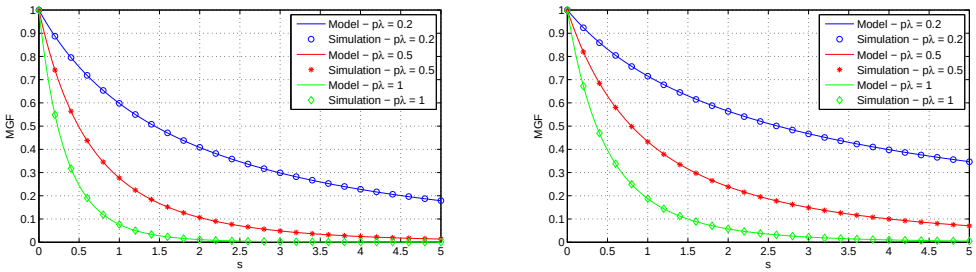

(a) $\alpha = 4$ (b) $\alpha = 5$

Figure 1.3: Moment Generating Function in an annular region over Nakagami-m fading channels. Analytical model given by (1.20). Setup: i) $m_0 = 2$; ii) $\alpha = 4, 5$; iii) $p\lambda = 0.2, 0.5, 1$; and iv) $R_1 = 1$, $R_2 = 32$.

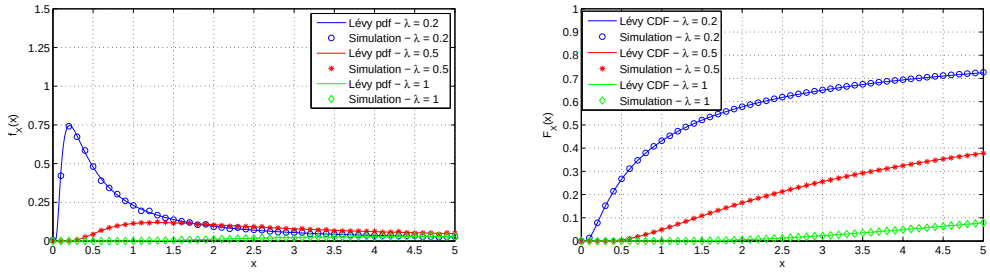

(a) pdf (b) CDF

Figure 1.4: pdf and CDF of $\mathcal{I}_\Phi$ for $\alpha = 4$ over an infinite area with no fading. Analytical model given by (1.42). Setup: i) $\lambda = 0.2, 0.5, 1$; and ii) $R_2 = 32$.

- the MGF presents lower values for increasing values of p and/or λ, which corresponds to higher interference environments, as there are more interfering nodes on the considered area, or the probability that they transmit is higher. This behaviour is motivated by the same reasons as in the previous point: worse/better interfering links conditions make the exponential function in the MGF definition be slower/faster in going to zero;

- the MGF shape is almost independent from the considered channel model. This behaviour can be explained noting that the MGF provides a measure of the mean interference, which is given by the path-loss. The fading coefficients (if present) introduce some fluctuations around this mean value, which are negligible in the MGF, but not in several key performance metrics (*e.g.* coverage probability, rate, etc.) which are obtained starting from the MGF.

Finally, it can be observed that the mathematical framework provided in this chapter presents an excellent agreement with Monte Carlo simulations.

1.4 PDF and CDF of the Aggregate Interference Power

In the previous sections, the Moment Generating Function of the aggregate interference power was provided in closed-form over generalized fading channels, and in several scenarios. Unfortunately, such an analytical modeling is not possible for the probability density function and the cumulative distribution function (CDF).
However, for infinite areas and non fading/Rayleigh fading channels, it was noted in [24] that the MGF of the aggregate interference power is the same as that of a *Stable Distribution* (see Appendix B):

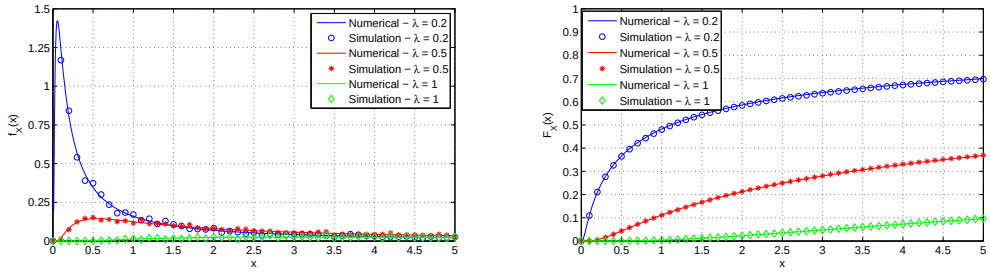

(a) pdf (b) CDF

Figure 1.5: pdf and CDF of $\mathcal{I}_\Phi$ for $\alpha = 5$ over an infinite area with no fading. Analytical model given by (1.42). Setup: i) $\lambda = 0.2, 0.5, 1$; and ii) $R_2 = 32$.

- for the non fading case, the interference follows a Stable distribution with characteristic exponent $\frac{d}{\alpha} < 1$, null drift, skew parameter $\beta = 1$, and dispersion $\gamma = \pi\lambda\Gamma\left(1 - \frac{d}{\alpha}\right)\cos\left(\frac{\pi d}{2}\right)$, and thus:

$$\mathcal{I}_\Phi \sim \mathcal{S}\left(\frac{d}{\alpha}, 1, c_d\lambda\Gamma\left(1 - \frac{d}{\alpha}\right)\cos\left(\frac{\pi d}{2}\right)\right)$$

- for the Rayleigh fading case, the only difference is in the fading coefficients affecting the dispersion, and thus

$$\mathcal{I}_\Phi \sim \mathcal{S}\left(\frac{d}{\alpha}, 1, c_d\lambda\mathbb{E}\left\{|\tilde{h}|^{d/\alpha}\right\}\Gamma\left(1 - \frac{d}{\alpha}\right)\cos\left(\frac{\pi d}{2}\right)\right)$$

Stable distributions do not have any finite moment. In particular, the mean interference diverges due to the singularity of the path-loss model in the origin, as also stated in Section 1.3.5. For $\alpha = 4$ and $d = 2$, the interference follows a Lévy distribution, one of the Stable distributions for which closed-form expressions of pdf and CDF exist, and thus for the non fading channel model:

$$\begin{aligned} f_{\mathcal{I}_\Phi}(x) &= \frac{\pi\lambda}{2x^{3/2}}\exp\left(-\frac{\pi^3\lambda^2}{4x}\right) \\ F_{\mathcal{I}_\Phi}(x) &= \operatorname{erfc}\left(\frac{\pi^{3/2}\lambda}{2\sqrt{x}}\right) \end{aligned} \tag{1.42}$$

while for Rayleigh fading:

$$\begin{aligned} f_{\mathcal{I}_\Phi}(x) &= \frac{\pi^{3/2}\lambda}{4x^{3/2}}\exp\left(-\frac{\pi^4\lambda^2}{16x}\right) \\ F_{\mathcal{I}_\Phi}(x) &= \operatorname{erfc}\left(\frac{\pi^2\lambda}{4\sqrt{x}}\right) \end{aligned} \tag{1.43}$$

Figure 1.4 provides the pdf and CDF of the Lévy distributed interference for several values of the density λ. For all the other cases, the pdf and CDF of the aggregate interference power can be obtained through a numerical approximation based on the inversion of the Laplace transform of a positive random variable [39]. As stated in Appendix A, the Laplace transform of a PPP coincides with its Moment Generating Function, and thus applying [39, Eq.(9)] and noting that $\hat{F}_{\mathcal{I}_\Phi}(s) = \hat{f}_{\mathcal{I}_\Phi}(s)/s$:

$$\begin{aligned} f_{\mathcal{I}_\Phi}(x) &= \sum_{q=0}^{Q} 2^{-Q} \binom{Q}{q} \left[\frac{e^{A/2}}{x} \sum_{n=0}^{N+q} \frac{(-1)^n}{\beta_n} \Re\left\{ \mathcal{M}_{\mathcal{I}_\Phi}\left(\frac{A + j2\pi n}{2x} \right) \right\} \right] \\ &\quad + E(A) + E(N,Q) \\ F_{\mathcal{I}_\Phi}(x) &= \sum_{q=0}^{Q} 2^{-Q} \binom{Q}{q} \left[\frac{e^{A/2}}{x} \sum_{n=0}^{N+q} \frac{(-1)^n}{\beta_n} \Re\left\{ \frac{\mathcal{M}_{\mathcal{I}_\Phi}\left(\frac{A+j2\pi n}{2x} \right)}{\frac{A+j2\pi n}{2x}} \right\} \right] \\ &\quad + E(A) + E(N,Q) \end{aligned} \tag{1.44}$$

where $\beta_n = 2$ if $n = 0$ and 1 otherwise, and the errors $E(A)$, $E(N,Q)$ are defined as follows:

$$|E(A)| \leq |e^{-A}/(1 - e^{-A})| \approx e^{-A}$$

$$E(N,Q) = \frac{e^{A/2}}{x} \sum_{q=0}^{Q} 2^{-Q} (-1)^{N+q+1} \binom{Q}{q} \cdot \Re\left\{ \mathcal{M}_{\mathcal{I}_\Phi}\left(\frac{A + j2\pi(N+q+1)}{2x} \right) \right\}$$

An application of the above numerical inversion is provided in Figure 1.5.

Chapter 2

Coverage Probability in Cellular Networks

In [22], Andrews, Baccelli and Ganti introduced a new analytical approach to estimate coverage and rate in cellular networks subject to inter-cell interference using stochastic geometry. More specifically, the positions of the Base Stations (BSs) of a cellular deployment are modeled as a homogeneous Poisson Point Process with fixed density. By averaging over the random positions of the BSs, the authors provide integral expressions of coverage and rate of a generic probe (intended) link. In particular, the authors provide a single integral expression of the coverage and a three-fold integral expression of the rate, which is useful when the intended link experiences Rayleigh fading. These results are highly remarkable, as they avoid lengthy and expensive numerical simulations. The comparison with the coverage probability and the achievable rate of an actual 4th generation (4G) cellular deployment is shown to substantiate the accuracy of the proposed approach. Numerical results show that using stochastic geometry provides a conservative (*i.e.* a lower-bound) estimate of the actual coverage and rate, with the main advantage of flexibility and reproducibility. In this thesis, starting from the approach proposed in [22] and using the results obtained in Chapter 1, a closed-form expression of the coverage and a single-integral expression of the rate, which can be used for arbitrary network and channel parameters (*e.g.* path-loss exponent, receiver noise, density of BSs, etc), is derived [1]. In this chapter, the focus is on the coverage probability, while the results on the average rate are provided in Chapter 3.

2.1 System Model

Similarly to [22], consider a 2D cellular network deployment with BSs and Mobile Stations (MSs) distributed according to two independent homogeneous Poisson Point Processes of densities λ_{BS} and λ_{MS}, respectively. It is assumed that each MS is connected (*i.e.*, communicates) with its nearest BS, while all the other BSs act as interferers. The scope of this chapter is computing the coverage probability of a generic probe (intended) link between a given BS and a given MS (downlink scenario). Since the intended terminal can be seen as a "typical" MS, it can be assumed located at the origin of the 2D Euclidean plane without any loss of generality (see Slivnyak's Theorem, Section A.3). However, it is assumed that, for each network realization, the distance between intended BS and MS is not fixed, but changes according to the actual position of its closest BS. More specifically, node mobility is not considered in this thesis, and the objective is estimating the coverage probability of an "average" cellular network configuration, i.e., by averaging over all possible network configurations [27]. Please note that, even if considering a cellular network, the scenario depicted above also describes a cognitive radio network in which a given number of randomly located Access Points (APs) provides a certain service to a Poisson distributed set of receiving nodes.

2.1.1 Channel Model

The following assumptions hold for the proposed analysis:

- an exponential-decaying path-loss model with $\alpha > 2$, common to all the links of the network, is considered [36];
- the constant transmit power of the intended and interfering BSs are denoted by P_0 and P_I respectively, and P_I is assumed to be the same for all the interfering BSs. Furthermore, $\rho_{BS} = P_I/P_0$ denotes the ratio between the transmitted power of the interfering and the intended BSs;
- the complex channel gain of the intended link, h_0, is assumed to have a Rayleigh fading distribution. The pdf of its square envelope is thus given by $f_{|h_0|^2}(\xi) = (1/\Omega_0)\exp(-\xi/\Omega_0)$, where $\Omega_0 = \mathbb{E}_{|h_0|^2}\left\{|h_0|^2\right\} = R_0^{-\alpha}$ with R_0 being the distance between the intended BS and MS;
- the complex channel gain of the i-th interfering BS is denoted by h_i for $i \in \Phi_{\mathrm{BS}}^{\{\setminus \mathrm{BS}_0\}}$, where $\Phi_{\mathrm{BS}}^{\{\setminus \mathrm{BS}_0\}}$ denotes the homogeneous PPP of all the BSs

in the Euclidean plane except the BS of the intended link, BS_0[1]. As the interfering links experience Rayleigh fading, the pdf of the square envelope $|h_i|^2$ for $i \in \Phi_{\mathrm{BS}}^{\{\backslash \mathrm{BS}_0\}}$ is denoted by $f_{|h_i|^2}(\xi) = (1/\Omega_i)\exp(-\xi/\Omega_i)$, where $\Omega_i = \mathbb{E}_{|h_i|^2}\left\{|h_i|^2\right\} = R_i^{-\alpha}$ and R_i is the distance between the i-th interfering BS and the intended MS;

- all the BSs deployed in the Euclidean plane are always transmitting,*i.e.* $p = 1$, and a constant envelope modulation is assumed, *i.e.* $b_j = 1, \forall j = 1, \ldots, M$;
- the noise at the intended MS is modeled as AWGN with power σ_N^2, and the Signal-to-Noise-Ratio (SNR) is given by $\gamma_0 = P_0/\sigma_N^2$.

According to the above assumptions, the aggregate interference received at the intended node from all the interfering BSs is given by:

$$\mathcal{I} = \sum_{i \in \Phi_{\mathrm{BS}}^{\{\backslash \mathrm{BS}_0\}}} |\tilde{h}_i|^2 R_i^{-\alpha}$$

It is worthwhile noting that the above equation shows the aggregate interference *power* when the interfering signals coming from all the interfering nodes are synchronous with the useful signal received at the intended node. In Chapter 4, the aggregate interference will be characterized in both synchronous and asynchronous scenarios for the computation of the Average Symbol Error Probability (ASEP), and further details on the connection between these two models will be provided.

2.1.2 Problem Statement

In this section, the analytical approach proposed in [22] is briefly described, as it provides the starting point for the simplified framework. The coverage probability for the downlink scenario in a cellular network can be defined as:

$$p_c(T, \lambda_{BS}, \alpha) \triangleq \mathbb{P}\{\mathrm{SINR} > T\} \tag{2.1}$$

and it can equivalently be thought of as (i) the probability that a randomly chosen user achieves a target Signal-to-Interference plus Noise-Ratio (SINR) T, (ii) the average fraction of users who achieve the target SINR T, or (iii) the average fraction of the network which can be considered in coverage according to the SINR threshold. It can be noted that the coverage probability is given by the Complementary

[1]Please note that $i \in \Phi_{\mathrm{BS}}^{\{\backslash \mathrm{BS}_0\}}$ is equivalent to $\mathbf{x}_i \in \Phi_{\mathrm{BS}}^{\{\backslash \mathrm{BS}_0\}}$.

CDF (CCDF) of the SINR evaluated at the threshold T, as the CDF is defined as $\mathbb{P}\{\text{SINR} \leq T\}$. The SINR of a mobile user located at a distance r from its intended BS is given by:

$$\text{SINR} = \frac{P_0 |\tilde{h}_0|^2 r^{-\alpha}}{\sigma_N^2 + P_I \mathcal{I}\left(r, \Phi_{\text{BS}}^{\{\setminus \text{BS}_0\}}\right)} \tag{2.2}$$

where $\tilde{h}_0 = h_0/\sqrt{\Omega_0}$ is the normalized fading gain of the intended link and:

$$\mathcal{I}_{r,\Phi} = \mathcal{I}\left(r, \Phi_{\text{BS}}^{\{\setminus \text{BS}_0\}}\right) = \sum_{i \in \Phi_{\text{BS}}^{\{\setminus \text{BS}_0\}}} |h_i|^2 = \sum_{i \in \Phi_{\text{BS}}^{\{\setminus \text{BS}_0\}}} |\tilde{h}_i|^2 R_i^{-\alpha} \tag{2.3}$$

is the aggregate interference power as defined in equation (1.1), conditioned on the distance $r = R_0$ between the intended BS and MS. More specifically, this is the aggregate interference generated by all the interfering BSs which fall outside the disc of radius R_0, $b(o, R_0)$. Similarly to the intended link, the normalized fading gain $\tilde{h}_i = h_i/\sqrt{\Omega_i}$ was introduced.
It can be noticed that the distance r separating a typical user from its intended BS is a fundamental parameter. Since each user communicates with the closest BS, no other BS can be closer than r. The CDF (and consequently the pdf) of r can thus be easily derived using the void probability of a 2D Poisson process (Section A.2):

$$\begin{aligned} F_{R_0}(r) &= 1 - \mathbb{P}\{\text{no BS closer than r}\} = 1 - e^{-\pi \lambda_{BS} r^2} \\ f_{R_0}(r) &= \frac{\mathrm{d}F_{R_0}(r)}{\mathrm{d}r} = 2\pi\lambda_{BS} e^{-\pi \lambda_{BS} r^2} r \end{aligned} \tag{2.4}$$

Thanks to the above pdf, the coverage probability can be evaluated by first conditioning on the nearest BS being at distance r from the typical user (proof of [22, Theorem 1]):

$$\begin{aligned} p_c(T, \lambda_{BS}, \alpha) &= \int_0^\infty \mathbb{P}\{\text{SINR} > T | r\} f_{R_0}(r) \mathrm{d}r \\ &\overset{(a)}{=} 2\pi\lambda_{BS} \int_0^\infty e^{-\pi \lambda_{BS} r^2} \underbrace{\mathbb{P}\left\{ |\tilde{h}_0|^2 > \frac{T r^\alpha \left(\sigma_N^2 + P_I \mathcal{I}_{r,\Phi}\right)}{P_0} \middle| r \right\}}_{\mathcal{P}} r \mathrm{d}r \end{aligned}$$

where (a) follows from equation (2.4). The probability $\mathcal{P}$ inside the above integral can be solved as follows:

$$\begin{aligned}\mathcal{P} &= \mathbb{E}_{\Phi_{\text{BS}}^{\{\setminus \text{BS}_0\}}}\left\{\mathbb{P}\left\{|\tilde{h}_0|^2 > \frac{Tr^\alpha\left(\sigma_N^2 + P_I\mathcal{I}_{r,\Phi}\right)}{P_0}\middle| r, \Phi_{\text{BS}}^{\{\setminus \text{BS}_0\}}\right\}\right\} \\ &\overset{(a)}{=} \mathbb{E}_{\Phi_{\text{BS}}^{\{\setminus \text{BS}_0\}}}\left\{\exp\left[-Tr^\alpha\left(\frac{1}{\gamma_0} + \frac{P_I}{P_0}\mathcal{I}_{r,\Phi}\right)\right]\middle| r, \Phi_{\text{BS}}^{\{\setminus \text{BS}_0\}}\right\} \\ &\overset{(b)}{=} e^{-Tr^\alpha/\gamma_0}\mathcal{M}_{\mathcal{I}_{r,\Phi}}\left(Tr^\alpha\rho_{BS}\right)\end{aligned}$$

where (a) follows from the CDF of the normalized fading gain on the intended link, which assuming a Rayleigh fading channel is exponentially distributed with unitary mean, *i.e.* $f_{|\tilde{h}_i|^2}(\xi) = \exp(-\xi)$, and (b) follows from the definition of Moment Generating Function (1.4). Note that the expectation over the PPP $\Phi_{\text{BS}}^{\{\setminus \text{BS}_0\}}$ implies to compute the average over both $|\tilde{h}_i|^2$ and R_i for $i \in \Phi_{\text{BS}}^{\{\setminus \text{BS}_0\}}$. Substituting the above expression in the previous integral:

$$p_c(T, \lambda_{BS}, \alpha) = 2\pi\lambda_{BS}\int_0^\infty e^{-\pi\lambda_{BS}r^2}e^{-Tr^\alpha/\gamma_0}\mathcal{M}_{\mathcal{I}_{r,\Phi}}\left(Tr^\alpha\rho_{BS}\right)r\mathrm{d}r \tag{2.5}$$

where $\mathcal{M}_{\mathcal{I}_{r,\Phi}}$ is the MGF of $\mathcal{I}_{r,\Phi}$ evaluated between r and the infinity, *i.e.* in an exclusion region as in Section 1.3.4.3. By writing this MGF as the MGF of a Poisson Point Process (see Section A.2), in [22, Theorem 1] the authors provide the following single-integral expression for the coverage probability:

$$p_c(T, \lambda_{BS}, \alpha) = \pi\lambda_{BS}\int_0^\infty e^{-\pi\lambda_{BS}v\beta(T,\alpha) - Tv^{\alpha/2}/\gamma_0}\mathrm{d}v \tag{2.6}$$

where

$$\beta(T,\alpha) = \frac{2(T\rho_{BS})^{\frac{2}{\alpha}}}{\alpha}\mathbb{E}_{|\tilde{h}_i|^2}\left\{|\tilde{h}_i|^{\frac{4}{\alpha}}\left(\Gamma\left(-\frac{2}{\alpha}, T|\tilde{h}_i|^2\rho_{BS}\right) - \Gamma\left(-\frac{2}{\alpha}\right)\right)\right\} \tag{2.7}$$

2.2 Closed-form Expression with Rayleigh Fading

In Chapter 1, a closed-form expression of $\mathcal{M}_{\mathcal{I}_{r,\Phi}}$ was obtained for several scenarios and fading models. In particular, the MGF in an exclusion region over Rayleigh fading channels was provided in equation (1.34). By evaluating it for $s = Tr^\alpha\rho_{BS}$, the MGF in equation (2.5) becomes:

$$\begin{aligned}\mathcal{M}_{\mathcal{I}_{r,\Phi}}\left(Tr^\alpha\rho_{BS}\right) = \exp\left[\pi\lambda_{BS}r^2\right] \times \exp\left[-\frac{\pi\lambda_{BS}r^2}{1+T\rho_{BS}}\right] \\ \times \exp\left[-\frac{\pi\lambda_{BS}T\rho_{BS}r^2}{\left(1+T\rho_{BS}\right)^2}\frac{{}_2F_1\left(2;1;2-\frac{2}{\alpha};\frac{T\rho_{BS}}{1+T\rho_{BS}}\right)}{1-\frac{2}{\alpha}}\right]\end{aligned} \tag{2.8}$$

Plugging (2.8) into (2.5) yields to:

$$p_c(T,\lambda_{BS},\alpha) = 2\pi\lambda_{BS}\int_0^\infty \left\{ r\exp\left[-\frac{Tr^\alpha}{\gamma_0}\right] \times \exp\left[-\frac{\pi\lambda_{BS}r^2}{1+T\rho_{BS}}\right] \times \exp\left[-\frac{\pi\lambda_{BS}T\rho_{BS}r^2}{(1+T\rho_{BS})^2}\frac{{}_2F_1\left(2;1;2-\frac{2}{\alpha};\frac{T\rho_{BS}}{1+T\rho_{BS}}\right)}{1-\frac{2}{\alpha}}\right]\right\} \mathrm{d}r$$

Switching the variables as $r^2 \to v$, finally provides the following form of the coverage probability:

$$p_c(T,\lambda_{BS},\alpha) = \pi\lambda_{BS}\int_0^\infty e^{-k_1 v}e^{-k_2 v^{\alpha/2}}\mathrm{d}v \tag{2.9}$$

where:

$$\begin{aligned} k_1 &= \pi\lambda_{BS}\left[\frac{1}{1+T\rho_{BS}} + \frac{T\rho_{BS}}{(1+T\rho_{BS})^2}\frac{{}_2F_1\left(2;1;2-\frac{2}{\alpha};\frac{T\rho_{BS}}{1+T\rho_{BS}}\right)}{1-\frac{2}{\alpha}}\right] \\ k_2 &= \frac{T}{\gamma_0} \end{aligned} \tag{2.10}$$

An alternative simpler form of the coefficient k_1 can be found starting from the definition of $\beta(T,\alpha)$ in equation (2.7). Applying the series expansion of the upper incomplete Gamma function (equation (1.16)), the expectation in (2.7) is given by:

$$\begin{aligned} \mathcal{T}_3 &= \mathbb{E}_{|\tilde{h}_i|^2}\left\{|\tilde{h}_i|^{\frac{4}{\alpha}}\left(\Gamma\left(-\frac{2}{\alpha},T|\tilde{h}_i|^2\rho_{BS}\right)-\Gamma\left(-\frac{2}{\alpha}\right)\right)\right\} \\ &= -\mathbb{E}_{|\tilde{h}_i|^2}\left\{|\tilde{h}_i|^{\frac{4}{\alpha}}\Gamma\left(-\frac{2}{\alpha}\right)\left(T\rho_{BS}|\tilde{h}_i|^2\right)^{-\frac{2}{\alpha}}e^{-T\rho_{BS}|\tilde{h}_i|^2}\sum_{k=0}^{\infty}\frac{\left(T\rho_{BS}|\tilde{h}_i|^2\right)^k}{\Gamma\left(k+1-\frac{2}{\alpha}\right)}\right\} \end{aligned}$$

Proceeding as in Section 1.3.1, $\mathcal{T}_3$ can be evaluated in closed-form as follows:

$$\begin{aligned} \mathcal{T}_3 &= -(T\rho_{BS})^{-\frac{2}{\alpha}}\Gamma\left(-\frac{2}{\alpha}\right)\sum_{k=0}^{\infty}\frac{(T\rho_{BS})^k}{\Gamma\left(k+1-\frac{2}{\alpha}\right)}\mathbb{E}_{|\tilde{h}_i|^2}\left\{|\tilde{h}_i|^{2k}e^{-T\rho_{BS}|\tilde{h}_i|^2}\right\} \\ &\overset{(a)}{=} -(T\rho_{BS})^{-\frac{2}{\alpha}}\Gamma\left(-\frac{2}{\alpha}\right)\sum_{k=0}^{\infty}\frac{(T\rho_{BS})^k}{\Gamma\left(k+1-\frac{2}{\alpha}\right)}\frac{\rho_{BS}\Gamma(k+1)}{(\rho_{BS}(T+1))^{(k+1)}} \\ &\overset{(b)}{=} (T\rho_{BS})^{-\frac{2}{\alpha}}\frac{{}_2F_1\left(1;1;1-\frac{2}{\alpha};\frac{T\rho_{BS}}{1+T\rho_{BS}}\right)}{(1+T\rho_{BS})\left(\frac{2}{\alpha}\right)} \end{aligned}$$

where (a) follows from the known integral $\mathbb{E}_{|\tilde{h}_i|^2}\left\{|\tilde{h}_i|^{2k}e^{-T\rho_{BS}|\tilde{h}_i|^2}\right\} = \frac{\Gamma(k+1)}{(1+T\rho_{BS})^{(k+1)}}$, and (b) from the infinite series representation of the Gauss' hypergeometric function

in [38, Eq.(15.1.1)] and the known equality $\Gamma(z+1) = z\Gamma(z)$. Substituting the above expression in (2.7), $\beta(T,\alpha)$ becomes:

$$\beta(T,\alpha) = \frac{{}_2F_1\left(1;1;1-\frac{2}{\alpha};\frac{T\rho_{BS}}{1+T\rho_{BS}}\right)}{(1+T\rho_{BS})} \tag{2.11}$$

In conclusion, the coverage probability over Rayleigh fading channels is given by:

$$\begin{aligned} p_c(T,\lambda_{BS},\alpha) &= \pi\lambda_{BS}\int_0^\infty e^{-k_1 v}e^{-k_2 v^{\alpha/2}}\mathrm{d}v \\ k_1 &= \pi\lambda_{BS}\left[\frac{1}{1+T\rho_{BS}} + \frac{T\rho_{BS}}{(1+T\rho_{BS})^2}\frac{{}_2F_1\left(2;1;2-\frac{2}{\alpha};\frac{T\rho_{BS}}{1+T\rho_{BS}}\right)}{1-\frac{2}{\alpha}}\right] \\ &\equiv \pi\lambda_{BS}\frac{{}_2F_1\left(1;1;1-\frac{2}{\alpha};\frac{T\rho_{BS}}{1+T\rho_{BS}}\right)}{(1+T\rho_{BS})} \\ k_2 &= \frac{T}{\gamma_0} \end{aligned} \tag{2.12}$$

2.2.1 Meijer-G Function

The single-integral form of the coverage probability over Rayleigh fading channels proposed in equation (2.12) can be solved in closed-form by simply applying the integration properties of the Meijer-G function. It is a general function including most of the known special functions as particular cases, like the Hypergeometric function or MacRobert's E-function, and can be used to express almost all the most significant solutions of a hypergeometric differential equation. The Meijer-G function is defined as the following path integral on the complex plane:

$$G_{p,q}^{m,n}\left(x\left|\begin{matrix}a_1,a_2,\ldots,a_p\\ \\ b_1,b_2,\ldots,b_q\end{matrix}\right.\right) = \frac{1}{2\pi j}\int_L \frac{\prod_{i=1}^{m}\Gamma(b_i-s)\prod_{i=1}^{n}\Gamma(1-a_i+s)}{\prod_{i=m+1}^{q}\Gamma(1-b_i+s)\prod_{i=n+1}^{p}\Gamma(a_i-s)}x^s\mathrm{d}s \tag{2.13}$$

where an empty product is interpreted as 1, $0 \le m \le q$, $0 \le n \le p$, $m,n,p,q = 0,1,\ldots$, and the parameters are such that no pole of $\Gamma(b_i-s)$, $i=1,\ldots,m$, coincides with any pole of $\Gamma(1-a_k+s)$, $k=1,\ldots,n$. For detailed information on the Meijer-G function, the reader can refer to [40–42].

In [42] many integrals involving the Meijer-G function are solved as Meijer-G functions with different parameters. The advantage of this approach is that the Meijer-G

function is already efficiently implemented in standard mathematical software packages, such as Maple and Mathematica, and it can thus be easily handled. In [42, Eq.(2.24.1.1)], the following integral is provided:

$$\int_0^\infty x^{\delta-1}e^{-\sigma x}G_{p,q}^{m,n}\left(\omega x^{l/k}\left|\begin{matrix}\mathbf{a}_p\\ \mathbf{b}_q\end{matrix}\right.\right)\mathrm{d}x = \\ = \frac{k^\mu\, l^{\left(\delta-\frac{1}{2}\right)}\sigma^{-\delta}}{(2\pi)^{\left(\frac{l-1}{2}+c^*(k-1)\right)}}G_{kp+l,kq}^{km,kn+l}\left(\frac{\omega^k\; l^l}{\sigma^l\; k^{k(q-p)}}\left|\begin{matrix}\Delta(l,1-\delta),\Delta(k,\mathbf{a}_p)\\ \Delta(k,\mathbf{b}_q)\end{matrix}\right.\right) \tag{2.14}$$

where $k, l = 1, 2, \ldots$ and:

$$\begin{aligned} c^* &= m+n-\frac{p+q}{2} \\ \mu &= \sum_{i=1}^{q} b_i - \sum_{i=1}^{p} a_i + \frac{p-q}{2} + 1 \\ \Delta(k,1-\delta) &= \frac{1-\delta}{k}, \frac{2-\delta}{k}, \ldots, \frac{k-\delta}{k} \\ \Delta(k,\mathbf{x}) &= \frac{\mathbf{x}}{k}, \frac{\mathbf{x}+1}{k}, \ldots, \frac{\mathbf{x}+k-1}{k}, \text{for } \mathbf{x}=\mathbf{a}_\mathrm{p}, \mathbf{b}_\mathrm{q} \end{aligned} \tag{2.15}$$

The integral in (2.14) is the same as that in (2.12). As a matter of facts, by writing the second exponential as a Meijer-G function thanks to [42, Eq.(8.4.3.1)], $e^{-k_2 v^{\alpha/2}} = G_{0,1}^{1,0}\left(k_2 v^{\alpha/2}\left|\begin{matrix}-\\ 0\end{matrix}\right.\right)$, the coverage probability can be written as:

$$p_c(T,\lambda_{BS},\alpha) = \pi\lambda_{BS}\int_0^\infty e^{-k_1 v}G_{0,1}^{1,0}\left(k_2 v^{\alpha/2}\left|\begin{matrix}-\\ 0\end{matrix}\right.\right)\mathrm{d}v$$

Comparing the above expression with equation (2.14), the parameters in (2.15) become: $\delta = 1$, $\sigma = k_1$, $\omega = k_2$, $p = n = 0$, $q = m = 1$, $c^* = \mu = \frac{1}{2}$, $\mathbf{a}_p = (-)$, $\mathbf{b}_q = 0$ and

$$\begin{aligned} \Delta(l,1-\delta) &= 0, \frac{1}{l}, \ldots, \frac{l-1}{l} \\ \Delta(k,\mathbf{a}_p) &= (-) \\ \Delta(k,\mathbf{b}_q) &= 0, \frac{1}{k}, \ldots, \frac{k-1}{k} \end{aligned}$$

and thus the coverage probability is given by the following closed-form expression:

$$p_c(T,\lambda_{BS},\alpha) = \pi\lambda_{BS}\frac{\sqrt{k_\alpha l_\alpha}}{k_1(2\pi)^{\left(\frac{k_\alpha+l_\alpha}{2}-1\right)}}G_{l_\alpha,k_\alpha}^{k_\alpha,l_\alpha}\left(\frac{k_2^{k_\alpha}l_\alpha^{l_\alpha}}{k_1^{l_\alpha}k_\alpha^{k_\alpha}}\left|\begin{matrix}\mathbf{a}\\ \mathbf{b}\end{matrix}\right.\right) \tag{2.16}$$

where $\mathbf{a} = 0, \frac{1}{l_\alpha}, \ldots, \frac{l_\alpha-1}{l_\alpha}$, $\mathbf{b} = 0, \frac{1}{k_\alpha}, \ldots, \frac{k_\alpha-1}{k_\alpha}$, and $\frac{2}{\alpha} = \frac{k_\alpha}{l_\alpha}$ with k_α, l_α being two positive integers.

2.2.2 Upper Bound

Analyzing the results obtained in the previous sections, an Upper Bound for the coverage probability can be easily obtained according to two different approaches:

1. by setting $e^{-k_2 v^{\alpha/2}} = 1$ in equation (2.12), the integral provides an upper bound as:

$$p_c^{(UB)}(T, \lambda_{BS}, \alpha) = \pi\lambda_{BS} \int_0^\infty e^{-k_1 v} \mathrm{d}v = \frac{\pi\lambda_{BS}}{k_1} = \frac{1 + T\rho_{BS}}{{}_2F_1\left(1; 1; 1 - \frac{2}{\alpha}; \frac{T\rho_{BS}}{1+T\rho_{BS}}\right)} \tag{2.17}$$

2. A different methodology consists in integrating by parts in equation (2.12). This operation also allows to obtain a closed-form expression of the error introduced using the Upper Bound:

$$\begin{aligned} p_c(T, \lambda_{BS}, \alpha) &= \pi\lambda_{BS} \int_0^\infty e^{-k_1 v} e^{-k_2 v^{\alpha/2}} \mathrm{d}v \\ &= \frac{\pi\lambda_{BS}}{k_1} - \pi\lambda_{BS} \frac{\alpha}{2} \frac{k_2}{k_1} \int_0^\infty v^{\alpha/2-1} e^{-k_1 v} e^{-k_2 v^{\alpha/2}} \mathrm{d}v \\ &= p_c^{(UB)}(T, \lambda_{BS}, \alpha) - \pi\lambda_{BS} \frac{\alpha}{2} \frac{k_2}{k_1} \int_0^\infty v^{\alpha/2-1} e^{-k_1 v} e^{-k_2 v^{\alpha/2}} \mathrm{d}v \end{aligned}$$

   The second term can be evaluated using once again the Meijer-G function, applying equation (2.14), yielding to:

$$p_c(T, \lambda_{BS}, \alpha) = \frac{\pi\lambda_{BS}}{k_1} - \pi\lambda_{BS} \frac{\alpha}{2} \frac{k_2 \sqrt{k_\alpha l_\alpha^{(\alpha-1)}}}{k_1^{\left(\frac{\alpha}{2}+1\right)} (2\pi)^{\left(\frac{k_\alpha + l_\alpha}{2} - 1\right)}} G_{l_\alpha, k_\alpha}^{k_\alpha, l_\alpha} \left(\left. \begin{matrix} \frac{k_2^{k_\alpha}}{k_1^{l_\alpha}} & \frac{l_\alpha^{l_\alpha}}{k_\alpha^{k_\alpha}} \end{matrix} \right| \begin{matrix} \mathbf{a}' \\ \mathbf{b}' \end{matrix} \right) \tag{2.18}$$

   where $\mathbf{a}' = \frac{1-\frac{\alpha}{2}}{l_\alpha}, \ldots, \frac{l_\alpha - \frac{\alpha}{2}}{l_\alpha}$ and $\mathbf{b}' = 0, \frac{1}{k_\alpha}, \ldots, \frac{k_\alpha - 1}{k_\alpha}$.

It is worthwhile noting that the Upper Bound depends only on the SINR threshold T, the ratio ρ_{BS} and the path-loss exponent α, and neither on the SNR, γ_0, or the BSs density, λ_{BS}. In order to analyze the accuracy of this bound, an asymptotical analysis of equation (2.18) is needed. In particular, it can be noticed that the Upper Bound is more accurate when the second term tends to zero, *i.e.* when:

$$\pi\lambda_{BS} \frac{\alpha}{2} \underbrace{\frac{k_1}{k_1^{\left(\frac{\alpha}{2}+1\right)}}}_{X(T,\gamma_0)} \frac{\sqrt{k_\alpha l_\alpha^{(\alpha-1)}}}{(2\pi)^{\left(\frac{k_\alpha + l_\alpha}{2} - 1\right)}} G_{l_\alpha, k_\alpha}^{k_\alpha, l_\alpha} \left(\left. \begin{matrix} \underbrace{\frac{k_2^{k_\alpha}}{k_1^{l_\alpha}}}_{Y(T,\gamma_0)} & \frac{l_\alpha^{l_\alpha}}{k_\alpha^{k_\alpha}} \end{matrix} \right| \begin{matrix} \mathbf{a}' \\ \mathbf{b}' \end{matrix} \right) \to 0 \tag{2.19}$$

The behaviour of the above limit depends on two different ratios of the coefficients k_1 and k_2. These two ratios depend on the SINR threshold T, the SNR γ_0, the ratio ρ_{BS}, the path-loss exponent α and the density λ_{BS}. However, considering that usually $2 < \alpha < 5$ and $0 < \lambda_{BS} < 1$, and that $\rho_{BS} > 0$, these parameters do not affect the limit behaviour of X and Y, which are thus denoted as functions of T and γ_0 only:

$$\begin{aligned} X(T,\gamma_0) &= \frac{k_2}{k_1^{\left(\frac{\alpha}{2}+1\right)}} = \frac{T(1+T\rho_{BS})^{\left(\frac{\alpha}{2}+1\right)}}{\gamma_0\left[\pi\lambda_{BS}{}_2F_1\left(1;1;1-\frac{2}{\alpha};\frac{T\rho_{BS}}{1+T\rho_{BS}}\right)\right]^{\left(\frac{\alpha}{2}+1\right)}} \\ Y(T,\gamma_0) &= \frac{k_2^{k_\alpha}}{k_1^{l_\alpha}} \propto \frac{k_2}{k_1^{l_\alpha/k_\alpha}} = \frac{T(1+T\rho_{BS})^{l_\alpha/k_\alpha}}{\gamma_0\left[\pi\lambda_{BS}{}_2F_1\left(1;1;1-\frac{2}{\alpha};\frac{T\rho_{BS}}{1+T\rho_{BS}}\right)\right]^{l_\alpha/k_\alpha}} \end{aligned}$$

The limit behaviour of this two functions is now provided for several cases:

- $T \to 0$, $\gamma_0 < \infty$. In this situation, the Hypergeometric function has the following limit:

$$\lim_{T\to 0} {}_2F_1\left(1;1;1-\frac{2}{\alpha};\frac{T\rho_{BS}}{1+T\rho_{BS}}\right) = {}_2F_1\left(1;1;1-\frac{2}{\alpha};0\right) = 1$$

  and thus for finite values of γ_0:

$$\begin{aligned} \lim_{T\to 0} X(T,\gamma_0) &= \frac{T(1+T\rho_{BS})^{\left(\frac{\alpha}{2}+1\right)}}{\gamma_0(\pi\lambda_{BS})^{\left(\frac{\alpha}{2}+1\right)}} = 0 \\ \lim_{T\to 0} Y(T,\gamma_0) &= \frac{T(1+T\rho_{BS})^{l_\alpha/k_\alpha}}{\gamma_0(\pi\lambda_{BS})^{l_\alpha/k_\alpha}} = 0 \end{aligned}$$

  The Meijer-G function has non-zero finite limit values, but, as the multiplying coefficients tend to zero, the limit (2.19) tends to zero, and the coverage probability tends to the Upper Bound.

- $T < \infty$, $\gamma_0 \to \infty$. This case is straightforward, as the SNR only appears in the denominator of both $X(T,\gamma_0)$ and $Y(T,\gamma_0)$: the limit (2.19) tends to zero, and also in this case the coverage probability tends to the Upper Bound.

- $T \to \infty$, $\gamma_0 < \infty$. In this case, a series expansion of the Hypergeometric function for $T \to \infty$ is extremely useful. Stopping this series at the first order

provides:

$$
\begin{aligned}
&{}_2F_1\left(1;1;1-\frac{2}{\alpha};\frac{T\rho_{BS}}{1+T\rho_{BS}}\right) \sim (T\rho_{BS})^{2/\alpha}\left(\frac{2\pi\csc\left[\pi\left(-1-\frac{2}{\alpha}\right)\right]T\rho_{BS}}{\alpha}\right.\\
&\left.-\frac{\pi\csc\left[\pi\left(-1-\frac{2}{\alpha}\right)\right]\cdot\left(2\alpha\Gamma\left[1-\frac{2}{\alpha}\right]+\alpha^2\Gamma\left[1-\frac{2}{\alpha}\right]+4\Gamma\left[-\frac{2}{\alpha}\right]\right)}{\alpha^2\Gamma\left[-\frac{2}{\alpha}\right]}+O\left[\frac{1}{T}\right]\right)\\
&+\left(\frac{\pi\csc\left[\pi\left(-1-\frac{2}{\alpha}\right)\right]\Gamma\left[1-\frac{2}{\alpha}\right]}{\Gamma\left[2+\frac{2}{\alpha}\right]\Gamma\left[-\frac{2}{\alpha}\right]^2}+\frac{\pi\csc\left[\pi\left(-1-\frac{2}{\alpha}\right)\right]\Gamma\left[1-\frac{2}{\alpha}\right]}{\Gamma\left[3+\frac{2}{\alpha}\right]\Gamma\left[-\frac{2}{\alpha}\right]^2T\rho_{BS}}+O\left[\frac{1}{T}\right]^2\right)
\end{aligned}
$$

Plugging the above series expansion into $X(T,\gamma_0)$ and $Y(T,\gamma_0)$:

$$
\begin{aligned}
\lim_{T\to\infty} X(T,\gamma_0) &= a<\infty\\
\lim_{T\to\infty} Y(T,\gamma_0) &= 0
\end{aligned}
$$

and thus also in this case the coverage probability tends to the Upper Bound.

2.2.3 On the computation of the Meijer-G Function

The computation of the coverage probability in equation (2.16) requires a software package that can efficiently handle the Meijer-G function. As already stated, this function is today efficiently implemented and available in standard mathematical software packages, such as Mathematica and Maple. For this reason, the Meijer-G function has been extensively used for the performance analysis of a large variety of wireless communication systems [43–46].

In general, the computation of single-integrals involving the Meijer-G function does not pose particular problems when the ergodic capacity or the error/outage probability are the performance metrics of interest. However, when computing (2.16), some numerical instabilities were found when the argument of the Meijer-G function takes very small values, *i.e.* when $\xi \to 0$ in $G_{p,q}^{m,n}\left(\xi\left|\begin{matrix}\mathbf{a}\\ \mathbf{b}\end{matrix}\right.\right)$. This behaviour was noticed for most of the common mathematical software packages, even tough some of them are more accurate than others, or need less computation time to achieve the same result. In general, numerical problems arise when $\xi < 10^{-2}$ or $\xi < 10^{-3}$. In particular, an exponential growth in computation time or no computation at all was noticed. For many systems setups, on the other hand, no numerical problems were encountered. However, it is worthwhile emphasizing that the results in (2.16) and (2.18) are exact and correct, and the numerical problems arise only due to the specific algorithm that is used to compute the Meijer-G function. This is the reason

why different mathematical software packages offer, in general, a different robustness to this problem.

To circumvent these numerical instabilities without loosing in accuracy, a simple solution is proposed. The idea is to avoid the computation of the Meijer-G function for $\xi \to 0$, by using, instead, a very accurate and asymptotically-tight approximation in this region. In particular, by applying [42, Eq.(8.2.2.14)], the argument of the Meijer-G function can be inverted as follows:

$$G_{p,q}^{m,n}\left(\xi \left| \begin{matrix} \mathbf{x} \\ \mathbf{y} \end{matrix} \right.\right) = G_{n,m}^{q,p}\left(\frac{1}{\xi} \left| \begin{matrix} 1-\mathbf{y} \\ 1-\mathbf{x} \end{matrix} \right.\right) \tag{2.20}$$

Applying the above inversion to equation (2.16) provides the following alternative form of the coverage probability:

$$p_c(T,\lambda_{BS},\alpha) = \frac{\pi\lambda BS}{k_1} - \pi\lambda_{BS}\frac{\alpha}{2}\frac{k_2\sqrt{k_\alpha l_\alpha^{(\alpha-1)}}}{k_1^{\left(\frac{\alpha}{2}+1\right)}(2\pi)^{\left(\frac{l_\alpha+k_\alpha}{2}-1\right)}}\underbrace{G_{k_\alpha,l_\alpha}^{l_\alpha,k_\alpha}\left(\frac{k_1^{l_\alpha}\ k_\alpha^{k_\alpha}}{k_2^{k_\alpha}\ l_\alpha^{l_\alpha}}\middle| \begin{matrix} 1-\mathbf{b}' \\ 1-\mathbf{a}' \end{matrix}\right)}_{\mathcal{U}_{cov}} \tag{2.21}$$

Thanks to the above form, it is possible to apply the series expansion as provided in [47, Theorem 1.8.3], which for arguments of the Meijer-G function tending to infinity states that if $1 \le n \le p < q$, $1 \le m \le q$ and:

$$\begin{aligned} c^* &= m+n-\frac{p}{2}-\frac{q}{2} > 0 \\ \mathbf{x}(d)-\mathbf{y}(h) &\neq 1,2,3,\ldots \ (d=1,\ldots,n; h=1,\ldots,m) \\ \mathbf{x}(d)-\mathbf{x}(h) &\neq 0,\pm1,\pm2,\ldots \ (d=1,\ldots,n; h=1,\ldots,m; d\neq h) \end{aligned} \tag{2.22}$$

then the Meijer-G function for its argument tending to infinity can be written as:

$$G_{p,q}^{m,n}\left(z \left| \begin{matrix} \mathbf{x} \\ \mathbf{y} \end{matrix} \right.\right) \sim \sum_{t=1}^{n} e^{-j\pi\mathbf{x}(t)(1+\mu^*)}\Delta_q^{m,n}(t)E_{p,q}\left[\, ze^{j\pi(1+\mu^*)}\middle|\middle|\, \mathbf{x}(t)\right] \tag{2.23}$$

where:

$$\begin{aligned} \Delta_q^{m,n}(t) &= (-1)^{m+n-q-1}\frac{\prod_{\substack{h=1\\h\neq t}}^{n}\left[\Gamma\left(\mathbf{x}(t)-\mathbf{x}(h)\right)\Gamma\left(1+\mathbf{x}(h)-\mathbf{x}(t)\right)\right]}{\prod_{h=m+1}^{q}\left[\Gamma\left(\mathbf{x}(t)-\mathbf{y}(h)\right)\Gamma\left(1+\mathbf{y}(h)-\mathbf{x}(t)\right)\right]} \\ E_{p,q}\left[\, w||\, \mathbf{x}(t)\right] &= \frac{w^{(\mathbf{x}(t)-1)}\prod_{h=1}^{q}\Gamma\left(1+\mathbf{y}(h)-\mathbf{x}(t)\right)}{\prod_{\substack{h=1\\h\neq t}}^{p}\Gamma\left(1+\mathbf{x}(h)-\mathbf{x}(t)\right)}{}_qF_{p-1}\left(\begin{matrix} 1+\mathbf{y}(h)-\mathbf{x}(t) \\ 1+\mathbf{x}(h)-\mathbf{x}(t)^* \end{matrix}\middle| w^{-1}\right) \end{aligned} \tag{2.24}$$

with $\mu^* = q - m - n$ and the * in the Generalized hypergeometric function ${}_qF_p(\cdot)$ meaning that the term $1 + \mathbf{x}(t) - \mathbf{x}(t)$ should not be considered. From now on, the factors related to the Generalized hypergeometric function will be neglected, as this function is very fast in tending to a unit value in the limiting region of interest. With reference to equation (2.21), the conditions for [47, Theorem 1.8.3] in (2.22) are satisfied, and the Meijer-G function in equation (2.21) can be simplified as:

$$\mathcal{U}_{cov} \to \mathcal{U}_{cov}^{(\infty)} = \sum_{t=1}^{k_\alpha} \mathcal{U}_{cov}^{(\infty)}(t) \tag{2.25}$$

where:

$$\begin{aligned}\mathcal{U}_{cov}^{(\infty)}(t) =& (-1)^{(k_\alpha - 1)} \times \exp\left[-j\pi\mathbf{x}(t)(1-k_\alpha)\right] \times \left(\frac{k_1^{l_\alpha}\, k_\alpha^{k_\alpha}}{k_2^{l_\alpha}\, l_\alpha^{l_\alpha}} \exp\left[j\pi(1-k_\alpha)\right]\right)^{(\mathbf{x}(t)-1)} \\ &\times \left[\prod_{\substack{q=1 \\ q\neq t}}^{k_\alpha} \Gamma\left(\mathbf{x}(t) - \mathbf{x}(q)\right) \Gamma\left(1 + \mathbf{x}(q) - \mathbf{x}(t)\right)\right] \times \left[\frac{\prod_{q=1}^{l_\alpha} \Gamma\left(1 + \mathbf{y}(q) - \mathbf{x}(t)\right)}{\prod_{\substack{q=1 \\ q\neq t}}^{k_\alpha} \Gamma\left(1 + \mathbf{x}(q) - \mathbf{x}(t)\right)}\right]\end{aligned} \tag{2.26}$$

with $\mathbf{x} = 1 - \mathbf{b}' = 1, \frac{k_\alpha - 1}{k_\alpha}, \ldots, \frac{1}{k_\alpha}$ and $\mathbf{y} = 1 - \mathbf{a}' = \frac{l_\alpha - 1 + \frac{\alpha}{2}}{l_\alpha}, \frac{l_\alpha - 2 + \frac{\alpha}{2}}{l_\alpha}, \ldots, \frac{\frac{\alpha}{2}}{l_\alpha}$. The coverage probability for small arguments of the Meijer-G function is thus given by:

$$p_c(T, \lambda_{BS}, \alpha)^{(\infty)} = \frac{\pi\lambda_{BS}}{k_1} - \pi\lambda_{BS}\frac{\alpha}{2}\frac{k_2\sqrt{k_\alpha l_\alpha^{(\alpha-1)}}}{k_1^{\left(\frac{\alpha}{2}+1\right)}(2\pi)^{\left(\frac{l_\alpha + k_\alpha}{2} - 1\right)}} \sum_{t=1}^{k_\alpha} \mathcal{U}_{cov}^{(\infty)}(t) \tag{2.27}$$

Finally, to solve the numerical problems outlined above, the following closed-form expression is proposed:

$$\begin{cases} p_c^{(\mathcal{H})}(T, \lambda_{BS}, \alpha) = \frac{\pi\lambda_{BS}}{k_1} - \pi\lambda_{BS}\frac{\alpha}{2}\frac{k_2\sqrt{k_\alpha l_\alpha^{(\alpha-1)}}}{k_1^{\left(\frac{\alpha}{2}+1\right)}(2\pi)^{\left(\frac{l_\alpha + k_\alpha}{2} - 1\right)}}\mathcal{U}_{cov}^{(\mathcal{H})} \\ \\ \mathcal{U}_{cov}^{(\mathcal{H})} = \mathcal{U}_{cov}\mathcal{H}\left(\frac{k_1^{l_\alpha}\, k_\alpha^{k_\alpha}}{k_2^{k_\alpha}\, l_\alpha^{l_\alpha}} - \varepsilon\right) + \mathcal{U}_{cov}^{(\infty)}\left[1 - \mathcal{H}\left(\frac{k_1^{l_\alpha}\, k_\alpha^{k_\alpha}}{k_2^{k_\alpha}\, l_\alpha^{l_\alpha}} - \varepsilon\right)\right] \end{cases} \tag{2.28}$$

where $\mathcal{H}(\cdot)$ is the Heaviside function, *i.e.* $\mathcal{H}(\xi) = 1$ if $\xi \geq 0$ and $\mathcal{H}(\xi) = 0$ if $\xi < 0$, and ε is a small value that takes into account the accuracy of the mathematical software package that is used to compute the Meijer-G function. In practice, ε is the smallest value after which computing the Meijer-G function introduces numerical problems. If the adopted algorithm is very efficient, then $\varepsilon = 0$. The main idea

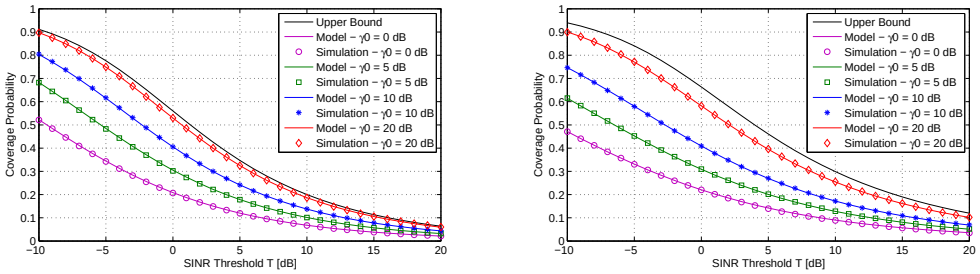

(a) $\alpha = 4$ (b) $\alpha = 5$

Figure 2.1: Coverage probability with density $\lambda_{BS} = 0.1$. Analytical model given by (2.28). Setup: i) $\lambda_{BS} = 0.1$; ii) $\alpha = 4, 5$; iii) $\rho_{BS} = 1$; and iv) $R_2 = 32$.

behind equation (2.28) is as follows. The exact formula (2.18) is used as long as the argument of the Meijer-G function is not smaller than ε. On the other hand, when this occurs the asymptotically-tight approximation in (2.27) is used, which has no numerical problems. This "adaptive" approach allows to keep the desired accuracy without increasing the computation time or incurring in numerical instabilities.

2.2.4 Numerical Results

In this section, some numerical results on the coverage probability are provided. In particular, in each figure the Upper Bound in (2.17), the coverage evaluated as in (2.28) and the simulation results are shown.

The simulated coverage probability is the result of Monte Carlo simulations. As far as Monte Carlo simulations are concerned, a real network with BSs randomly distributed in the 2D Euclidean plane according to a homogeneous PPP was simulated, with the intended MS being kept fixed at the origin of the plane. Among the set of BSs generated for each simulation instance, the intended BS was chosen as that closest to the intended MS, while all other BSs acted as interferers. This way, the random position of the serving BS is accurately taken into account.

It is worth mentioning that even though in the considered system model the interference is distributed in the whole 2D Euclidean plane, in practice only a finite area can be simulated, as stated in Section 1.3.5. Applying equation (1.39), the truncation radius, R_2, such that the infinite area is simulated with an accuracy equal to 10^{-3} was found to be 32 and 10 for $\alpha = 4, 5$ respectively. In Figures 2.1-2.3, which substantiate the proposed framework through an excellent agreement with the simulation results, the following general trends can be observed:

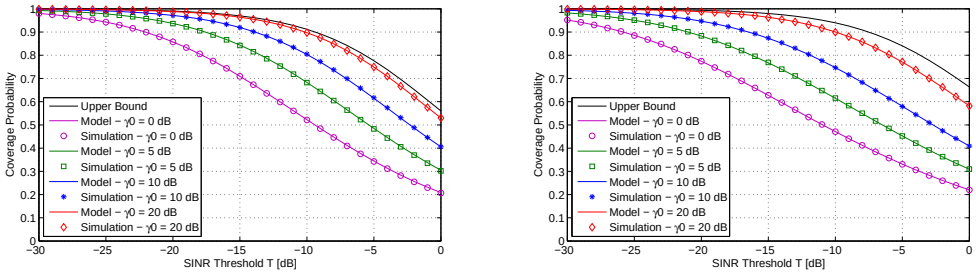

(a) $\alpha = 4$ (b) $\alpha = 5$

Figure 2.2: Coverage probability for low SINR and $\lambda_{BS} = 0.1$. Analytical model given by (2.28). Setup: i) $\lambda_{BS} = 0.1$; ii) $\alpha = 4, 5$; iii) $\rho_{BS} = 1$; and iv) $R_2 = 32$.

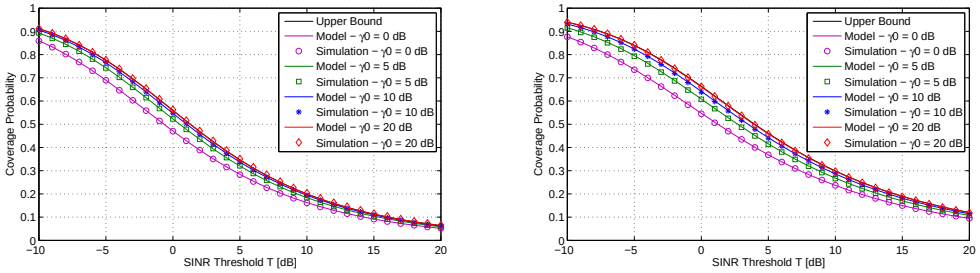

(a) $\alpha = 4$ (b) $\alpha = 5$

Figure 2.3: Coverage probability with density $\lambda_{BS} = 0.5$. Analytical model given by (2.28). Setup: i) $\lambda_{BS} = 0.5$; ii) $\alpha = 4, 5$; iii) $\rho_{BS} = 1$; and iv) $R_2 = 32$.

- the coverage probability tends to the Upper Bound given in equation (2.17) for $T \to \infty$, $T \to 0$ and $\gamma_0 \to \infty$ as stated in Section 2.2.2;

- for $\lambda_{BS} = 0.1$ the coverage probability increases for increasing values of the path-loss exponent α only when $\gamma_0 = 20$ dB, *i.e.* when the intended link experiences good propagation conditions. This is due to the low amount of interference, as the density is quite low. In this case the network is *noise-limited*, and thus, even if the interfering links experience the same path-loss, the advantage of a higher path-loss exponent in terms of reduced aggregate interference at the MS is outperformed by the disruptive effect on the intended link when $\gamma_0 < 20$ dB;

- for $\lambda = 0.5$ increasing α always improves the performance. In this case, the network is *interference-limited*, and thus increasing the path-loss exponent provides better performance not only for high SNR values.

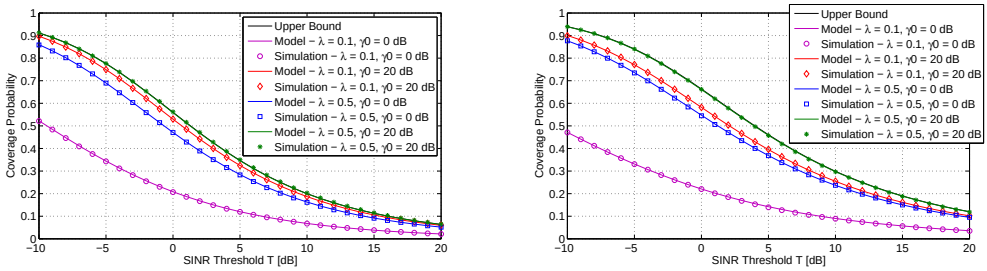

(a) $\alpha = 4$ (b) $\alpha = 5$

Figure 2.4: Coverage probability for varying densities. Analytical model given by (2.28). Setup: i) $\lambda_{BS} = 0.1, 0.5$; ii) $\alpha = 4, 5$; iii) $\rho_{BS} = 1$; and iv) $R_2 = 32$.

Figure 2.4 shows the coverage probability for different values of density λ_{BS}, and it can be noticed that the coverage probability is better for higher values of this parameter. This might not seem obvious, as increasing the density of the process increases the interference level. However, as the interfering nodes are transmitting low power levels ($P_I = 0$ dB), the interference received at the intended node is limited, due to the propagation model assumed in this study. Moreover, increasing the density also has the beneficial effect of reducing the distance between the intended BS, BS_0, and the intended node, implying a higher level of useful power at the victim node located at the origin. Thus, the latter effect overwhelms the previous one.

Chapter 3

Average Achievable Rate in Cellular Networks

In this chapter, the attention is turned on the mean data rate achievable in a cellular network. As for the coverage probability in Chapter 2, the work by Andrews et al. in [22] provides the starting point of a greatly simplified framework. In particular, the authors obtained a three-fold integral expression of the average rate by using the tools of stochastic geometry for network interference modeling. In the framework proposed in this thesis, starting from the same system model, a simple MGF-based approach allows to apply once again the closed-form expression of the Moment Generating Function of the aggregate interference power (Section 1.3). Then, by using the integration properties of the previously introduced Meijer-G function, a single-integral expression of the rate is obtained. Moreover, while the three-fold integral in [22] can be applied only to Rayleigh fading, the framework provided in this chapter is applicable to generalized fading distributions, and thanks to the MGF-based approach it will also be possible to consider different channel models for the intended and the interfering links [1, 2].

3.1 System Model

The reference system model is the same as that considered for the coverage probability in Section 2.1. In particular, the MSs and BSs of the 2D cellular network deployment are modeled as two independent homogeneous Poisson Point Processes with densities λ_{MS} and λ_{BS} respectively. Each MS communicates with its closest

BS, and all the other BSs act as interferers. The focus will be on the average achievable rate of an intended MS, which, thanks to Slivnyak's Theorem (Section A.3), can be assumed to be located at the origin of the 2D Euclidean plane without any loss of generality.

3.1.1 Channel Model

For the framework proposed in this chapter, the following assumptions are made. Please note that some of them are the same as for the coverage probability, and are listed below for the sake of completeness:

- an exponential-decaying path-loss model with $\alpha > 2$, common to all the links of the network, is considered [36];
- the constant transmit power of the intended and interfering BSs are denoted by P_0 and P_I respectively, and P_I is assumed to be the same for all the interfering BSs. Moreover, their ratio is denoted as $\rho_{BS} = P_I/P_0$;
- the complex channel gain of the intended link, h_0, is assumed to have a generic fading distribution. In particular, $f_{|\tilde{h}_0|^2}(\cdot)$ and $\mathcal{M}_{|\tilde{h}_0|^2}(\cdot)$ denote the pdf and the MGF of the square envelope of the normalized fading gains respectively, with $\tilde{h}_0 = h_0/\sqrt{\Omega_0} = h_0/\sqrt{R_0^{-\alpha}}$;
- the complex channel gain of the i-th interfering BS is denoted by h_i, for $i \in \Phi_{\text{BS}}^{\{\setminus \text{BS}_0\}}$, where $\Phi_{\text{BS}}^{\{\setminus \text{BS}_0\}}$ denotes the homogeneous PPP of all the BSs in the Euclidean plane except the BS of the intended link, BS_0. With $f_{|\tilde{h}_i|^2}(\cdot)$ and $\mathcal{M}_{|\tilde{h}_i|^2}(\cdot)$, the pdf and MGF of the square envelope of the normalized fading gains are respectively denoted;
- all the BSs deployed in the Euclidean plane are always transmitting, *i.e.* $p = 1$, and a constant envelope modulation is assumed, *i.e.* $b_j = 1, \forall j = 1, \ldots, M$;
- the noise at the intended MS is assumed to be AWGN with power σ_N^2, and the SNR is given by $\gamma_0 = P_0/\sigma_N^2$.

According to the above assumptions, the aggregate interference power is given by equation (1.1). In particular, it is the aggregate interference generated by all the interfering BSs belonging to the process $\Phi_{\text{BS}}^{\{\setminus \text{BS}_0\}}$, which fall outside a disk of radius

$r = R_0$, $b(0, R_0)$, with R_0 being the distance between the intended BS and MS:

$$\mathcal{I}_{r,\Phi} = \sum_{i \in \Phi_{\mathrm{BS}}^{\{\setminus \mathrm{BS}_0\}}} |h_i|^2 = \sum_{i \in \Phi_{\mathrm{BS}}^{\{\setminus \mathrm{BS}_0\}}} |\tilde{h}_i|^2 R_i^{-\alpha}$$

3.1.2 Problem Statement

In [22, Theorem 3] the authors provide a three-fold integral expression for the average achievable rate over a cell for the downlink case. In particular, they compute such mean rate in units of nats/Hz[1] for a typical user where adaptive code and modulation is used. The rate each user can achieve is thus given by the Shannon bound for its instantaneous SINR, *i.e.* $\ln(1 + \mathrm{SINR})$, and its average over $\Phi_{\mathrm{BS}}^{\{\setminus \mathrm{BS}_0\}}$ is given by:

$$\begin{aligned} \mathcal{R}(\lambda_{BS}, \alpha) &\triangleq \mathbb{E}_{\Phi_{\mathrm{BS}}^{\{\setminus \mathrm{BS}_0\}}} \{\ln(1 + \mathrm{SINR})\} \\ &= 2\pi\lambda_{BS} \int_0^\infty e^{-\pi\lambda_{BS} r^2} r \int_0^\infty e^{-r^\alpha (e^t - 1)/\gamma_0} \mathcal{M}_{\mathcal{I}_{r,\Phi}} \left(\rho_{BS} r^\alpha \left(e^t - 1\right)\right) \mathrm{d}t \mathrm{d}r \end{aligned} \tag{3.1}$$

where:

$$\mathcal{M}_{\mathcal{I}_{r,\Phi}} \left(\rho_{BS} r^\alpha \left(e^t - 1\right)\right) = \exp\left[-\pi\lambda_{BS} r^2 \left(\rho_{BS} \left(e^t - 1\right)\right)^{\frac{2}{\alpha}} \int_{(\rho_{BS}(e^t-1))^{-\frac{2}{\alpha}}}^\infty \frac{1}{1 + x^{\alpha/2}} \mathrm{d}x \right]$$

and the expectation over $\Phi_{\mathrm{BS}}^{\{\setminus \mathrm{BS}_0\}}$ implies the computation of the average over both $|\tilde{h}_i|^2$ and R_i, for $i \in \Phi_{\mathrm{BS}}^{\{\setminus \mathrm{BS}_0\}}$.

3.2 Single-integral Expression over Nakagami-m Fading Channels

In this section, both intended and interfering links will be modeled as Nakagami-m fading channels. The proposed framework allows to easily consider the combination of different channel models, as shown in Section 3.2.4. As provided in the proof of [22, Theorem 3], in order to obtain the integral form (3.1) of the mean rate, the average over the Poisson Point Process $\Phi_{\mathrm{BS}}^{\{\setminus \mathrm{BS}_0\}}$ is evaluated as for the coverage probability (see Section 2.1.2): the instantaneous rate is first conditioned to a specific

[1] 1 bit= $\log_2(e) = 0.693$ nats.

value of r, and then integrated over the distribution of the distance between the intended BS and MS, $f_{R_0}(r)$, which is given by equation (2.4):

$$\begin{aligned}\mathcal{R}(\lambda_{BS},\alpha) &= \int_0^\infty f_{R_0}(r)\mathcal{R}(r)\mathrm{d}r \\ &= \int_0^\infty f_{R_0}(r)\mathbb{E}_{\Phi_{\mathrm{BS}}^{\{\setminus \mathrm{BS}_0\}}}\left\{\ln\left(1+\frac{P_0|\tilde{h}_0|^2 r^{-\alpha}}{\sigma_N^2+P_I\mathcal{I}_{r,\Phi}}\right)\right\}\mathrm{d}r \\ &= 2\pi\lambda_{BS}\int_0^\infty e^{-\pi\lambda_{BS}r^2} r\mathbb{E}_{\Phi_{\mathrm{BS}}^{\{\setminus \mathrm{BS}_0\}}}\left\{\ln\left(1+\frac{P_0|\tilde{h}_0|^2 r^{-\alpha}}{\sigma_N^2+P_I\mathcal{I}_{r,\Phi}}\right)\right\}\mathrm{d}r\end{aligned} \tag{3.2}$$

In the proposed framework, in order to compute $\mathcal{R}(\lambda_{BS},\alpha)$, the first step is to re-write (3.2) in a more convenient form, that is useful to remove the conditioning over fading statistics and random distances. To this aim, the MGF-based approach provided in [43, 44, 48, 49] is exploited to compute the average rate. In particular, the framework recently introduced in [49] for interference channels seems to be well-suited to solve the problem at hand. In [49, Lemma 1], the average per-link throughput is written as:

$$\mathcal{R}=\mathbb{E}\left\{\ln\left(1+\frac{\sum_{n=1}^{N}x_n}{1+\sum_{m=1}^{M}y_m}\right)\right\}=\int_0^\infty\frac{\mathcal{M}_y(z)-\mathcal{M}_{x,y}(z)}{z}e^{-z}\mathrm{d}z$$

where x_n, y_m are two arbitrary non-negative random variables, and in case they are also independent, $\mathcal{M}_{x,y}(z)=\mathcal{M}_x(z)\mathcal{M}_y(z)$. Considering equation (3.2), and normalizing both numerator and denominator of the SINR by the noise power σ_N^2, the following form of the average rate can be found after some algebraic manipulation:

$$\begin{aligned}\mathcal{R}(\lambda_{BS},\alpha) &= \int_0^\infty f_{R_0}(r)\mathcal{R}(r)\mathrm{d}r \\ &= \int_0^\infty f_{R_0}(r)\int_0^\infty\left\{\mathcal{M}_{\mathcal{I}_{r,\Phi}}\left(\frac{P_I}{\sigma_N^2}z\right)\left[1-\mathcal{M}_{|\tilde{h}_0|^2}\left(\frac{P_0 r^{-\alpha}}{\sigma_N^2}z\right)\right]\right\}\frac{e^{-z}}{z}\mathrm{d}z\mathrm{d}r\end{aligned} \tag{3.3}$$

where $\mathcal{M}_{|\tilde{h}_0|^2}(\cdot)$ is the MGF of $|\tilde{h}_0|^2$, and is known in closed-form for many fading distributions [36]. By observing the above form of the average rate, it can be noticed that the proposed MGF-based approach allows to easily consider different

channel models for the intended and the interfering links by simply appliying the corresponding MGF. As previously stated, the intended link is assumed to experience Nakagami-m fading as the interfering links, while other channel models will be considered in Section 3.2.4. The MGF of $|\tilde{h}_0|^2$ for Nakagami-m fading is given by [36, Eq.(2.22)]:

$$\mathcal{M}_{|\tilde{h}_0|^2}(s) = \left(1 + \frac{s}{m_0}\right)^{-m_0} \tag{3.4}$$

Referring to equation (3.3), some important comments are worth being made. First of all, it can be noticed that, by exploiting the MGF-based approach, the average rate is now given by a two-fold integral that only requires the MGF of the intended link, which is known in closed-form for arbitrary fading channels, and the MGF of the aggregate interference. This MGF was evaluated in Chapter 1 in closed-form for Nakagami-m, Rayleigh and non fading channels. In particular, as for the coverage probability, given the system model being considered, the MGF in the exclusion region scenario will be used (equation (1.33)). Second, by using the MGF-based approach, some analytical issues are avoided, which make the original derivation in [22] useful only for Rayleigh fading on the intended link. As a matter of facts, the fourth equality in [22, Appendix B] holds only for exponential random variables, while its generalization to different random variables would lead to a much more complicated analytical development.

Plugging (3.4) and the closed-form expression of the MGF over Nakagami-m fading channels, provided in equation (1.33), into (3.3):

$$\begin{aligned}
\mathcal{R}(\lambda_{BS},\alpha) = 2\pi\lambda_{BS} \int_0^\infty r \int_0^\infty \frac{e^{-z}}{z} \Bigg\{ \left[1 - \frac{1}{\left(1+\frac{zP_0 r^{-\alpha}}{m_0\sigma_N^2}\right)^{m_0}}\right] \exp\left[-\frac{\pi\lambda_{BS} r^2}{\left(1+\frac{zP_I r^{-\alpha}}{m_0\sigma_N^2}\right)^{m_0}}\right] \\
\times \exp\left[-\frac{\pi\lambda_{BS} z P_I r^{(2-\alpha)} m_0^{(m_0+1)}}{\sigma_N^2\left(1-\frac{2}{\alpha}\right)} \frac{{}_2F_1\left(m_0+1;1;2-\frac{2}{\alpha};\frac{\frac{zP_I}{\sigma_N^2}}{\frac{zP_I}{\sigma_N^2}+m_0 r^\alpha}\right)}{\left(m_0+\frac{zP_I}{\sigma_N^2} r^{-\alpha}\right)^{(m_0+1)}}\right] \Bigg\} \mathrm{d}z\mathrm{d}r \\
\overset{(a)}{=} \pi\lambda_{BS} \int_0^\infty \frac{1}{y} \left[1 - \frac{1}{\left(1+\frac{y}{m_0}\gamma_0\right)^{m_0}}\right] \Bigg\{ \int_0^\infty \exp\left[-yx^{\frac{\alpha}{2}}\right] \exp\left[-\frac{x\pi\lambda_{BS}}{(1+y\gamma_I)^{m_0}}\right] \\
\times \exp\left[-xy\pi\lambda_{BS}\gamma_I \frac{{}_2F_1\left(m_0+1;1;2-\frac{2}{\alpha};\frac{y\gamma_I}{y\gamma_I+m_0}\right)}{\left(1-\frac{2}{\alpha}\right)(1+y\gamma_I)^{(m_0+1)}}\right] \mathrm{d}x \Bigg\} \mathrm{d}y
\end{aligned}$$

where (a) follows from two exchange of variables, $zr^{-\alpha} = y$ and $r^2 = x$, and $\gamma_I = \frac{P_I}{\sigma_N^2}$. The average rate can thus be written as:

$$\mathcal{R}(\lambda_{BS}, \alpha) = \pi\lambda_{BS} \int_0^\infty \mathcal{F}_1(y) \left\{ \underbrace{\int_0^\infty \exp\left[-\mathcal{F}_2(y)x\right] \exp\left[-yx^{\alpha/2}\right] \mathrm{d}x}_{\mathcal{I}_{\mathcal{F}}(y)} \right\} \mathrm{d}y \tag{3.5}$$

where:

$$\begin{aligned} \mathcal{F}_1(y) &= \frac{1}{y}\left[1 - \left(1 + \frac{y}{m_0}\gamma_0\right)^{-m_0}\right] \\ \mathcal{F}_2(y) &= \frac{\pi\lambda_{BS}}{\left(1 + \frac{y\gamma_I}{m_0}\right)^{m_0}} + \pi\lambda_{BS} y\gamma_I {m_0}^{(m_0+1)} \frac{{}_2F_1\left(m_0+1; 1; 2-\frac{2}{\alpha}; \frac{y\gamma_I}{y\gamma_I+m_0}\right)}{\left(1-\frac{2}{\alpha}\right)\left(m_0 + y\gamma_I\right)^{(m_0+1)}} \end{aligned} \tag{3.6}$$

It can be noticed that $\mathcal{F}_1(y)$ is only related to the MGF of the fading model for the intended link (the term $1/y$ is due to the change of variables), while $\mathcal{F}_2(y)$ results from the product of the MGF of the fading model for the interfering links with the term $\exp\left(-\pi\lambda_{BS}r^2\right)$, given by the pdf $f_{R_0}(r)$.

3.2.1 Meijer-G function

The inner integral $\mathcal{I}_{\mathcal{F}}(y)$ in equation (3.5) can be computed in closed-form with the help of the Meijer-G function introduced in Section 2.2.1 as follows:

$$\begin{aligned} \mathcal{I}_{\mathcal{F}}(y) &\overset{(a)}{=} \frac{1}{\mathcal{F}_2(y)} - \frac{\alpha y}{2\mathcal{F}_2(y)} \int_0^\infty x^{\left(\frac{\alpha}{2}-1\right)} \exp\left[-\mathcal{F}_2(y)x\right] \exp\left[-yx^{\frac{\alpha}{2}}\right] \mathrm{d}x \\ &\overset{(b)}{=} \frac{1}{\mathcal{F}_2(y)} - \frac{\alpha y}{2\mathcal{F}_2(y)} \int_0^\infty x^{\left(\frac{\alpha}{2}-1\right)} G_{0,1}^{1,0}\left(\mathcal{F}_2(y)\middle|\begin{matrix}-\\0\end{matrix}\right) G_{0,1}^{1,0}\left(yx^{\frac{\alpha}{2}}\middle|\begin{matrix}-\\0\end{matrix}\right) \mathrm{d}x \\ &\overset{(c)}{=} \frac{1}{\mathcal{F}_2(y)} - \frac{\alpha y \sqrt{k_\alpha l_\alpha^{(\alpha-1)}}}{2(2\pi)^{\left(\frac{l_\alpha+k_\alpha}{2}-1\right)}\left[\mathcal{F}_2(y)\right]^{\left(\frac{\alpha}{2}+1\right)}} \underbrace{G_{l_\alpha,k_\alpha}^{k_\alpha,l_\alpha}\left(\frac{y^{k_\alpha} l_\alpha^{l_\alpha}}{\mathcal{F}_2^{l_\alpha}(y) k_\alpha^{k_\alpha}}\middle|\begin{matrix}\mathbf{v}\\\mathbf{w}\end{matrix}\right)}_{\mathcal{U}_{rate}(y)} \end{aligned} \tag{3.7}$$

where (a) is obtained by using integration by parts, (b) is obtained by using [42, Eq.(8.4.3.1)] for both integrand functions in $\mathcal{I}_{\mathcal{F}}(y)$, (c) follows from the general integral [42, Eq.(2.24.1.1)] which exploits the properties of the Meijer-G function,

$\mathbf{v} = \frac{1-\frac{\alpha}{2}}{l_\alpha}, \frac{2-\frac{\alpha}{2}}{l_\alpha}, \ldots, \frac{l_\alpha-\frac{\alpha}{2}}{l_\alpha}$ and $\mathbf{w} = 0, \frac{1}{k_\alpha}, \ldots, \frac{k_\alpha-1}{k_\alpha}$.
Finally, substituting (3.7) in (3.5), the following single-integral expression of the average rate can be obtained:

$$\mathcal{R}(\lambda_{BS}, \alpha) = \pi\lambda_{BS} \int_0^\infty \left[\frac{\mathcal{F}_1(y)}{\mathcal{F}_2(y)} - \frac{\alpha y \sqrt{k_\alpha l_\alpha^{(\alpha-1)}} \mathcal{F}_1(y)}{2(2\pi)^{\left(\frac{l_\alpha+k_\alpha}{2}-1\right)} [\mathcal{F}_2(y)]^{\left(\frac{\alpha}{2}+1\right)}} \mathcal{U}_{rate}(y) \right] \mathrm{d}y \quad (3.8)$$

with:

$$\mathcal{U}_{rate}(y) = G_{l_\alpha,k_\alpha}^{k_\alpha,l_\alpha} \left(\frac{y^{k_\alpha} l_\alpha^{l_\alpha}}{\mathcal{F}_2^{l_\alpha}(y) k_\alpha^{k_\alpha}} \middle| \begin{matrix} \mathbf{v} \\ \mathbf{w} \end{matrix} \right) \quad (3.9)$$

The integral in equation (3.8) can be solved by using conventional quadrature rule methods [38, Chapter 25], *e.g.* the Gauss-Chebyshev Quadrature (GCQ) integration rule [44, Eq.(9)]:

$$\begin{aligned} \int_0^\infty f(x)\mathrm{d}x &= \sum_{n=1}^{N} w_n s(s_n) \\ w_n &= \frac{\pi^2 \sin\left(\frac{2n-1}{2N}\pi\right)}{4N \cos^2\left[\frac{\pi}{4}\cos\left(\frac{2n-1}{2N}\pi\right)+\frac{\pi}{4}\right]} \\ s_n &= \tan\left[\frac{\pi}{4}\cos\left(\frac{2n-1}{2N}\pi\right)+\frac{\pi}{4}\right] \end{aligned} \quad (3.10)$$

It is worthwhile emphasizing that the result in (3.8) is exact according to the assumption that the positions of the BSs can be modeled as a homogeneous Poisson Point Process, as substantiated in [22]. Furthermore, unlike [22, Eq.(25)], the proposed framework is valid for the more general Nakagami-m fading and allows to avoid a three-fold numerical integration thanks to the closed-form MGF in (1.33) and to the flexibility of the Meijer-G function.

3.2.2 Upper Bound

The first term in equation (3.8) is actually an Upper Bound of the average achievable rate, as the second integrand function is positive and integrated over a positive interval. By explicitly writing $\mathcal{F}_1(y)$ and $\mathcal{F}_1(y)$, the Upper Bound is thus given by:

$$\mathcal{R}^{(UB)}(\alpha, m_0) = \pi\lambda_{BS} \int_0^\infty \frac{\frac{1}{y}\left[1-\left(1+\frac{y}{m_0}\gamma_0\right)^{-m_0}\right]}{\frac{\pi\lambda_{BS}}{\left(1+\frac{y\gamma_I}{m_0}\right)^{m_0}} + \pi\lambda_{BS} y\gamma_I {m_0}^{(m_0+1)} \frac{{}_2F_1\left(m_0+1;1;2-\frac{2}{\alpha};\frac{y\gamma_I}{y\gamma_I+m_0}\right)}{\left(1-\frac{2}{\alpha}\right)(m_0+y\gamma_I)^{(m_0+1)}}} \mathrm{d}y \quad (3.11)$$

It can be noticed that the Upper Bound depends only on the PPP density λ_{BS} and on the parameter of the Nakagami-m fading m_0, as well as on the transmitting and noise power levels, which appear in γ_0, γ_I, when the intended and the interfering BSs do not transmit the same power. In this case, $\rho_{BS} = 1$ leads to $\gamma_0 = \gamma_I$, which makes the above Upper Bound depend only on λ_{BS} and m_0. Furthermore, the Upper Bound is given by a very simple single-integral expression which does not require either the Meijer-G function or its asymptotic approximation.

3.2.3 Series Expansion of the Meijer-G function

As for the coverage probability (Section 2.2.3), the computation of integral (3.8) generates some numerical instabilities when the argument of the Meijer-G function takes very small values. Hopefully, the same procedure as that used for the coverage probability can be applied for the average rate as well. Inverting the Meijer-G function according to [42, Eq.(8.2.2.14)], the integral $\mathcal{I}_{\mathcal{F}}(y)$ can be written as follows:

$$\mathcal{I}_{\mathcal{F}}(y) = \frac{1}{\mathcal{F}_2(y)} - \frac{\alpha y \sqrt{k_\alpha l_\alpha^{(\alpha-1)}}}{2(2\pi)^{\left(\frac{l_\alpha+k_\alpha}{2}-1\right)}[\mathcal{F}_2(y)]^{\left(\frac{\alpha}{2}+1\right)}} \underbrace{G_{k_\alpha,l_\alpha}^{l_\alpha,k_\alpha}\left(\frac{\mathcal{F}_2^{l_\alpha}(y)k_\alpha^{k_\alpha}}{y^{k_\alpha}l_\alpha^{l_\alpha}}\middle|\begin{matrix}\mathbf{x}\\ \mathbf{z}\end{matrix}\right)}_{\mathcal{V}_{rate}(y)}$$

where $\mathbf{x} = \left[1, \frac{k_\alpha-1}{k_\alpha}, \ldots, \frac{1}{k_\alpha}\right]$ and $\mathbf{z} = \left[\frac{l_\alpha-1+\frac{\alpha}{2}}{l_\alpha}, \frac{l_\alpha-2+\frac{\alpha}{2}}{l_\alpha}, \ldots, \frac{\frac{\alpha}{2}}{l_\alpha}\right]$. Applying the series expansion of the Meijer-G function in [47, Theorem 1.8.3] to $\mathcal{V}_{rate}(y)$:

$$\mathcal{I}_{\mathcal{F}}(y) = \frac{1}{\mathcal{F}_2(y)} - \frac{\alpha y \sqrt{k_\alpha l_\alpha^{(\alpha-1)}}}{2(2\pi)^{\left(\frac{l_\alpha+k_\alpha}{2}-1\right)}[\mathcal{F}_2(y)]^{\left(\frac{\alpha}{2}+1\right)}} \mathcal{V}_{rate}^{(\infty)}(y)$$

with $\mathcal{V}_{rate}^{(\infty)}(y) = \sum_{t=1}^{k_\alpha} \mathcal{V}_{rate}^{(\infty)}(y;t)$, where:

$$\mathcal{V}_{rate}^{(\infty)}(y;t) = (-1)^{(k_\alpha-1)} \times e^{-j\pi\mathbf{x}(t)(1-k_\alpha)} \times \left(\frac{\mathcal{F}_2^{l_\alpha}(y)k_\alpha^{k_\alpha}}{y^{k_\alpha}l_\alpha^{l_\alpha}} e^{j\pi(1-k_\alpha)}\right)^{(\mathbf{x}(t)-1)}$$
$$\times \left[\prod_{\substack{q=1\\q\neq t}}^{k_\alpha} \Gamma\left(\mathbf{x}(t)-\mathbf{x}(q)\right)\Gamma\left(1+\mathbf{x}(q)-\mathbf{x}(t)\right)\right] \times \left[\frac{\prod_{q=1}^{l_\alpha}\Gamma\left(1+\mathbf{z}(q)-\mathbf{x}(t)\right)}{\prod_{\substack{q=1\\q\neq t}}^{k_\alpha}\Gamma\left(1+\mathbf{x}(q)-\mathbf{x}(t)\right)}\right] \tag{3.12}$$

Finally, the single-integral form of the average rate which solves the numerical instabilities is:

$$\begin{cases} \mathcal{R}^{(\mathcal{H})}(\lambda_{BS},\alpha) = \pi\lambda_{BS}\int\limits_0^\infty \left[\frac{\mathcal{F}_1(y)}{\mathcal{F}_2(y)} - \frac{\mathcal{F}_1(y)\alpha y\sqrt{k_\alpha l_\alpha^{(\alpha-1)}}}{2(2\pi)^{\left(\frac{l_\alpha+k_\alpha}{2}-1\right)}[\mathcal{F}_2(y)]^{\left(\frac{\alpha}{2}+1\right)}}\mathcal{V}_{rate}^{(\mathcal{H})}(y)\right]\mathrm{d}y \\ \\ \mathcal{V}_{rate}^{(\mathcal{H})}(y) = \mathcal{V}_{rate}(y)\mathcal{H}\left(\frac{\mathcal{F}_2^{l_\alpha}(y)k_\alpha^{k_\alpha}}{y^{k_\alpha}l_\alpha^{l_\alpha}}-\varepsilon\right) + \mathcal{V}_{rate}^{(\infty)}(y)\left[1-\mathcal{H}\left(\frac{\mathcal{F}_2^{l_\alpha}(y)k_\alpha^{k_\alpha}}{y^{k_\alpha}l_\alpha^{l_\alpha}}-\varepsilon\right)\right] \end{cases} \tag{3.13}$$

where $\mathcal{H}(\cdot)$ is the Heaviside function and ε is the smallest argument of the Meijer-G function after which computing the Meijer-G function introduces numerical instabilities, due to the algorithm implemented by the mathematical software package being used.

3.2.4 Combination of Different Channel Models

As stated at the end of Section 3.2, the two functions $\mathcal{F}_1(y)$ and $\mathcal{F}_2(y)$ are independent, as originated from the fading model on the intended and on the interfering links respectively. This is a great advantage of the proposed framework, as it allows to combine different channel models for the intended and interfering links. For instance, considering that the intended link is the one between the intended MS and its closest BS, it might be useful to model this channel with a less severe fading (*e.g.* a Nakagami-m fading with $m_0 = 2$), while the interfering links experience deeper fading fluctuations (*e.g.* Rayleigh fading).

The combination of different fading models is straightforward, as the procedure which led to equation (3.13) is valid for generic $\mathcal{F}_1(y)$ and $\mathcal{F}_2(y)$. Thus, it is sufficient to obtain the MGF of $\left|\tilde{h}_0\right|^2$ and $\left|\tilde{h}_i\right|^2$ for the desired fading model. In the following, these MGFs will be provided for Rayleigh fading (which is a particular case of the Nakagami-m fading previously considered) and Lognormal fading on the intended link. Firstly, it is worthwhile noting that in (3.13) the intended and interfering channel can be modeled with different values of m_0, *i.e.*:

$$\begin{aligned} \mathcal{F}_{1,Nak}(y) &= \frac{1}{y}\left[1-\left(1+\frac{y}{m_0}\gamma_0\right)^{-m_0}\right] \\ \mathcal{F}_{2,Nak}(y) &= \frac{\pi\lambda_{BS}}{\left(1+\frac{y\gamma_I}{m_I}\right)^{m_I}} + \pi\lambda_{BS}y\gamma_I{m_I}^{(m_I+1)}\frac{{}_2F_1\left(m_I+1;1;2-\frac{2}{\alpha};\frac{y\gamma_I}{y\gamma_I+m_I}\right)}{\left(1-\frac{2}{\alpha}\right)\left(m_I+y\gamma_I\right)^{(m_I+1)}} \end{aligned} \tag{3.14}$$

where m_0 and m_I are the parameters of the Nakagami-m fading on the intended and interfering links respectively.

3.2.4.1 MGF of $|\tilde{h}_0|^2$

Rayleigh fading. The Moment Generating Function of $|\tilde{h}_0|^2$ in case of Rayleigh fading is given by [36, Eq.(2.8)], and it can also be obtained from (3.4) setting $m_0 = 1$. Evaluating this MGF in $s = \frac{P_0 r^{-\alpha}}{\sigma_N^2} z$ yields to:

$$\mathcal{M}_{|\tilde{h}_0|^2}\left(\frac{P_0 r^{-\alpha}}{\sigma_N^2} z\right) = \left(1 + \frac{P_0 r^{-\alpha}}{\sigma_N^2} z\right)^{-1} \tag{3.15}$$

and thus $\mathcal{F}_1(y)$ is given by:

$$\mathcal{F}_{1,Ray}(y) = \frac{1}{y}\left[1 - (1 + y\gamma_0)^{-1}\right] \tag{3.16}$$

Lognormal fading. In this case, the MGF is given in [36, Eq.(2.54)] in the following approximated form:

$$\mathcal{M}_{|\tilde{h}_0|^2}\left(\frac{P_0 r^{-\alpha}}{\sigma_N^2} z\right) \simeq \frac{1}{\sqrt{\pi}} \sum_{n=1}^{N_p} H_{x_n} \exp\left[-10^{\left(\frac{\sqrt{2}\sigma_{log} x_n + \mu_{\text{dB}}}{10}\right)} \frac{P_0 r^{-\alpha}}{\sigma_N^2} z\right] \tag{3.17}$$

where x_n are the zeros of the N_p-order Hermite plynomial, H_{x_n} are the weight factors, and μ_{dB} and σ_{log} are the mean and the standard deviation of $10\log_{10}\left(|\tilde{h}_0|^2\right)$ in dB, respectively. Considering that $\mathbb{E}_{|\tilde{h}_0|^2}\left\{|\tilde{h}_0|^2\right\} = 1$ implies $\mu_{\text{dB}} = 0$ dB, and $\mathcal{F}_1(y)$ can be written as:

$$\mathcal{F}_{1,Log}(y) = \mathcal{F}^{(1)}_{1,Log}(y) - \mathcal{F}^{(2)}_{1,Log}(y) = \frac{1}{y} - \frac{1}{y\sqrt{\pi}} \sum_{n=1}^{N_p} H_{x_n} \exp\left[-10^{\left(\frac{\sqrt{2}\sigma_{log} x_n}{10}\right)} \gamma_0 y\right] \tag{3.18}$$

In the above formula, $\mathcal{F}_1(y)$ was split into two terms because this allows to write the average rate as the sum of two contributions as follows:

$$\begin{cases} \mathcal{R}^{(\mathcal{H})}(\lambda_{BS}, \alpha) = \mathcal{R}^{(\mathcal{H})}_1(\lambda_{BS}, \alpha) - \mathcal{R}^{(\mathcal{H})}_2(\lambda_{BS}, \alpha) \\ \mathcal{R}^{(\mathcal{H})}_i(\lambda_{BS}, \alpha) = \pi\lambda_{BS} \int_0^\infty \left[\frac{\mathcal{F}^{(i)}_{1,Log}(y)}{\mathcal{F}_2(y)} - \frac{\mathcal{F}^{(i)}_{1,Log}(y)\alpha y \sqrt{k_\alpha l_\alpha^{(\alpha-1)}}}{2(2\pi)^{\left(\frac{l_\alpha + k_\alpha}{2} - 1\right)} [\mathcal{F}_2(y)]^{\left(\frac{\alpha}{2}+1\right)}} \mathcal{V}^{(\mathcal{H})}_{rate}(y)\right] \mathrm{d}y \\ \mathcal{V}^{(\mathcal{H})}_{rate}(y) = \mathcal{V}_{rate}(y)\mathcal{H}\left(\frac{\mathcal{F}_2^{l_\alpha}(y) k_\alpha^{k_\alpha}}{y^{k_\alpha} l_\alpha^{l_\alpha}} - \varepsilon\right) + \mathcal{V}^{(\infty)}_{rate}(y)\left[1 - \mathcal{H}\left(\frac{\mathcal{F}_2^{l_\alpha}(y) k_\alpha^{k_\alpha}}{y^{k_\alpha} l_\alpha^{l_\alpha}} - \varepsilon\right)\right] \end{cases} \tag{3.19}$$

where from (3.18):

$$\begin{aligned} \mathcal{F}^{(1)}_{1,Log}(y) &= \frac{1}{y} \\ \mathcal{F}^{(2)}_{1,Log}(y) &= \frac{1}{y\sqrt{\pi}} \sum_{n=1}^{N_p} H_{x_n} \exp\left[-10^{\left(\frac{\sqrt{2}\sigma_{log}x_n}{10}\right)}\gamma_0 y\right] \end{aligned} \tag{3.20}$$

3.2.4.2 MGF of $|\tilde{h}_i|^2$

Rayleigh fading. For the function $\mathcal{F}_2(y)$, the Moment Generating Function of $|\tilde{h}_i|^2$ over Rayleigh fading channels has to be multiplied by the factor $\exp\left(-\pi\lambda_{BS}r^2\right)$, as previously stated. Otherwise, by simply setting $m_I = 1$ in the second equation of (3.14):

$$\mathcal{F}_2(y) = \frac{\pi\lambda_{BS}}{1+\gamma_I y} + \pi\lambda_{BS} y\gamma_I \frac{{}_2F_1\left(2;1;2-\frac{2}{\alpha};\frac{y\gamma_I}{y\gamma_I+1}\right)}{\left(1-\frac{2}{\alpha}\right)\left(1+y\gamma_I\right)^2} \tag{3.21}$$

3.3 Numerical Results

In this section, the proposed analytical framework is compared with Monte Carlo simulations. The real network was simulated as for the coverage probability. The intended MS was kept fixed at the origin of the 2D Euclidean plane, and among the set of BSs generated at each simulation instance, the intended one was chosen as that closest to the intended MS, while all the others act as interferers. Given the intended and the interfering links, for each simulation instance, the empirical rate was computed as:

$$\mathcal{R}_{MC} = \ln\left[1 + \left(\frac{P_0|\tilde{h}_0|^2 r^{-\alpha}}{\sigma_N^2 + P_I\mathcal{I}_{r,\Phi}}\right)\right] \tag{3.22}$$

The average rate was obtained by averaging over a large number of simulation instances, in which fading and positions of both intended and interfering BSs took different values, according to generalized fading and conditional uniform distributions respectively. In this case, following the approach proposed in [32], the truncation radius was set to 50 for $\alpha = 4, 5$.

In Figures 3.1-3.3, some numerical examples for various fading conditions and density of the BSs are shown. In particular, the intended link is modeled as a Nakagami-m fading channel, and the interfering links as Rayleigh fading channels. The following general trends can be observed:

- the average rate increases with the SNR γ_0, and with the density λ_{BS}. These behavours are in agreement with [22];

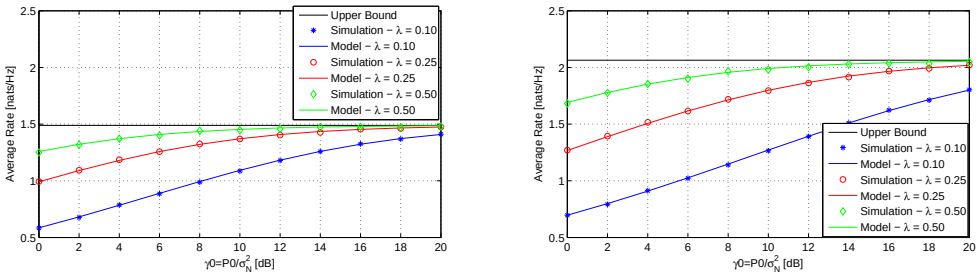

(a) $\alpha = 4$ (b) $\alpha = 5$

Figure 3.1: Average rate $\mathcal{R}$ in nats/Hz with Nakagami-m fading on the intended link and Rayleigh fading on the interfering links. Analytical model in (3.13). Setup: i) $m_0 = 1$; ii) $\rho_{BS} = 1$; and iii) $R_2 = 50$.

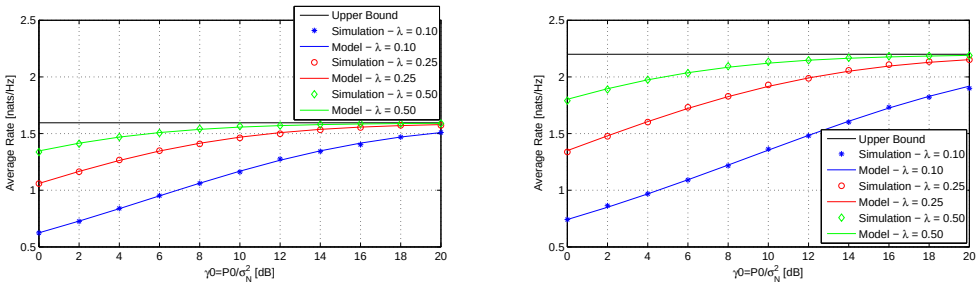

(a) $\alpha = 4$ (b) $\alpha = 5$

Figure 3.2: Average rate $\mathcal{R}$ in nats/Hz with Nakagami-m fading on the intended link and Rayleigh fading on the interfering links. Analytical model in (3.13). Setup: i) $m_0 = 2$; ii) $\rho_{BS} = 1$; and iii) $R_2 = 50$.

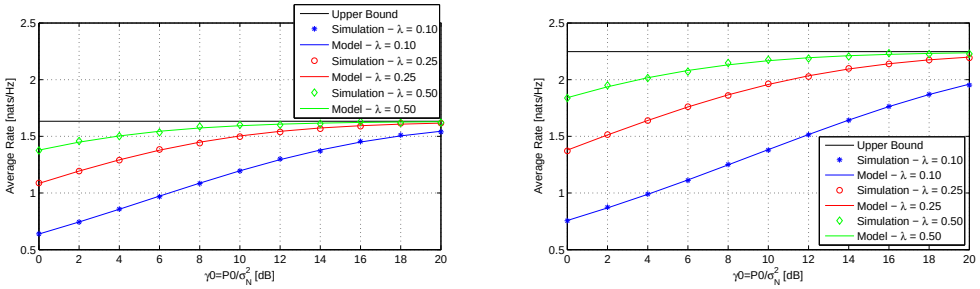

(a) $\alpha = 4$ (b) $\alpha = 5$

Figure 3.3: Average rate $\mathcal{R}$ in nats/Hz with Nakagami-m fading on the intended link and Rayleigh fading on the interfering links. Analytical model in (3.13). Setup: i) $m_0 = 3$; ii) $\rho_{BS} = 1$; and iii) $R_2 = 50$.

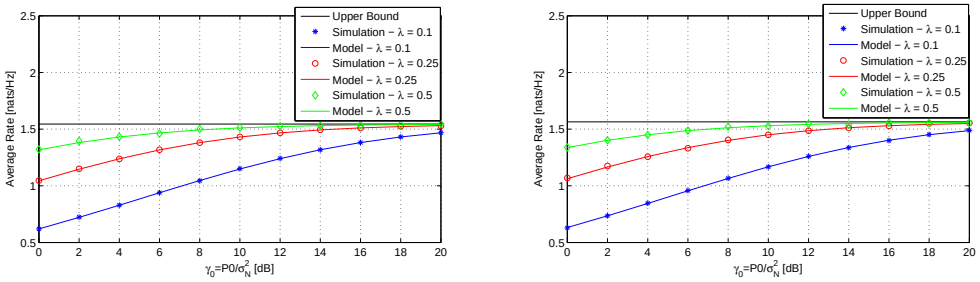

(a) $m_0 = 2$ (b) $m_0 = 3$

Figure 3.4: Average rate $\mathcal{R}$ in nats/Hz over Nakagami-m fading channels. Analytical model in (3.13). Setup: i) $\alpha = 4$; ii) $\rho_{BS} = 1$; and iii) $R_2 = 50$.

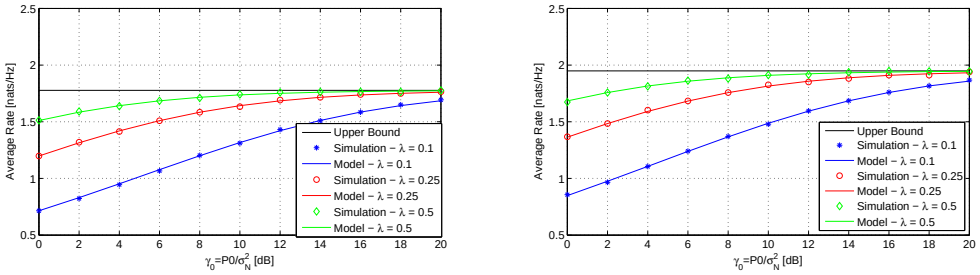

(a) $\sigma_{log} = 4$ dB (b) $\sigma_{log} = 8$ dB

Figure 3.5: Average rate $\mathcal{R}$ in nats/Hz with Lognormal fading on the intended link and Rayleigh fading on the interfering links. Analytical model in (3.13), (3.20). Setup: i) $\alpha = 4$; ii) $\rho_{BS} = 1$; and iii) $R_2 = 50$.

- the average rate significantly increases for higher values of the path-loss exponent α, while it slightly improves for less severe fading conditions on the intended link, *i.e.* for increasing values of m_0. It can be noticed that, even though a large value of α results in a reduction of the received power on the intended link, this also results in reduced interference. The latter effect is thus the dominant one. If m_0 increases, on the other hand, the fading fluctuations are less pronounced on the intended link, while the fading fluctuations on the interfering links are the same as Rayleigh fading is assumed in this case;

- in Figure 3.1, for Rayleigh fading (as $m_0 = 1$) and $\alpha = 4$ the average rate reaches the Upper Bound $\mathcal{R} \to 1.49$ nats/Hz for $\gamma_0 \to \infty$, as predicted in [22, Eq.(30)]. This asymptotic limit increases with m_0 and α, as stated in Section 3.2.2.

In Figure 3.4, the average rate with Nakagami-m fading on both the intended and interfering links is provided for $\alpha = 4$. In this case, higher values of the Nakagami-m parameter, m_0, still provide better performance as for the previous case of Rayleigh fading on the interfering links, but this gain is now less evident. By comparing Figures 3.4(a) and 3.4(b) with 3.2(a) and 3.3(a) respectively, when all the links experience Nakagami-m fading, for higher values of m_0 the fading fluctuations are less pronounced on the interfering links as well, and thus the gain for the intended user is limited. As a result, the average rate slightly improves with reference to the case of Rayleigh fading on the intended link (see Figure 3.1(a)), and definetly decreases when compared to the Nakagami-m fading cases.

In Figure 3.5, the average rate with Lognormal fading over the intended link is shown. It can be noticed that the rate increases for higher values of the standard deviation of $10\log_{10}\left(|\tilde{h}_0|^2\right)$, σ_{log}. This behaviour might not seem obvious, and it can be explained as follows: the effect on the useful signal of a certain level of interference basically depends on the mean interference level, with respect to the mean level of the intended signal. In particular, when these average values are similar, the effect of a greater variance of the received signal level on the intended user is almost unchanged: both the events that the received SINR is below or over a specific threshold have similar probabilities. Observing Figure 3.5, it can be deduced that the mean interference level is higher than the mean useful signal level, and thus increasing its range consequently increases the number of events for which the SINR is above the threshold level T. Thus, in such cases, the performance increases for increasing values of the standard deviation of the Lognormal fading.

Chapter 4

Average Symbol Error Probability

In this chapter, a novel framework for the computation of the Average Symbol Error Probability (ASEP) of an intended wireless communication system in the presence of network interference and noise is introduced. In particular, the proposed framework is applicable to emerging wireless communication systems, like cognitive radio networks, providing means for performance prediction and optimization. The analysis of the error behaviour of an intended link in the presence of network interference generated by randomly located nodes is receiving significant attention in current scientific literature, and notable contributions can be found in [23, 50–57]. However, these works have several limitations. In [50, 51] only binary modulation with no fading is considered. In [52], the proposed framework assumes that network interference is conditional Gaussian, which might not be true for many scenarios of interest, [53]. In [54, 55] the authors propose optimal combiners in the presence of network interference, but without conducting performance analysis. In [56, 57], only binary modulation is considered with no background noise. Finally, in [23, 53], the authors propose a very interesting framework applicable to many scenarios. However, this framework is semi-analytical and Monte Carlo methods are required to remove conditioning over network interference, even tough with the advantage of avoiding extensive system-level simulations.

Here, a novel framework developed starting from the work recently introduced by Pinto and Win [53] is proposed, and it provides a new mathematical model offering a simple single-integral expression of the ASEP on an intended link subject to network interference and receiver noise. As for the results obtained in the previous chapters, the framework is exact and does not require lengthy Monte Carlo methods for its

computation. Moreover, it is applicable to both asynchronous and synchronous scenarios. The numerical results, substantiated through Monte Carlo simulations, will show that in both scenarios the performance are almost the same. Furthermore, the ASEP in the presence of synchronous interference provides a very tight Upper Bound of the ASEP for asynchronous interference. This is a relevant result, as in the former case all parameters of interest can be computed in closed-form. The framework proposed in this chapter can be found in [3].

4.1 System Model

The system model is the same as that provided in [53], and is almost identical to the one taken into account for coverage probability and average rate in the previous chapters. The network nodes are deployed according to a 2D homogeneous Poisson Point Process with density λ, and the focus will be on the Average Symbol Error Probability of an intended link between a pair of transmitting and receiving nodes, namely TX_0 and RX_0. Thanks to Slivnyak's Theorem (Section A.3), RX_0 can be assumed to be located in the origin of the 2D Euclidean plane. Furthermore, it is also assumed that the distance between the intended transmitter and receiver is fixed and equal to R_0. All the other network nodes belonging to the homogeneous PPP act as interferers, and it is assumed that they transmit on the same band of the intended link.

4.1.1 Definitions and Assumptions

In the following, the definitions and system assumptions listed below hold:

- the distance between the origin (*i.e.* the intended receiver position) and the i-th interfering node is denoted by R_i, for $i \in \Phi_{\mathrm{TX}}^{\{\setminus \mathrm{TX}_0\}}$, where $\Phi_{\mathrm{TX}}^{\{\setminus \mathrm{TX}_0\}}$ is the homogeneous Poisson Point Process of all the transmitting nodes except the intended one, TX_0;

- the intended and interfering nodes transmit symbols belonging to a MPSK modulation scheme. The symbol period is denoted by T, and it is assumed to be the same for all the nodes in the network. The generic complex MPSK symbols emitted by TX_0 and the i-th interfering node are denoted by $s_0 = a_0 \exp(j\theta_0)$ and $s_i = a_i \exp(j\theta_i)$ respectively;

- the intended and interfering nodes transmit with the same average energy per symbol, denoted by E_0 and E_I respectively, and all the interfering nodes use the same transmission energy;

- the transmissions of the interfering nodes are independent and asynchronous. In particular, the transmission delay at the intended receiver of the i-th interfering node is denoted by D_i, which is assumed to be a uniform random variable $\mathcal{U}[0,T)$. The random variables D_i, for $i \in \Phi_{\mathrm{TX}}^{\{\setminus \mathrm{TX}_0\}}$, are assumed to be independent;

- without any loss of generality, the transmission delay between the intended transmitter and receiver is assumed to be equal to zero, *i.e.* TX_0 and RX_0 are perfectly synchronized in time, phase and frequency, and an optimum coherent decoder is used;

- the additive noise at the input of the intended receiver is assumed to be White Complex Circularly Symmetric Gaussian, with power spectral density equal to $N_0/2$ per dimension.

According to the definitions and assumptions provided above, the channel model is assumed to be as follows:

- the fast-fading has a Rayleigh distribution in all the wireless links. In particular, the complex fading gain of the intended and i-th interfering links are denoted respectively by $\alpha_0 = |\alpha_0| \exp(j\phi_0)$ and $\alpha_i = |\alpha_i| \exp(j\phi_i)$, for $i \in \Phi_{\mathrm{TX}}^{\{\setminus \mathrm{TX}_0\}}$, where: (i) $|\alpha_0|$, $|\alpha_i|$ are Rayleigh distributed with parameter $\Omega_0 = \mathbb{E}_{\alpha_0}\left\{|\alpha_0|^2\right\} = 1$ and $\Omega_I = \mathbb{E}_{\alpha_i}\left\{|\alpha_i|^2\right\} = 1$ for $i \in \Phi_{\mathrm{TX}}^{\{\setminus \mathrm{TX}_0\}}$; and (ii) ϕ_0, ϕ_i are the channel phases uniformly distributed over the interval $[0, 2\pi)$;

- the shadowing follows a Lognormal distribution in all the wireless links. In particular, the shadowing gain of the i-th interfering link is denoted by $S_i = \exp(\sigma_I G_i)$, where σ_I is the standard deviation of the shadowing in Neper[1] and G_i for $i \in \Phi_{\mathrm{TX}}^{\{\setminus \mathrm{TX}_0\}}$ are independent standard Gaussian random variables with zero mean and unit standard deviation;

- slow power control is used on the intended link [22], and thus the shadowing gain $S_0 = \exp(\sigma_0 G_0)$ can be assumed to be fixed;

[1] Denoting the standard deviation in dB as σ_{dB}, the corresponding value in Neper is given by $\sigma = \frac{\ln(10)}{20}\sigma_{\mathrm{dB}}$.

- the path-loss model is assumed to follow an exponential-decaying law in all wireless links. In particular, the transmitted power of both the intended and the i-th interfering links decays with the transmission distance according to the functions $\ell_0 = \frac{\kappa_0}{R_0^{b_0}}$ and $\ell_i = \frac{\kappa_I}{R_i^{b_I}}$ for $i \in \Phi_{\mathrm{TX}}^{\{\backslash \mathrm{TX}_0\}}$ respectively, where κ_0, κ_I are environment-dependent constants, and $b_0 > 1$, $b_I > 1$ denote the path-loss exponents.

An important remark is that, in the proposed channel model, all the interfering nodes are i.i.d. with common fast-fading (Ω_I), shadowing (σ_I), and path-loss (κ_I, b_I) parameters. The combined channel gain at the intended receiver RX_0 of the intended transmitter and the i-th interfering node is respectively given by $h_0 = \alpha_0 S_0 \ell_0$ and $h_i = \alpha_i S_i \ell_i$, for $i \in \Phi_{\mathrm{TX}}^{\{\backslash \mathrm{TX}_0\}}$.

4.1.1.1 Baseband Representation of the Interference

Denoting the operating frequency by f_c, and according to the definitions and assumptions provided in the above section, the overall bandpass signal received at the intended node RX_0 can be written as [53]:

$$z(t) = \frac{\kappa_0 \alpha_0 e^{\sigma_0 G_0}}{R_0^{b_0}} \sqrt{\frac{2}{T}} a_0 \cos\left(2\pi f_c t + \theta_0\right) + \mathcal{I}(t) + w(t)$$

where the first term represents the intended signal, $\mathcal{I}(t)$ is the aggregate interference, and $w(t)$ is the noise. In particular, the bandpass aggregate interference is given by [53, Eq.(1)]:

$$\begin{aligned} \mathcal{I}(t) = \sum_{i=1}^{\infty} \frac{\kappa_I \alpha_i e^{\sigma_I G_i}}{R_i^{b_I}} \Bigg[& \sqrt{\frac{2}{T}} a_i \cos\left(2\pi f_c t + \theta_i + \phi_i\right) u(D_i - t) + \\ & + \sqrt{\frac{2}{T}} \overline{a}_i \cos\left(2\pi f_c t + \overline{\theta}_i + \phi_i\right) u(t - D_i) \Bigg], 0 \le t \le T \end{aligned} \tag{4.1}$$

where $u(t)$ is the unit step function. It is worth noting that $s_i = a_i \exp\left(j\theta_i\right)$ and $\overline{s}_i = \overline{a}_i \exp\left(j\overline{\theta}_i\right)$ denote a pair of successive symbols transmitted by the same interfering user. It is necessary to consider two symbols because of the assumption of asynchronous communication systems.

The intended receiver RX_0 coherently demodulates the received signal $z(t)$ through the orthonormal base $\left\{\psi_1(t) = \sqrt{\frac{2}{T}} \cos(2\pi f_c t), \psi_1(t) = -\sqrt{\frac{2}{T}} \sin(2\pi f_c t)\right\}$, and thus the baseband aggregate interference can be written as [53, Eq.(8)]:

$$\mathcal{I} = \sum_{i=1}^{\infty} \frac{e^{\sigma_I G_i}}{R_i^{b_I}} \left(X_{i,p} + j X_{i,q}\right) \tag{4.2}$$

where $X_{i,p}$ and $X_{i,q}$ are related to the in-phase (p) and quadrature (q) components of the demodulated aggregate interference $\mathcal{I}$:

$$\begin{aligned} X_{i,p} &= \kappa_I \alpha_i \left[a_i \frac{D_i}{T} \cos\left(\theta_i + \phi_i\right) + \overline{a}_i \left(1 - \frac{D_i}{T}\right) \cos\left(\overline{\theta}_i + \phi_i\right) \right] \\ X_{i,q} &= \kappa_I \alpha_i \left[a_i \frac{D_i}{T} \sin\left(\theta_i + \phi_i\right) + \overline{a}_i \left(1 - \frac{D_i}{T}\right) \sin\left(\overline{\theta}_i + \phi_i\right) \right] \end{aligned} \tag{4.3}$$

It is worthwhile noting that, considering the synchronous scenario, *i.e.* $D_i = 1$ or $0\ \forall i \in \Phi_{\mathrm{TX}}^{\{\setminus \mathrm{TX}_0\}}$, and assuming $\kappa_I = 1$, the aggregate interference power shown in equation (2.3) (see Chapter 2) is given by the sum of the squares (power) of the single terms in equation (4.2), as $R_i^{-2b_I} = R_i^{-\alpha}$ and $|\alpha_i|^2 = |\tilde{h}_i|^2$.

4.1.1.2 Meaning of the Average

After the introduction of so many random variables for the computation of the ASEP, some clarifying observations are worth being made on the physical meaning of "average". On the one hand, the Symbol Error Probability is averaged over fading statistics (fast-fading and shadowing) and random positions, R_i for $i \in \Phi_{\mathrm{TX}}^{\{\setminus \mathrm{TX}_0\}}$, of all the interfering nodes. On the other hand, the average for the intended link is computed only over fast-fading, as according to the assumptions made in the previous section the shadowing S_0 and the distance R_0 are fixed values.
This average performance metric is extremely useful for proper network planning and optimization in several scenarios of interest. As an example, two possible cases are described:

1. as stated in [23], the interferers have a short session life-time compared to the duration of the intended communication. Thus, each interfering node periodically becomes active, transmitting bursts of symbols, and then goes back to an idle state. In this case, the set of interfering nodes, *i.e.* fading/shadowing and spatial positions, varies so often that the interference process can be assumed ergodic, and averages over fading, shadowing, and spatial positions are meaningful;

2. in many scenarios, like cognitive networks, *ad hoc* networks or femtocell-overlaid networks [22, 25], the positions of the interfering nodes are unknown to the network designer *a priori*. In this case, the interest is on the performance of an average network configuration, *i.e.* the performance obtained by averaging over all the possible network configurations, which implies averag-

ing over fading, shadowing, and randomly distributed spatial locations of the interferers.

4.1.2 Problem Statement

In [53, Eq.(25)], by exploiting Slivnyak's and PGFL (Section A.2) theorems, as well as the decomposition property of alpha-stable random variables[2], the authors provided the following integral form of the ASEP for MPSK modulation and Rayleigh fading:

$$\text{ASEP} = \frac{1}{\pi} \int_0^{\frac{M-1}{M}\pi} \mathbb{E}_{\mathcal{B}} \left\{ \left(1 + \frac{\sin^2\left(\frac{\pi}{M}\right)}{\sin^2(\xi)} \eta_{\mathcal{B}} \right)^{-1} \right\} \mathrm{d}\xi \tag{4.4}$$

where:

- from (4.2) and (B.4), $\mathcal{I} = \sqrt{\mathcal{B}}\mathbf{G}$;
- $\mathcal{B} \sim \mathcal{S}\left(\tilde{\alpha} = \frac{1}{b_I}, \tilde{\beta} = 1, \tilde{\gamma} = \cos^{b_I}\left(\frac{\pi}{2b_I}\right)\right)$, *i.e.* $\mathcal{B}$ belongs to a real skewed stable distribution with characteristic exponent $\tilde{\alpha} \in (0, 2]$, skewness $\tilde{\beta} \in [-1, 1]$, and dispersion $\tilde{\gamma} \in [0, \infty)$;
- $\eta_{\mathcal{B}} = \frac{\kappa_0^2 E_0 \Omega_0 S_0^2}{R_0^{2b_0} \sigma_{\mathcal{B}}^2}$ is the received SNR averaged over the fast-fading, with $\sigma_{\mathcal{B}}^2 = \mathcal{B} E_I \sigma_I^2 + N_0$;
- $\sigma_I^2 = 4\kappa_I^2 \Omega_I \left(\pi \lambda \mathcal{X}_I \mathcal{C}_{2/b_I}^{-1}\right)^{b_I}$, where $\mathcal{C}_{2/b_I}$ is given by:

$$\mathcal{C}_{2/b_I} = \begin{cases} \left(1 - \frac{2}{b_I}\right) \left[\Gamma\left(2 - \frac{2}{b_I}\right) \cos\left(\frac{\pi}{b_I}\right)\right]^{-1}, & b_I \neq 2 \\ \frac{2}{\pi}, & b_I = 2 \end{cases} \tag{4.5}$$

and for Rayleigh fading $\mathcal{X}_I = \mathbb{E}\left\{ |X_{i,p} + jX_{i,q}|^{\frac{2}{b_I}} \right\}$ can be written as:

$$\begin{aligned} \mathcal{X}_I = & \exp\left(\frac{2\sigma_I^2}{b_I^2}\right) \Gamma\left(1 + \frac{1}{b_I}\right) \\ & \times \mathbb{E}_{a_i, \theta_i, \overline{a}_i, \overline{\theta}_i, \phi_i, D_i} \left\{ \left| \frac{a_i D_i}{T} \cos(\theta_i + \phi_i) + \overline{a}_i \left(1 - \frac{D_i}{T}\right) \cos\left(\overline{\theta}_i + \phi_i\right) \right|^{\frac{2}{b_I}} \right\} \end{aligned} \tag{4.6}$$

In the above equation, $\mathbb{E}_{a_i, \theta_i, \overline{a}_i, \overline{\theta}_i, \phi_i, D_i}\{\cdot\}$ is the expectation computed over information symbols, channel phases, and propagation delays of the interferers. Moreover, since the interfering signals are i.i.d., this expectation is the same for each interferer.

[2] See equation (B.4) in Appendix B or [58].

The result summarized in equation (4.4) is highly remarkable as it avoids the need for pure network simulations [53]. However, this framework is semi-analytical as the expectation $\mathbb{E}_{\mathcal{B}}\{\cdot\}$ must be computed by using Monte Carlo methods. Furthermore, the expectation in (4.6) has to be numerically evaluated as well. The main purpose of this chapter is to provide a simplified expression of (4.4) by completely avoiding Monte Carlo simulations.

4.2 Single-integral Expression of the ASEP

In [59] the authors provide an integral expression of the moments of the Lognormal power sum, denoted as $S^{(N_p)}$, in the logarithmic domain. In particular, this allows to compute the MGF of the Lognormal power sum, denoted as Log-MGF. [59, Eq.(6)] states that:

$$\mathcal{M}_{S^{(N_p)}}(p) = \mathbb{E}_S\left\{S^{-p}\right\} = \frac{1}{\Gamma(p)} \int_0^\infty z^{(p-1)} \mathcal{M}_S(z) \mathrm{d}z \tag{4.7}$$

The above formula can be applied in order to write the expectation in equation (4.4) in a different form. In particular, the ASEP can be written as:

$$\text{ASEP} = \frac{1}{\pi} \int_0^{\frac{M-1}{M}\pi} \left[\int_0^\infty \mathcal{M}_{\mathcal{Z}_\xi}(z;\xi) \mathrm{d}z \right] \mathrm{d}\xi \tag{4.8}$$

where $\mathcal{M}_{\mathcal{Z}_\xi}(z;\xi) = \mathbb{E}_{\mathcal{Z}_\xi}\left\{\exp\left(-z\mathcal{Z}_\xi\right)\right\}$ is the Moment Generating function of the random variable $\mathcal{Z}_\xi = 1 + \left(\frac{\sin^2(\pi/M)}{\sin^2(\xi)}\right)\eta_{\mathcal{B}}$. By definition, this MGF is given by:

$$\mathcal{M}_{\mathcal{Z}_\xi}(z;\xi) = \exp(-p)\mathcal{M}_{\eta_{\mathcal{B}}}\left(z\frac{\sin^2\left(\frac{\pi}{M}\right)}{\sin^2(\xi)}\right) \tag{4.9}$$

where $\mathcal{M}_{\eta_{\mathcal{B}}}(z) = \mathbb{E}_{\eta_{\mathcal{B}}}\left\{\exp\left(-z\eta_{\mathcal{B}}\right)\right\}$. The MGF of $\eta_{\mathcal{B}}$ can be evaluated as:

$$\begin{aligned}
\mathcal{M}_{\eta_{\mathcal{B}}}(z) &= \mathbb{E}_{\eta_{\mathcal{B}}}\left\{\exp\left(-z\eta_{\mathcal{B}}\right)\right\} \\
&\overset{(a)}{=} \mathbb{E}_{\mathcal{B}}\left\{\exp\left(-z\frac{\kappa_0^2 E_0 \Omega_0 S_0^2}{R_0^{2b_0}\left(\mathcal{B}E_I\sigma_I^2 + N_0\right)}\right)\right\} \\
&\overset{(b)}{=} 1 - \sqrt{z}\int_0^\infty t^{-1/2} J_1\left(2\sqrt{zt}\right)\mathcal{M}_{\eta_{\mathcal{A}}}(t)\mathrm{d}t
\end{aligned}$$

where (a) follows from the definition of the random variable $\eta_{\mathcal{B}}$ provided in the previous section, (b) follows from [45, Theorem 1] by introducing the random variable

$\eta_{\mathcal{A}} = \frac{1}{\eta_{\mathcal{B}}}$, and $J_\nu(\cdot)$ denotes the Bessel function of the first kind and order ν [38, Chapter 9]. Finally, the derivation of $\mathcal{M}_{\eta_{\mathcal{B}}}$ can be concluded as:

$$\begin{aligned}\mathcal{M}_{\eta_{\mathcal{B}}}(z) &\overset{(c)}{=} 1-\sqrt{z}\int_0^\infty t^{-1/2}J_1\left(2\sqrt{zt}\right)\exp\left(-\frac{\Psi_0}{\gamma_0}t\right)\mathcal{M}_{\mathcal{B}}\left(\Psi_0\sigma_I^2\frac{\gamma_I}{\gamma_0}t\right)\mathrm{d}t \\ &\overset{(d)}{=} 1-\sqrt{z}\int_0^\infty t^{-1/2}J_1\left(2\sqrt{zt}\right)\exp\left(-\frac{\Psi_0}{\gamma_0}t\right)\exp\left(-\left(\Psi_0\sigma_I^2\frac{\gamma_I}{\gamma_0}\right)^{\frac{1}{b_I}}t^{1/b_I}\right)\mathrm{d}t\end{aligned} \tag{4.10}$$

where (c) follows from the definition of $\eta_{\mathcal{A}}$, $\gamma_0 = E_0/N_0$ and $\gamma_I = E_I/N_0$ denote the Signal energy-to-Noise spectral density-Ratio for the intended (SNR) and interfering (INR) links respectively, $\Psi_0 = \frac{R_0^{2b_0}}{\kappa_0^2\Omega_0 S_0}$, and $\mathcal{M}_{\mathcal{B}}(z) = \mathbb{E}_{\mathcal{B}}\left\{\exp\left(-z\mathcal{B}\right)\right\}$ is the MGF of the random variable $\mathcal{B}$. In conclusion, step (d) follows from [58] where it is shown that the MGF of the real skewed stable random variable $\mathcal{B}$ is available in closed-from as $\mathcal{M}_{\mathcal{B}}(z) = \exp\left(-z^{1/b_I}\right)$.

Substituting (4.10) in equation (4.8) the following form of the Average Symbol Error Probability can be obtained:

$$\begin{aligned}\mathrm{ASEP} = \frac{M-1}{M}\pi - \frac{1}{\pi}\int_0^{\frac{M-1}{M}\pi}\Bigg\{\int_0^\infty t^{-1/2}\exp\left(-\frac{\Psi_0}{\gamma_0}t\right) \\ \times\exp\left(-\left(\Psi_0\sigma_I^2\frac{\gamma_I}{\gamma_0}\right)^{\frac{1}{b_I}}t^{1/b_I}\right)\mathcal{T}\left(t,\xi\right)\mathrm{d}t\Bigg\}\mathrm{d}\xi\end{aligned} \tag{4.11}$$

where the function $\mathcal{T}(\cdot,\cdot)$ is given by:

$$\begin{aligned}\mathcal{T}\left(t,\xi\right) &= \sqrt{\frac{\sin^2\left(\frac{\pi}{M}\right)}{\sin^2\left(\xi\right)}}\int_0^\infty\sqrt{z}\exp(-z)J_1\left(2\sqrt{\frac{\sin^2\left(\frac{\pi}{M}\right)}{\sin^2\left(\xi\right)}}\sqrt{t}\sqrt{z}\right)\mathrm{d}z \\ &\overset{(a)}{=} \sqrt{t}\frac{\sin^2\left(\frac{\pi}{M}\right)}{\sin^2\left(\xi\right)}{}_1F_1\left(2;2;-\frac{\sin^2\left(\frac{\pi}{M}\right)}{\sin^2\left(\xi\right)}t\right) \\ &\overset{(b)}{=} \sqrt{t}\frac{\sin^2\left(\frac{\pi}{M}\right)}{\sin^2\left(\xi\right)}\exp\left(-\frac{\sin^2\left(\frac{\pi}{M}\right)}{\sin^2\left(\xi\right)}t\right)\end{aligned} \tag{4.12}$$

In the above expression, (a) follows from [40, Eq.(6.631)], ${}_1F_1(\cdot;\cdot;\cdot)$ is the Kummer confluent hypergeometric function defined in [38, Chapter 13], and (b) follows from the known identity ${}_1F_1(2;2;\pm x) = \exp(\pm x)$. Furthermore, substituting the above closed-from expression of $\mathcal{T}(\cdot,\cdot)$ in equation (4.11) yields to:

$$\mathrm{ASEP} = \frac{M-1}{M}\pi - \frac{1}{\pi}\int_0^\infty\exp\left(-\frac{\Psi_0}{\gamma_0}t\right)\exp\left(-\left(\Psi_0\sigma_I^2\frac{\gamma_I}{\gamma_0}\right)^{\frac{1}{b_I}}t^{1/b_I}\right)\mathcal{Q}(t)\mathrm{d}t \tag{4.13}$$

with:

$$\begin{aligned}\mathcal{Q}(t) &= \int_0^{\frac{M-1}{M}\pi} \frac{\sin^2\left(\frac{\pi}{M}\right)}{\sin^2(\xi)} \exp\left(-\frac{\sin^2\left(\frac{\pi}{M}\right)}{\sin^2(\xi)} t\right) \mathrm{d}\xi \\ &\overset{(a)}{=} \frac{1}{2}\sqrt{\frac{\pi}{t}} \sin\left(\frac{\pi}{M}\right) \exp\left(-t\sin^2\left(\frac{\pi}{M}\right)\right) \left[1 + \mathrm{erf}\left(\sqrt{t}\cos\left(\frac{\pi}{M}\right)\right)\right]\end{aligned} \tag{4.14}$$

with $\mathrm{erf}(x) = \frac{2}{\sqrt{\pi}} \int_0^x \exp\left(-t^2\right) \mathrm{d}t$ being the error function. In the above equation, (a) follows from the closed-from solution of the indefinite integral:

$$\int \left[\frac{\mu^2}{\sin^2(\xi)}\right] \exp\left(\frac{-\mu^2 t}{\sin^2(\xi)}\right) \mathrm{d}\xi = -\frac{1}{2}\sqrt{\pi}\mu t^{-1/2} \exp\left(-\mu^2 t\right) \mathrm{erf}\left(\mu\cot(\xi)\sqrt{t}\right)$$

and from the notable limit $\lim_{x\to 0}[\mathrm{erf}(\xi\cot(x))] = 1$ for any constant $\xi > 0$. Finally, by substituting (4.14) in (4.13), the following single-integral expression of the ASEP can be obtained:

$$\begin{aligned}\mathrm{ASEP} =& \frac{M-1}{M}\pi - \frac{\sin\left(\frac{\pi}{M}\right)}{2\sqrt{\pi}} \int_0^\infty \left\{ \frac{1}{\sqrt{t}} \exp\left[-\left(\frac{\Psi_0}{\gamma_0} + \sin^2\left(\frac{\pi}{M}\right)\right) t\right] \right. \\ & \left. \times \exp\left[-\left(\Psi_0\sigma_I^2\frac{\gamma_I}{\gamma_0}\right)^{\frac{1}{b_I}} t^{1/b_I}\right] \left[1 + \mathrm{erf}\left(\sqrt{t}\cos\left(\frac{\pi}{M}\right)\right)\right] \right\} \mathrm{d}t\end{aligned} \tag{4.15}$$

It can be noticed that the above expression of the ASEP is extremely simple, and its computational complexity is similar to many conventional modulation schemes without network interference [36]. This single-integral form can be efficiently computed using conventional quadrature rule methods [38, Chapter 25], as the Gauss-Chebyshev Quadrature integration rule provided in [38, Eq.(9)] and introduced in Section 3.2.1 (see equation (3.10)). As a sanity check, it was also verified that when $\gamma_I \to 0 \Rightarrow E_I \to 0$, the framework actually reduces to well-known formulas of the Average Symbol Error Probability without interference [36].

It is worthwhile noting that the main design parameters, *i.e.* the symbol transmit energy of intended and interfering links (in γ_0 and γ_I respectively), the fading, shadowing, and path-loss parameters for intended and interfering links (in Ψ_0 and σ_I^2), the modulation order M and the path-loss exponent of the interfering links b_I, are clearly shown in (4.15). This novel framework is thus not only simple to compute, as it avoids Monte Carlo methods, but allows to easily understand the system performance under several practical scenarios as well.

4.2.1 Closed-form Expression of $\mathcal{X}_I$ for Synchronous Systems

The single-integral expression of the ASEP provided in equation (4.15) does not require Monte Carlo methods for its computation. However, some parameters that appear in it still have to be computed numerically. In particular, $\mathcal{X}_i$, defined in (4.6), is not available in closed-form. In this section, a closed-form expression of this parameter will be provided for a network setup where all the interfering transmitters are synchronous with the intended one, *i.e.* $D_i = 0$ for $i \in \Phi_{\mathrm{TX}}^{\{\backslash \mathrm{TX}_0\}}$. Moreover, in Section 4.3, it will be shown that this scenario turns out to provide a tight Upper Bound for the asynchronous case.

When $D_i = 0$, for $i \in \Phi_{\mathrm{TX}}^{\{\backslash \mathrm{TX}_0\}}$, and considering that for MPSK modulations the equality $a_i = \overline{a}_i = 1$, for $i \in \Phi_{\mathrm{TX}}^{\{\backslash \mathrm{TX}_0\}}$, holds, equation (4.6) simplifies to:

$$\begin{aligned} \mathcal{X}_I &= \exp\left(\frac{2\sigma_I^2}{b_I^2}\right)\Gamma\left(1+\frac{1}{b_I}\right)\mathbb{E}_{\overline{\theta}_i,\phi_i}\left\{\left|\cos\left(\overline{\theta}_i+\phi_i\right)\right|^{\frac{2}{b_I}}\right\} \\ &= \exp\left(\frac{2\sigma_I^2}{b_I^2}\right)\Gamma\left(1+\frac{1}{b_I}\right)\mathbb{E}_{\overline{\theta}_i,\phi_i}\left\{\Upsilon_I^{1/b_I}\right\} \end{aligned} \tag{4.16}$$

where the random variable $\Upsilon_I = \left|\cos\left(\overline{\theta}_i+\phi_i\right)\right|^2$ was introduced. Applying [59, Eq.(6)] (see (4.7)), the expectation of Υ_I^{1/b_I} can be written as:

$$\mathbb{E}_{\overline{\theta}_i,\phi_i}\left\{\Upsilon_I^{1/b_I}\right\} = \mathbb{E}_{\Upsilon_I}\left\{\Upsilon_I^{1/b_I}\right\} = \frac{1}{\Gamma\left(\frac{1}{b_I}\right)}\int_0^\infty \xi^{\left(\frac{1}{b_I}-1\right)}\mathcal{M}_{\frac{1}{\Upsilon_I}}(\xi)\mathrm{d}\xi \tag{4.17}$$

where $\mathcal{M}_{\frac{1}{\Upsilon_I}}(\cdot)$ is the MGF of $\frac{1}{\Upsilon_I}$. This latter MGF can be evaluated using [45, Theorem 1] as follows:

$$\begin{aligned} \mathcal{M}_{\frac{1}{\Upsilon_I}}(z) &= 1-\sqrt{z}\int_0^\infty t^{-1/2}J_1\left(2\sqrt{zt}\right)\mathcal{M}_{\Upsilon_I}(t)\mathrm{d}t \\ &\overset{(a)}{=} -\int_0^\infty J_0\left(2\sqrt{zt}\right)\left[\frac{\mathrm{d}}{\mathrm{d}x}\mathcal{M}_{\Upsilon_I}(x)\right]_{x=t}\mathrm{d}t \end{aligned} \tag{4.18}$$

where $\mathcal{M}_{\Upsilon_I}(\cdot)$ is the MGF of Υ_I, and (a) follows from integration by parts and the following known indefinite integral:

$$\int t^{-1/2}J_1\left(\sqrt{zt}\right)\mathrm{d}t = -p^{-1/2}\left[J_0\left(2\sqrt{zt}\right)-1\right]$$

The Bessel function $J_0(\cdot)$ can be expressed in terms of the Meijer-G function, introduced in Section 2.2.1. In [42, Eq.(8.4.19.1)] it is shown that:

$$J_\nu\left(2\sqrt{x}\right) = G_{0,2}^{1,0}\left(x\,\middle|\,\begin{matrix}-,-\\ \frac{\nu}{2},-\frac{\nu}{2}\end{matrix}\right) \tag{4.19}$$

and thus, from (4.18), $J_0\left(2\sqrt{zt}\right) = G_{0,2}^{1,0}\left(zt\left|\begin{matrix}-,-\\0,0\end{matrix}\right.\right)$. Plugging (4.18) in (4.17) and computing the Mellin transform of the Meijer-G function, with the help of the integration provided in [42, Eq.(2.24.2.1)], finally leads to:

$$\begin{aligned}\mathbb{E}_{\overline{\theta}_i,\phi_i}\left\{\Upsilon_I^{1/b_I}\right\} &= -\frac{1}{\Gamma\left(\frac{1}{b_I}\right)}\int_0^\infty\left[\frac{\mathrm{d}}{\mathrm{d}x}\mathcal{M}_{\Upsilon_I}(x)\right]_{x=t}\left\{\int_0^\infty \xi^{\left(\frac{1}{b_I}-1\right)}J_0\left(2\sqrt{\xi t}\right)\mathrm{d}\xi\right\}\mathrm{d}t\\ &= -\frac{1}{\Gamma\left(1-\frac{1}{b_I}\right)}\int_0^\infty t^{-1/b_I}\left[\frac{\mathrm{d}}{\mathrm{d}x}\mathcal{M}_{\Upsilon_I}(x)\right]_{x=t}\mathrm{d}t \qquad (4.20)\end{aligned}$$

Thus, in orer to obtain a closed-form expression of $\mathcal{X}_I$, the above integral has to be solved. This computation can be performed by finding a closed-form expression of $\mathcal{M}_{\Upsilon_I}(\cdot)$. In particular, by the definition of Υ_I:

$$\begin{aligned}\mathcal{M}_{\Upsilon_I}(z) &= \mathbb{E}_{\Upsilon_I}\left\{\exp\left(-z\left|\cos\left(\overline{\theta}_i+\phi_i\right)\right|^2\right)\right\}\\ &\overset{(a)}{=} \frac{1}{2\pi}\int_0^{2\pi}\exp\left[-z\cos^2\left(\overline{\theta}_i+\xi\right)\right]\mathrm{d}\xi\\ &\overset{(b)}{=} \exp\left(-\frac{z}{2}\right)I_0\left(\frac{z}{2}\right) \qquad (4.21)\end{aligned}$$

where (a) follows from the uniform distribution of the random variables $\phi_i \sim \mathcal{U}[0,2\pi)$ for $i \in \Phi_{\mathrm{TX}}^{\{\backslash \mathrm{TX}_0\}}$, and (b) can be obtained from [60, Eq.(14)] which provides the following integral:

$$\int_0^{2\pi}\int_0^{2\pi}\exp\left[2s\beta_1\beta_2\cos(\phi_1-\phi_2)\right]\mathrm{d}\phi_1\mathrm{d}\phi_2 = (2\pi)^2 I_0\left(2s\beta_1\beta_2\right)$$

with $I_\nu(\cdot)$ being the modified Bessel function of the first kind and order ν, defined in [38, Chapter 23].

Finally, substituting (4.21) in (4.20), and computing the derivative yields to:

$$\begin{aligned}\mathbb{E}_{\overline{\theta}_i,\phi_i}\left\{\Upsilon_I^{1/b_I}\right\} &= \frac{1}{2\Gamma\left(1-\frac{1}{b_I}\right)}\int_0^\infty t^{-1/b_I}\exp\left(-\frac{t}{2}\right)I_0\left(\frac{t}{2}\right)\mathrm{d}t\\ &\quad -\frac{1}{2\Gamma\left(1-\frac{1}{b_I}\right)}\int_0^\infty t^{-1/b_I}\exp\left(-\frac{t}{2}\right)I_1\left(\frac{t}{2}\right)\mathrm{d}t\\ &\overset{(a)}{=} \frac{1}{2\sqrt{\pi}\Gamma\left(\frac{1}{b_I}\right)}\Gamma\left(\frac{1}{b_I}-\frac{1}{2}\right) - \frac{\Gamma\left(2-\frac{1}{b_I}\right)\Gamma\left(\frac{1}{b_I}-\frac{1}{2}\right)}{2\sqrt{\pi}\Gamma\left(1-\frac{1}{b_I}\right)\Gamma\left(1+\frac{1}{b_I}\right)}\end{aligned} \qquad (4.22)$$

where (a) is obtained solving each integral by first expressing the Bessel function $I_\nu(\cdot)$ in terms of the Meijer-G function, as in [42, Eq.(8.4.22.3)], and then computing the Mellin transform of the Meijer-G function applying [42, Eq.(2.24.2.1)]. Substituting (4.22) in equation (4.16) provides the closed-form expression of $\mathcal{X}_I$ for the synchronous scenario:

$$\mathcal{X}_I = \exp\left(\frac{2\sigma_I^2}{b_I^2}\right)\frac{\Gamma\left(\frac{1}{b_I}-\frac{1}{2}\right)}{2b_I\sqrt{\pi}} - \exp\left(\frac{2\sigma_I^2}{b_I^2}\right)\frac{\Gamma\left(2-\frac{1}{b_I}\right)\Gamma\left(\frac{1}{b_I}-\frac{1}{2}\right)}{2\sqrt{\pi}\Gamma\left(1-\frac{1}{b_I}\right)} \tag{4.23}$$

where the known identity $\Gamma(\delta+1)=\delta\Gamma(\delta)$ was used.

4.3 Numerical Results

In this section, the proposed analytical framework is compared with Monte Carlo simulations. As for the computation of coverage probability and average rate, the nodes were randomly distributed in the 2D Euclidean plane according to a homogeneous Poisson Point Process, but in this case the whole communication system, *i.e.* modulator, channel, and demodulator, was implemented. The same signal model as in [53, Eq.(1)] was modeled, and no *a priori* model has been assumed for the network interference. The truncation radius for the proper simulation of an infinite network was chosen according to [32]. With the parameters used in this study, a truncation radius equal to 40 was sufficient to avoid truncation errors. According to Figures 4.1-4.2, the following observations can be made:

- in Figure 4.1, the interfering nodes are assumed to have constant energy, *i.e.* γ_I is fixed, while the intended user increases its transmission energy, *i.e.* γ_0. It can be observed that the ASEP gets better when the SNR increases, while it gets worse for increasing INR, as expected. The interesting result is that there is no error-floor in this case. As far as the accuracy of the proposed analytical derivation is concerned, it can be noted that simulations and framework results closely overlap. Furthermore, by comparing the results for the asynchronous system (a), in which $\mathcal{X}_I$ is computed numerically, with the results for the synchronous system (b), in which $\mathcal{I}$ is given by (4.23), it can be observed that the ASEP is almost the same. As a matter of facts, the difference between the two cases is negligible. However, a close analisys reveals that the results in Figure 4.1(b) provide a tight Upper Bound for those in Figure 4.1(a);

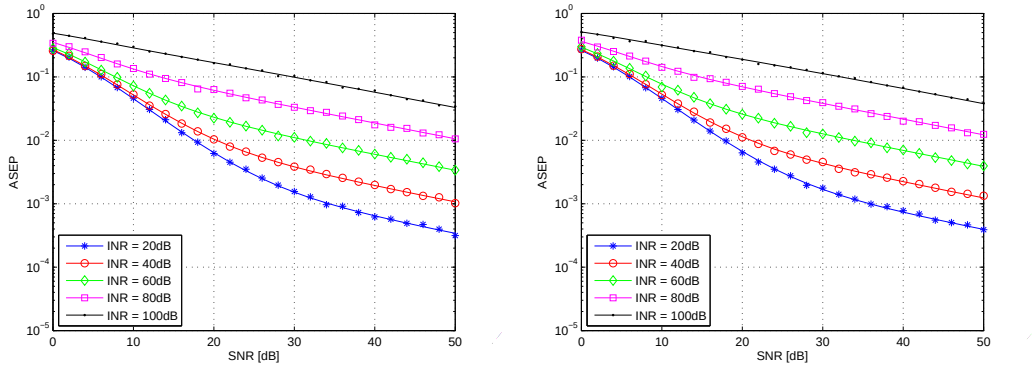

(a) Asynchronous (b) Synchronous

Figure 4.1: ASEP of MPSK modulation for asynchronous (a) and synchronous (b) system setups. Solid lines show the analytical model in (4.15) and markers show Monte Carlo simulations. Setup: i) $M = 4$; ii) $R_0 = 1$, $\kappa_0 = 1$, $G_0 = 1$, $S_0 = \exp(\sigma_0 G_0)$; iii) $b_0 = b_I = 4$; iv) $\sigma_0^{(\mathrm{dB})} = \sigma_I^{(\mathrm{dB})} = 3$ dB; and v) $\lambda = 10^{-3}$.

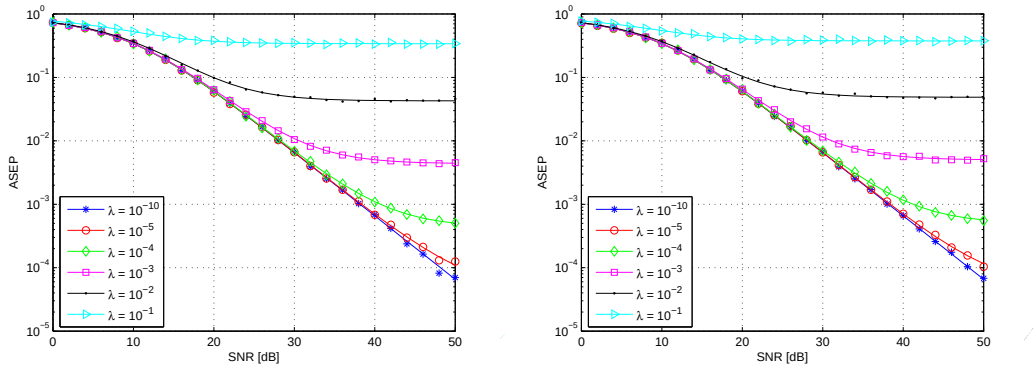

(a) Asynchronous (b) Synchronous

Figure 4.2: ASEP of MPSK modulation for asynchronous (a) and synchronous (b) system setups. Solid lines show the analytical model in (4.15) and markers show Monte Carlo simulations. Setup: i) $M = 16$; ii) $R_0 = 1$, $\kappa_0 = 1$, $G_0 = 1$, $S_0 = \exp(\sigma_0 G_0)$; iii) $b_0 = b_I = 4$; iv) $\sigma_0^{(\mathrm{dB})} = \sigma_I^{(\mathrm{dB})} = 3$ dB; and v) $\gamma_0 = \gamma_I$.

- in Figure 4.2, the interfering nodes use the same transmission energy as the intended user, *i.e.* $\gamma_I = \gamma_0$. It can be noticed that the performance are better for increasing values of the SNR, while they get worse for increasing density of the interfering nodes λ, as expected. Unlike the case studied in Figure 4.1, an error-floor is clearly observable for increasing values of SNR. This behaviour is

due to the increase in the interfering transmission energy, which follows that used by the intended user. Thus, this system tends to be heavily interference-limited. Furthermore, similarly to Figure 4.1, the proposed analytical model is very accurate, and there is only a negligible difference between the asynchronous, Figure 4.2(a), and synchronous, Figure 4.2(b), scenarios. Thus, the closed-form expression of $\mathcal{X}_I$ in (4.23) can be again efficiently used to obtain a tight Upper Bound estimate for the asynchronous scenario.

Part II

Coexistence of Heterogeneous Wireless Communication Systems

The ever increasing demand for multimedia wireless communication systems is a key feature of the ICT world. Wireless communications and internet services have had a pervasive diffusion into our society and profoundly affected our everyday life during the last decade far beyond any expectations. As a matter of facts, during the last years the total number of users subscribing to cellular wireless services have overwhelmed the number of users subscribing to wired telephone services. The buzzword of personal communications, meant to provide "access to anyone, anywhere, at anytime" to the wanted service implies that spectrum demands are dramatically increasing in most developed markets, and the growth of wireless networks and services depends on their availability. Furthermore, in the recent years the internet of things, *i.e.* the internet where physical objects are seamlessly integrated into the information network as active participants, is becoming even more important than the internet of people, due to the far higher amount of objects/devices which nowadays are connected to the web. This accelerating demand for resources is testing the limits of current commercial wireless networks, due to the popularity of portable data-intensive wireless devices: users already accustomed to broadband and multimedia services provided by fixed line operators started requiring the same services while on the move, with the same quality as fixed networks.

Spectrum availability and management in current wireless communication systems is decided by regulatory and licensing bodies. Since Marconi's first wireless communication, the global spectrum management approach is based on a static spectrum allocation model, known as *Command and Control*. According to this paradigm, the available radio spectrum is split into fixed and non-overlapping blocks, separated by appropriate guard bands, and assigned for exclusive use to different services and technologies after a spectrum auction. This static spectrum assignment combined with the phenomenal growth in resource demand is straining the efficiency of this allocation model, thus leading to a commonly shared feeling of spectrum scarcity. It is fundamental to highlight that this is just a feeling. Actually, a large portion of the assigned spectrum is sporadically used: the spectrum usage is concentrated on certain frequencies, while a significant amount of resources is basically unused. In [61], FCC provided a study on the efficiency of spectrum usage, showing that temporal and geographical variations in the utilization of licensed spectrum resources ranges from 15% to 85%. In particular, measurements in the $30-300$ MHz band show that some channels are used less than 1%, whereas the average utilization of all the bands is approximately 5.2%. According to these percentages, the

level of efficiency in spectrum resource utilization is absolutely unacceptable.

In order to cope with this problem, most of the academical, industrial, and regulatory efforts are oriented towards efficient spectrum management. In general, the solutions proposed (and realized, in some cases) so far can be summarized according to the two following approaches: (i) release spectrum bands thanks to novel and more efficient communication techniques, and assign these resources to other services; and (ii) allow smart devices to opportunistically access the temporarily and/or locally available spectrum resources. In the first case, the most known example is probably represented by the Digital Television Broadcasting - Terrestrial (DVB-T) service. Thanks to the OFDM-based transmission, which provides higher spectral efficiency compared to previous transmission techniques, the switch from analogue to digital TV broadcasting is releasing some very valuable portions of the spectrum (the so called *Digital Dividend*) that can be re-allocated to other services. In several countries, the switch-off process has already been completed, and the released spectrum band, 790-862 MHz, has already been allocated to mobile service through public auctions, as in Germany, Sweden, and more recently in Italy. Regarding the second approach, the main technology enabling opportunistic access to the spectrum is given by Cognitive Radios (CRs), first introduced by Joseph Mitola III in 1999 [62]. According to their most common definition, these devices are capable of sensing the surrounding radio environment and, according to this information and to predefined requirements and regulatory policies, can autonomously modify their operating behaviour, subject to not causing harmful interference to the so called Primary Users (PUs), *i.e.* users of a licensed service on the considered band. Of course, an appropriate implementation of these devices would allow to exploit unused spectrum resources in a very efficient way, theoretically close to 100%.

The above approaches actually promise to solve the spectrum scarcity problem. However, they also pose both well known and new coexistence management challenges between communication systems. For instance, consider the switch from analogue to digital TV broadcasting. When some portions of spectrum are released by the TV broadcasting service and assigned to mobile services, both adjacent and co-channel interference among them must be avoided. This is a typical coexistence problem related to new communication systems, which thus needs proper studies. Furthermore, this is not a technical problem only, as it also involves bilateral agreements between neighbouring countries, which might use different systems on the same band. When dealing with opportunistic access to licensed bands, there are

several additional issues to be considered. First of all, such a secondary access can be allowed if and only if no harmful interference is generated on licensed services. This implies many technological challenges, like the ability to sense the presence of primary services or to select the appropriate transmission parameters and protocol such that harmful interference is avoided. Furthermore, even when a Cognitive Radio network correctly fulfills these requirements, fair and efficient spectrum sharing among the CRs in the network still has to be guaranteed.

In this Part, an analysis of coexistence and co-channel interference between broadcasting and mobile service in the Digital Divide bands will be provided in Chapter 5. Then, the attention will be turned on Cognitive Radios. Several feasibility studies will be provided in Chapter 6. These studies were all performed inside SE43, a working group inside CEPT which has the objective of finding the operational characteristics of Cognitive Radio devices for their proper deployment in the available bands inside the spectrum licensed to digital TV broadcasting services. Finally, the possible introduction of Cognitive Radio concepts into hybrid satellite-terrestrial systems will be analyzed in Chapter 7. For a short introduction to Cognitive Radios concepts, the reader might refer to Appendix C.

Chapter 5

Mutual Interference between DVB-T and LTE systems

As stated in the introduction to this Part, the first years of the new millennium saw two driving factors deeply influencing the spectrum management scenarios. On the one hand, users already accustomed to broadband and multimedia services provided by fixed line operators started requiring these services while on the move, with the same quality. This led to an ever increasing demand for new spectrum resources, as well as to an increasing market interest for wireless broadband services. On the other hand, thanks to the greater spectral efficiency of the OFDM transmission technique, the TV switch-over process, *i.e.* the switch from analogue to digital TV broadcasting services, is releasing an extremely valuable portion of the spectrum. This is the so called Digital Dividend, namely the 790-862 MHz band corresponding to channels from 61 to 69, which due to its very favourable propagation characteristics is particularly appealing for wireless broadband services. In order to exploit such an opportunity while satisfying market requests, the last World Radiocommunication Conference (WRC-07) held in Geneva in 2007 allocated on a co-primary basis this band to mobile services[1] in Region 1 (which includes Europe) starting from June 2015. Furthermore, several countries in the European Union were allowed to use this allocation before 2015, subject to technical coordination with neighbouring countries [63]. This decision gave rise to new interference challenges to be coped with: (i) co-channel interference between neighbouring countries or regions, one of them using the 790-862 MHz band for the mobile system and the other for DVB-T;

[1] Exception made for the aeronautical mobile service.

and (ii) adjacent channel interference within a given territory, where frequencies up to 790 MHz are used for DVB-T and those immediately above for the mobile service. In this chapter, an analysis of the co-channel mutual interference between DVB-T and 3GPP Long Term Evolution (LTE) mobile systems is provided [64]. Previous works related to the coexistence between mobile and digital TV broadcasting generally focused on one system to be protected, thus providing the operational constraints for the other system which is considered as interferer. For instance, in [65, 66] the authors provide interesting results obtained considering a UMTS mobile system interfering with a DVB-T system, while in [67] the authors provide an analysis of the mobile radio performance degradation as a consequence of DVB-T interference. In this chapter, a versatile methodology is proposed to take into account both the interference from the mobile system towards the broadcasting system and vice versa. The proposed methodology can be easily adapted and applied to different configurations, for protecting either the DVB-T or the mobile systems. The aim of this work is to identify the most critical radio link in terms of co-channel interference in different scenarios, and define both appropriate guard distances between the interfering systems and transmitters operational characteristics such that specific Quality of Service (QoS) requirements are met. Finally, some considerations and comments are made about the introduction of IMT systems in the 800 MHz bands. Please note that all the results provided in this chapter can be found in [4–10].

5.1 System Layout and Proposed Methodology

In this section, a list of the European regulatory activities dealing with coexistence challenges between mobile and broadcasting systems is presented. After this short insight, the assumptions made on the simulation scenario and on both the mobile and DVB-T systems are provided.

5.1.1 Regulatory Activities

In order to address all the coexistence aspects introduced above, the European Conference of Postal and Telecommunications Administrations (CEPT) set up several study groups. Even if some of them already completed their activity, for the sake of completeness they are all listed below[2]:

[2]Further details on these regulatory activities and their terms of reference are available on CEPT website: http://www.cept.org/.

- SE42 (closed), for the "identification of common and minimal technical conditions in the 790-862 MHz band";
- TG4 "Digital Dividend" (closed), "to provide support when required by SE42 [...] in particular on the protection criteria for broadcasting systems";
- ECC PT1 "IMT matters," for the consideration of the "designation and frequency arrangements for spectrum, identified for IMT in the Radio Regulations and [...] develop appropriate ECC Deliverables, applying to the use of the 3.4-3.6 GHz and 790-862 MHz bands, identified for IMT at WRC-07";
- CPG PT-D Agenda Item 1.17, in order "to consider results of sharing studies between the mobile service and other services in the 790-862 band in Regions 1 and 3, in accordance with Resolution 749 (WRC-07), to ensure the adequate protection of services to which this frequency band is allocated, and take appropriate action".

5.1.2 Simulation Scenario

In order to shed some light on the compatibility challenges between cellular and broadcasting systems, a simple Monte Carlo simulation was performed on the considered area, where both a DVB-T transmitter and a mobile network are present, as depicted in Figure 5.1. These two systems serve adjacent areas, whose reciprocal position depends on the configuration parameters taken into account in the different simulations. The following two cases have been considered in this analysis:

- study case 1: interference generated by a certain number of LTE Base Stations (BSs) on the DVB-T receivers;
- study case 2: interference generated by the DVB-T transmitter on a certain amount of LTE BSs.

It is worthwhile noting that in the second case, only the uplink was taken into account, as it is the most critical link. This is due to the deployment of mobile Base Stations, which are typically rooftop mounted, and thus their height is considerably greater with respect to mobile terminals. Thus, they receive a larger amount of interference from the DVB-T transmitter. For the same reason, in study case 1 only the downlink of the mobile network is considered, as the mobile BSs are positioned on rooftops, and thus they generate a higher amount of interference on the DVB-T receivers when compared to mobile terminals.

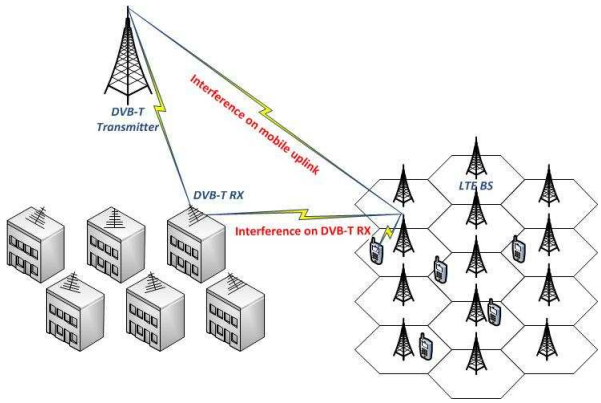

Figure 5.1: Coexistence scenario between DVB-T and LTE systems.

5.1.2.1 Mobile System

The simulation parameters of the LTE network are summarized in Table 5.1. In particular, the following assumptions hold:

- the mobile system works with a 5 MHz channel, as in this case the whole BS transmitted power is inside the transfer function of the victim DVB-T receiver[3]. Therefore, in study case 2 the interference generated on the 5 MHz LTE channel can be assimilated to AWGN, as the power spectrum of a DVB-T signal is approximately flat in its 8 MHz bandwidth. Please note that all the parameters used in this work are in agreement with those considered in typical simulations of LTE systems [68, Chapter 19];

- in each Monte Carlo simulation, 99 BSs are deployed on the considered area according to a typical hexagonal lattice, and kept in these fixed positions for all the simulation instances. Among these BSs, only the inner 42 were considered for the performance evaluation, in order to avoid any border effect, *i.e.* taking into account those BSs which have less than 6 interfering BSs in the first tier. With reference to Figure 5.2, which shows the cellular layout, only those BSs falling inside the black square were considered[4];

- in each simulation instance, 200 User Equipments (UEs) are randomly positioned in the inner area. This number was chosen such that the overall blocking

[3]The channel bandwidth of a typical DVB-T system is 8 MHz, exception made for the US where they use 7 MHz channels.

[4]Different colors denote different reuse indexes.

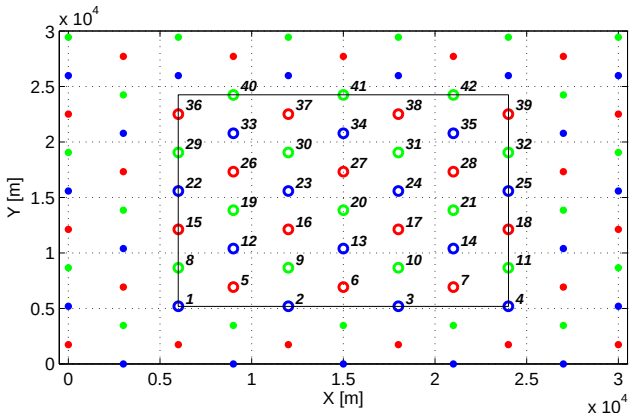

Figure 5.2: Layout of the LTE system.

percentage, *i.e.* the percentage of users in outage conditions due to internal interference only, was approximately 2%, which is a typical value;

- the Link Adaptation behaviour was simulated as a function of the SINR, which for the purpose of this work is assumed to have equivalent characteristics as the SNR, owing to the previous assumption on the AWGN-like behaviour of the interfering DVB-T signal. Among the different modulations admitted for LTE systems, only some of them were considered, and they are provided in Table 5.2. The corresponding throughput values can be found in [68].

Cell radius	2 km
Simulation area	900 km^2
Operating frequency	800 MHz
Total number of BSs	99
Number of BSs in central area	42
Cluster size	3
Channel bandwidth	5 MHz
BS antenna height	30 m
BS antenna gain	15 dBi
BS transmitted power	43 dBm
UEs per simulation instance	200
UE antenna height	1.5 m
UE antenna gain	0 dBi
UE transmitted power	23 dBm

Table 5.1: Main simulation parameters for the LTE system.

Modulation	Code Rate	SINR [dB]	Rate [bit/s/Hz]
QPSK	1/2	1.0	1.00
	2/3	2.9	1.32
16-QAM	1/2	6.6	2.00
	2/3	10.0	2.62
64-QAM	2/3	13.8	4.00
	3/4	15.7	4.47

Table 5.2: LTE throughput as a function of uplink SINR for a 5 MHz channel.

5.1.2.2 DVB-T System

The simulation parameters for the DVB-T system are provided in Table 5.3, where different DVB-T transmitter configurations are considered, depending on its height and Emitted Radiated Power (ERP). The coverage radius varies depending on the

DVB-T transmitter	
ERP	50 dBm or 70 dBm
Antenna height	100 m or 200 m
Antenna pattern	Omnidirectional in azimuth
Operational frequency	800 MHz
DVB-T receiver	
Antenna height	10 m
Antenna pattern	Mask taken from [69]
Antenna gain	14.15 dBi
Receiver minimum SINR	21 dB
Noise figure	7 dB
Noise equivalent bandwidth	8 MHz
Number of TV receivers per instance	200

Table 5.3: Main simulation parameters for the DVB-T system.

configuration being analyzed and it is determined according to the Reference Planning Configurations (RPCs) defined in GE06 [70], assuming:

- Location Probability (LP) equal to 95%;
- median field strength at coverage edge equal to 58.2 dBμV/m [70, Annex 3.4], corresponding to a minimum SINR equal to 21 dB. This value guarantees a 50% coverage at cell edge. In order to obtain a 95% LP at coverage edge, 9.05 dB must be added to the receiver minimum required SINR, considering a 5.5 dB standard deviation for the lognormal fading. Thus, the minimum SINR for the DVB-T receiver is given by 30.05 dB;

- in each simulation instance, the TV receiver positions are randomly generated within the DVB-T coverage area.

5.1.2.3 Propagation Model

According to the simulation parameters provided in the two above sections, for study case 1, *i.e.* interference from the LTE BSs towards the DVB-T receivers, the Extended Okumura-Hata model is used [71] assuming a urban environment. On the other hand, for study case 2, *i.e.* interference from a DVB-T transmitter towards a certain amount of LTE BSs, the ITU-R P.1546 model is applied [72].

5.2 Proposed Methodology

The proposed methodology to take into account both the interference from the mobile system towards the broadcasting system and vice versa is now described. The purpose of this methodology is to define both appropriate guard distances between the interfering systems and transmitters operational characteristics such that specific QoS requirements are met.
For study case 1, where the victim is the DVB-T system, the reduction in the coverage percentage was chosen as the performance metric. In particular, the interference analysis is performed according to the following steps:

1. select the DVB-T parameters, *e.g.* ERP, transmitter height, etc.;
2. define a maximum level of admitted outage due to LTE interfering BSs. In this work, this value was set equal to 1%;
3. deploy the DVB-T and LTE systems according to a predefined distance. In particular, the distance between the DVB-T coverage edge and the center of the LTE network is considered;
4. compute the overall interference generated by the LTE BSs falling inside the simulation area (the black square in Figure 5.2) for several distances between the two systems;
5. identify as *guard distance* the minimum distance between the two systems such that an outage of 1% or less is introduced in the DVB-T service;
6. repeat steps 1-5 for all the DVB-T configuration parameters that have to be evaluated.

Once the two systems are deployed according to the guard distance computed with the above procedure, the effect of the DVB-T transmitter on the LTE performance shall be evaluated. This can be done according to several performance metrics. For instance, the percentage of users that are able to access a certain modulation type (which is a function of the SINR, as stated in Section 5.1.2.1) might be considered. Please note that the interference level in this case is given by both the interference from the DVB-T transmitter and the internal interference of the LTE system, while in study case 1 there is no internal interference[5].

The above procedure is applied when there is a DVB-T system already providing service, and an LTE network has to be deployed on an adjacent area. Basically, the LTE network is deployed at a guard distance such that specific coverage requirements are met for the DVB-T service, and if the interference of digital TV towards the LTE service is also acceptable, the deployment can proceed. On the other hand, if the interference is far too high, the LTE network will have to be deployed at a greater distance (or even not deployed at all). However, the opposite situation might happen (study case 2): if a DVB-T system has to be deployed on an area adjacent to an already existing LTE network, which requirements shall be met in order to preserve an acceptable mobile service performance?
The procedure is the same as for study case 1: for several distances between the two systems and for several configurations of the DVB-T transmitter, the LTE performance deterioration is evaluated. It is important to highlight that, in this case, the distance between the two systems is given by the distance between the center of the LTE network and the DVB-T transmitter, as there is no interest in the DVB-T coverage radius. In this case, the throughput reduction perceived by the users was chosen as performance metric. In particular, the reduction in the total throughput that the BSs are able to provide to the users when there is interference from the DVB-T transmitter is evaluated, and if it is under a certain percentage it means that the interference level introduced by the DVB-T transmitter is excessive.

5.3 Numerical Results

In this section, the numerical results obtained for both study cases according to the methodology described above are provided. In particular, the results are obtained through Monte Carlo simulations performed with 100 instances.

[5]Thanks to the OFDM properties, efficient iso-frequential broadcasting systems are allowed.

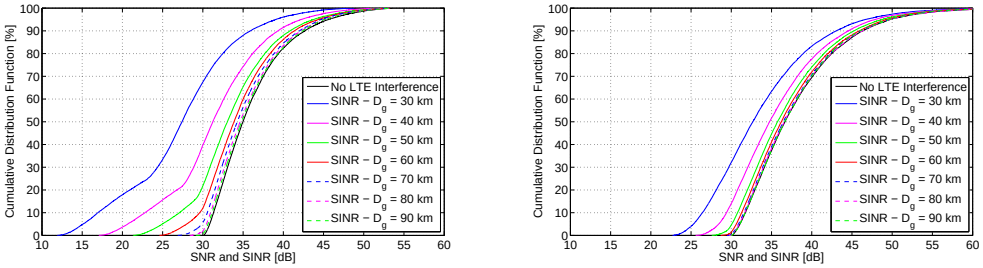

(a) ERP = 50 dBm

(b) ERP = 70 dBm

Figure 5.3: Service percentage of the DVB-T system with the transmitter mounted at $h_{TX} = 100$ m.

5.3.1 Study Case 1

The coverage reduction of the DVB-T service is evaluated thanks to the CDF of the SINR. As stated in Section 5.1.2.2, for a Location Probability equal to 95% the minimum SINR value for a correct reception is 30.05 dB. Thus, for each simulation the CDF of the SINR is computed, and the percentage corresponding to 30.05 dB is compared to that evaluated without interference. This provides the coverage reduction due to the LTE interfering BSs.

Figures 5.3-5.4 show the CDF for a DVB-T transmitter deployed at 100 m or 200 m height and transmitting with ERP $= 50, 70$ dBm. The distances reported on these figures are the distances between the DVB-T coverage edge and the center of the LTE network. It can be noticed that, by increasing the distance between the two systems, the performance of the DVB-T service improves, as expected. In particular, the CDF is quite fast in tending to the no interference case for increasing distances. Furthermore, the the DVB-T transmitter height deeply affects the coverage reduction. Actually, for a fixed link distance, transmitting from a higher location significantly increases the received field strength value, and thus the effect of the LTE interference is much less evident. For instance, by comparing Figure 5.3(b) with Figure 5.4(b), and considering the 50th percentile and a distance equal to 30 km, the difference with the no interference case is given respectively by 6 and 3 dB. The percentages of coverage reduction for the DVB-T configurations taken into account are summarized in Table 5.4, where the cases in which the 1% limit degradation is respected are highlighted. According to the definition provided in the previous sections, the guard distance for a specific DVB-T configuration is given by the minimum of these allowed distances. Depending on the DVB-T transmitter height and

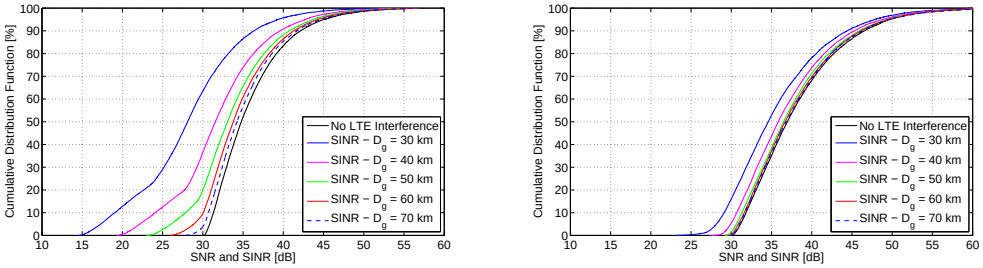

(a) ERP = 50 dBm (b) ERP = 70 dBm

Figure 5.4: Service percentage of the DVB-T system with the transmitter mounted at $h_{TX} = 200$ m.

ERP, different guard distances are required. In particular, this value decreases for higher transmitting antenna heights or higher ERP values. Thus, as expected, the worst case from the DVB-T point of view corresponds to lower transmission power or height. In conclusion, a high power DVB-T transmitter is reasonably well protected from the interference generated by a mobile system, whereas a gap-filler might need a higher degree of protection. Please note that, of course, other limit degradation thresholds would have led to different guard distances.

DVB-T configuration		**Distance [km]**						
Height [m]	**ERP [dBm]**	**30**	**40**	**50**	**60**	**70**	**80**	**90**
100	**50**	22.52	8.93	3.30	1.25	0.48	0.20	0.09
	70	4.39	1.31	0.44	0.18	0.08	0.04	0.02
Height [m]	**ERP [dBm]**	**30**	**40**	**50**	**60**	**70**	**80**	**90**
200	**50**	18.73	7.05	2.57	0.92	0.35	0.16	0.05
	70	1.58	0.49	0.18	0.08	0.04	0.02	0.00

Table 5.4: Percentage of DVB-T coverage reduction.

As stated in the previous section, once the DVB-T service is well protected, its effect on the adjacent LTE service shall be evaluated. This effect can be evaluated in terms of the percentage of mobile users that are able to access a certain modulation type, as it is a function of the SINR. The interference originated by the DVB-T transmitter is computed using the Recommendation ITU-R P.1546 [72], considering the interference at both 50% and 1% of time[6]. The results of this analysis are provided in Figure 5.5 as histograms. As expected, worst cases are obtained for higher

[6]Lower values of this percentage correspond to received field strength which are less likely to happen, and thus to higher interference scenarios.

DVB-T ERP and antenna heights, as this casues the reduction of the guard distance which guarantees the protection of the digital TV broadcasting. Furthermore, the performance are worse for interference evaluated at 1% of time, as it corresponds to lower attenuation values in the propagation model. As a matter of facts, the performance degradation is quite evident for ERP = 70 dBm, while with ERP = 50 dBm the impact on the LTE system is lower. In this case, and especially with interference evaluated at 50% of time, the interference introduced by the DVB-T transmitter is negligible with respect to the internal interference of the LTE network.

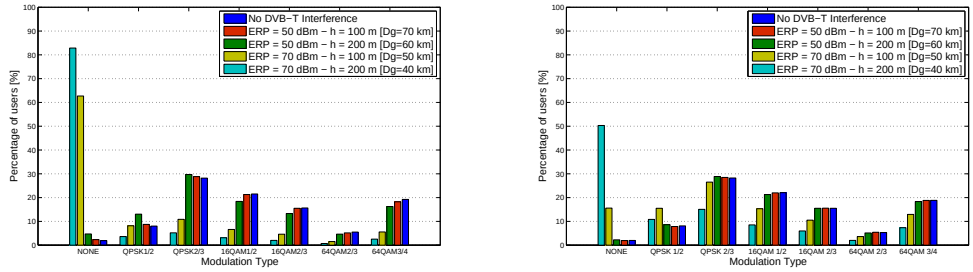

(a) Interference at 1% (b) Interference at 50%

Figure 5.5: Mobile service performance with DVB-T interference.

5.3.2 Study Case 2

For study case 2, when the pre-existing service is the LTE and a DVB-T system has to be deployed on an adjacent area, the procedure to be followed is similar to study case 1 (Section 5.2). In particular, two metrics are considered: the average throughput per BS and per 5 MHz channel provided to the users. These values are computed for several distances between the two systems[7] and for different configurations of the DVB-T transmitter. Once the maximum allowed throughput reduction is defined, *e.g.* a degradation of 10% with respect to the performance without DVB-T interference, or a minimum value of throughput to be provided is known, the requirements in terms of distance or DVB-T characteristics can be easily found.

The results are shown in Figure 5.6. It can be noticed that the throughput increases for lower DVB-T ERP values and for increasing distances between the two systems, of course. As an example, if the minimum requirement is that the average throughput provided by the BSs to their users must be greater or equal to 1.5 Mbps, and

[7]Once more, it is worthwhile noting that this distance is between the DVB-T transmitter and the center of the LTE area, for study case 2.

the DVB-T shall transmit at least 50 dBm due to coverage requirements, the distance between the DVB-T transmitter and the LTE network shall be approximately greater than 50 km.

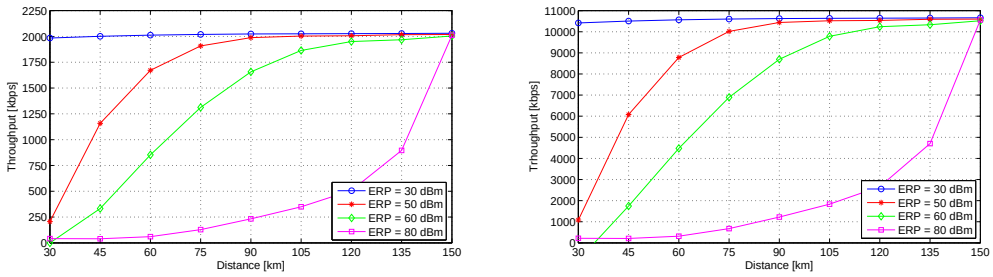

(a) Throughput per BS

(b) Throughput per 5 MHz channel

Figure 5.6: Average throughput per BS (a) and per 5 MHz channel (b) as a function of the distance, with $h_{TX} = 200$ m and interference at 1% of time.

5.3.3 Cumulative Effect of the BSs

In the previous sections, the impact of a LTE network deployed on an area adjacent to a digital TV broadcasting service was analyzed (study case 1). All the results were obtained considering 99 BSs, and in order to avoid any border effect only the inner 42 were considered. However, the potential impact of the cumulative effect of the interference from the mobile service is not negligible, and shall be properly taken into account. In order to do so, the behaviour of the guard distance for varying number of BSs in the LTE network, while keeping all the other parameters fixed, was analyzed. In particular, the DVB-T transmitter is mounted at 200 m height and transmits a 60 dBm ERP. The results of the Monte Carlo simulation are provided in Table 5.5. It is straightforward to notice that the cumulative effect is not negligible. For instance, the minimum distance between the two systems is 30 km with 4 BSs, while it raises to 50 km when considering 42 BSs: a significantly higher value.

LTE configuration	**Distance [km]**					
Number of BSs	**5**	**10**	**20**	**30**	**40**	**50**
4	22.92	10.04	1.91	0.45	0.14	0.96
9	37.15	19.92	4.58	1.11	0.35	0.12
25	65.22	43.05	13.99	3.82	1.19	0.41
42	81.44	59.50	23.78	7.35	2.29	0.76

Table 5.5: DVB-T coverage reduction as a function of the number of BSs.

5.4 Advantages of the 800 MHz Band

The introduction of broadband wireless services in the Digital Dividend band poses new coexistence and mutual interference challenges between DVB-T and 4G systems. In the previous sections, a thorough analysis of this coexistence considering a LTE broadband service was provided, with interesting simulation results. In particular, it was shown that the DVB-T system is more protected when a high power transmitter is considered, but this particularly affects the performance of the LTE service. On the other hand, low power DVB-T transmitters, like a gap-filler, introduce less interference in the LTE network, but the DVB-T coverage area is significantly reduced. Thus the coexistence between these two services requires a deep and exhaustive coordination, either at national level, or between neighbouring countries. At this point, a question naturally arises: why is this band so attractive for mobile service providers? The purpose of this section is to investigate such aspect.

5.4.1 Coverage and Propagation Analysis

In order to highlight the possible benefits of lower frequency bands with respect to higher ones for broadband mobile services, both in terms of indoor and outdoor environments, different mobile architectures and layouts were compared. In particular, the following analysis was performed taking into account the IMT bands, namely the 800 MHz, 2100 MHz, and 2600 MHz bands.

5.4.1.1 Isolated Cell Scenario

Before considering more complex and real scenarios, a simple isolated single-cell scenario is taken into account, in order to evaluate the expected gain in terms of coverage area following from the usage of the 800 MHz band instead of the 2100 MHz one. For this analysis, the coverage radius for outdoor and indoor environments is evaluated with the transmitters at both frequencies employing an omnidirectional antenna and the same transmitted power. Furthermore, the sensitivity levels and standard deviations for the shadowing margin are provided in Table 5.6.
The results of this analysis are depicted in Figure 5.7, where the coverage radius and

Sensitivity [dBm]	**QPSK 1/3 [dBm]**	**64-QAM 3/4 [dBm]**	σ_{out} **[dB]**	σ_{in} **[dB]**
−108	−100	−80	4	10

Table 5.6: Sensitivity levels and standard deviation for the shadowing margin.

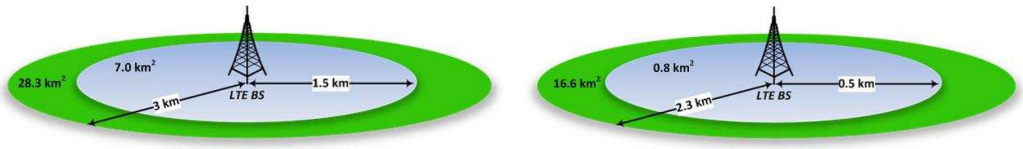

(a) Outdoor (b) Indoor

Figure 5.7: Cell radius of a LTE BS at 800 MHz and 2100 MHz.

the corresponding area at both 800 MHz and 2100 MHz are represented assuming a sensitivity level of −108 dBm. The Location Probability for the outdoor environment was set to 95%, while in the indoor case it was set to 75%. As expected, lower operating frequencies increase the coverage radius. In particular the ratio of the radius in the two cases is given by:

$$R_{out} = \frac{R_{800,out}}{R_{2100,out}} = 4.6$$
$$R_{in} = \frac{R_{800,in}}{R_{2100,in}} = 2$$

It can be noticed that, for the outdoor environment, the radius is doubled by using the 800 MHz band, while for the indoor scenario the benefit is even stronger, with a factor of 4.6. This reflects in a significant increase in the covered area at 800 MHz. Such an advantage might be exploited by the mobile operator through appropriate network planning, as reducing the number of BSs maintaining the same transmission power, or decreasing power while keeping the same number of BSs.

5.4.2 Hexagonal and Real Scenarios

The above depicted single-cell scenario allows some first considerations on the benefit of using the 800 MHz band instead of higher ones. However, it is a far too simple scenario as it does not take into account the internal interference of the mobile system, which, of course, would be higher maintaining the same number of BSs while using lower frequencies. In order to properly analyse this effect, some coverage simulations were performed at 800 MHz, 2100 MHz, and 2600 MHz considering both an hexagonal lattice and a real BSs deployment in the city of Bologna (Italy).

Material	800 MHz	2100 MHz	2600 MHz
Brick	13.9 dB	27.7 dB	31.1 dB
Concrete	24.7 dB	29.7 dB	30.3 dB

Table 5.7: Penetration loss values at 800 MHz, 2100 MHz, and 2600 MHz.

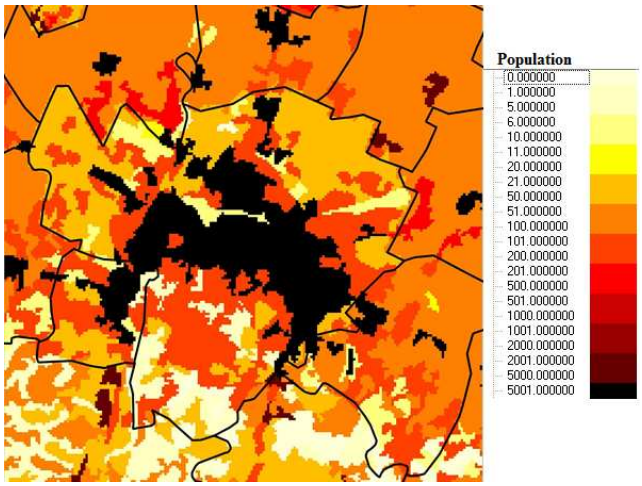

Figure 5.8: Population data in Bologna.

5.4.2.1 Ideal Layout

This layout was realized using the same simulator as for the coexistence analysis provided in the previous sections. In particular, as the considered area (located in the city center) is a square of 529 km^2, a similar hexagonal layout to that provided in Figure 5.2, assuming a a 1.55 km radius, was repeated (as the covered area is lower than 529 km^2) and properly overlapped to the city map. The purpose of this overlapping process is to obtain results on the covered population, which, of course, is a critical parameter for mobile operators. As for the coexistence analysis, only the inner BSs were taken into account in order to avoid any border effect. Also in this case, the propagation model for the mobile network is the Extended Okumura-Hata model [71]. The population distribution in the considered area is provided in Figure 5.8. Moreover, for the indoor environment both concrete and brick walls were considered, and the penetration loss values are summarized in Table 5.7 [73]. The simulation results for the covered population in the ideal layout are provided in Table 5.8. The benefits deriving from the usage of the 800 MHz band are evident, especially for the 64-QAM modulation and the indoor scenarios. As a matter of facts, for the -108 dBm sensitivity and the QPSK modulation cases the outdoor coverage is already satisfactory for both 2600 MHz and 2100 MHz, and the improvement at 800 MHz is limited to just a few percentiles. On the other hand, considering a 64-QAM modulation, a $40\% - 50\%$ increase is obtained, which is a significant gain. Furthermore, in the indoor environments, the gain is impressive: for instance, in the -108 dBm sensitivity case, passing from 2600 MHz to 800 MHz provides a 70%

increase in the covered population, while from 2100 MHz to 800 MHz the increase is approximately 50%.

Band	Scenario	Sensitivity -108 dBm	QPSK 1/3	64-QAM 3/4
2600 MHz	**Outdoor**	98.20%	91.26%	34.98%
	Indoor - brick	27.78%	12.25%	1.00%
	Indoor - concrete	29.79%	13.39%	1.10%
2100 MHz	**Outdoor**	99.34%	95.82%	48.03%
	Indoor - brick	49.44%	26.56%	2.60%
	Indoor - concrete	43.16%	21.90%	1.99%
800 MHz	**Outdoor**	99.99%	99.86%	87.07%
	Indoor - brick	98.76%	94.07%	46.93%
	Indoor - concrete	90.74%	74.56%	18.70%

Table 5.8: Population coverage with ideal hexagonal layout.

5.4.2.2 Real Layout

In this scenario, the same coverage analysis as for the hexagonal layout was performed considering a real UMTS cellular layout. The distribution of the 96 UMTS BSs was provided by ARPA (Agenzia Regionale per la Protezione dell'Ambiente dell'Emilia Romagna), and is shown in Figure 5.9. The simulations results are summarized in Table 5.9. It can be noticed that the real scenario provides better

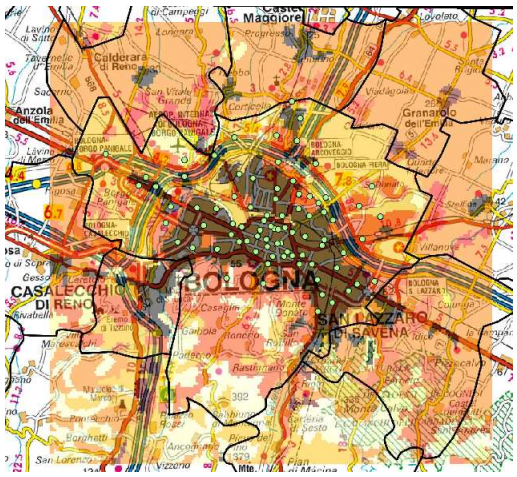

Figure 5.9: UMTS cellular layout in Bologna.

performance with respect to the ideal one, and this is due to the different coverage strategies of densely populated areas. As a matter of facts, while in the hexagonal

layout each BS covers a certain area independently from the population density, in the real case more BSs are deployed in more densely populated areas. However, with a more appropriate network planning as in the real scenario, the advantage in using the 800 MHz band instead of 2600 MHz and 2100 MHz is impressive. For instance, in the outdoor environment with 64-QAM modulation, the covered population increases of $30\% - 20\%$ for 2600 MHz and 2100 MHz respectively, while with QPSK modulation this gain raises to $50\% - 40\%$.

Band	Scenario	Sensitivity -108 dBm	QPSK 1/3	64-QAM 3/4
2600 MHz	**Outdoor**	97.36%	93.66%	68.75%
	Indoor - brick	61.11%	41.86%	8.58%
	Indoor - concrete	62.89%	43.78%	9.22%
2100 MHz	**Outdoor**	98.51%	95.81%	76.59%
	Indoor - brick	76.20%	59.97%	16.81%
	Indoor - concrete	72.58%	55.18%	14.06%
800 MHz	**Outdoor**	99.89%	99.41%	92.02%
	Indoor - brick	98.15%	95.24%	74.81%
	Indoor - concrete	93.73%	87.44%	51.37%

Table 5.9: Population coverage with real layout.

5.4.3 Real Layout in Digital Divide Areas

According to the results obtained in the above sections, the deployment of wireless services in frequency bands below 1 GHz provides significant advantages, due to the better propagation characteristics at lower frequencies. On the one hand, this advantage might be used to increase indoor coverage in densely populated areas, or to reduce the number of deployed BSs. On the other hand, such an increase in coverage area can be exploited to provide broadband wireless connectivity in rural areas, where significant percentages of the populations do not have access to either the fixed and the wireless broadband services, which are the so called *Digital Divide* areas. In this section, an investigation of the reduction of the Digital Divide areas in the Emilia Romagna region is provided, analyzing as above the consequences of the switch from present 2100 MHz UMTS BSs to 800 MHz ones.
Starting from the information on the UMTS BSs distribution, only those in Digital Divide areas were taken into account. Assuming the same transmission parameters for both frequency bands, the coverage performance was evaluated for the 384 kbps data service. The simulation results are provided in Figure 5.10. The covered areas

in the 2100 MHz case are shown in blue, while those covered at 800 MHz are colored in green. It can be noticed that the gain deriving from the usage of the 800 MHz band is impressive in rural areas as well.

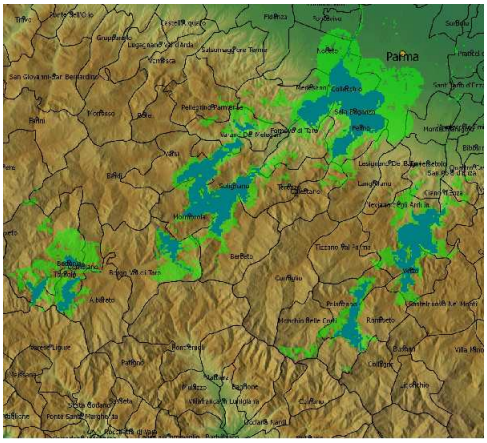

Figure 5.10: Coverage at 2100 MHz and 800 MHz in Digital Divide areas.

Chapter 6

CEPT SE43 Regulation for Cognitive Radio Systems

As part of its Digital Dividend strategy in the 470-790 MHz band, the European Communications Committee (ECC) aims at highly efficient and flexible spectrum usage, while allowing the widest possible range of technologies. With this intent, ECC delegated to CEPT a study on Cognitive Radios, aiming at providing technical and operational requirements for CR systems in the Digital Dividend band, in order to both increase spectrum usage efficiency and protect primary services. This led to the creation of the Spectrum Engineering (SE) 43 working group in 2009, whose objectives are[1]: (i) the definition of technical and operational requirements for the operation of CR systems in the *white spaces*[2] of the UHF broadcasting band (*i.e.* the Digital Dividend band) to ensure the protection of primary radio services/systems and investigate the consequential amount of spectrum potentially available; (ii) provide technical assistance on further issues related to white spaces and CR systems that ECC may identify in the future; and (iii) liaise directly with relevant groups within ECC and ETSI as necessary. SE43 activities were concluded in 2010, with the publication of the ECC Report 159 [75]. However, this group is still working on the above listed topics in an idle state inside CEPT working groups.
In [75], SE43 addresses several protection criteria, developed using both measure-

[1] SE43 terms of reference are available on http://www.ero.dk/.

[2] According to CEPT [74], the term white space denotes *a part of the spectrum which is available for a radiocommunication application/service/system at a given time in a given geographical area on a non-interfering / non-protected basis with regard to other services with a higher priority on a national basis.*

ment results and previous ECC, ETSI and ITU deliverables, for each of the primary systems taken into account: broadcasting, Programme Making and Special Events (PMSE), Radio Astronomy, Aeronautical Radionavigation, Mobile/Fixed services adjacent to the 470-790 MHz band. In particular, three cognitive techniques were initially taken into account, *i.e.* single-device sensing, geolocation database, and beacon. However, most of the efforts were devoted to the former two.
Thanks to the participation to SE43 as Italian Administration representative, the following studies were performed: (i) quantification of the amount of spectrum potentially available as white space [11]; (ii) analysis of the issues related to geolocation databases and their possible combination with spectrum sensing [15–17]; (iii) calculation of the Hidden Node margin in a typical Italian scenario [12, 13]; (iv) performance evaluation of a simple cooperative energy detection sensing algorithm [18,19]; (v) coexistence analysis between cognitive devices and Terrestrial Trunked Radio (TETRA) systems [20]. For the sake of briefness, in this chapter only topics (i) and (iii) will be discussed.

6.1 Amount of White Spaces in West Piedmont

In this section, an estimation of the spectrum potentially available as white space in West Piedmont (Italy), where the digital switch-over process was completed at the end of 2009, is provided. Such estimation depends on several factors, as the characteristics of the cognitive devices, the topology of the considered area, the national rules governing the use of channels adjacent to those used by DVB-T services, and many others. As some of these factors still have to be defined by national or international regulatory bodies, a possible approach to estimate the amount of white space is to make several hypothesis whenever needed.
However, in order to keep the estimation process as general as possible, a simple detection threshold-based approach was proposed: assuming that the CR can rely on non-cooperative spectrum monitoring techniques only, it can measure the received signal power on a certain channel, and if this power is under a properly chosen detection threshold it can deduce that there are no licensed users in its proximity, and thus it can transmit its intended signal according to specific emission requirements. It is worthwhile underlining that the results provided by this approach *do not* show the spectrum that is actually available as white space for two reasons:

- the interference generated by the cognitive device on the primary users when it

starts its transmission shall be taken into account. Not considering this effect results in a potential overestimation of the available spectrum;

- geolocation databases or cooperative spectrum monitoring techniques might allow the cognitive device to use higher detection thresholds, which might introduce an underestimation error.

6.1.1 Methodology

In this section, the methodology employed to determine the amount of spectrum potentially available as white space in Italy is described. As stated in the above paragraph, it is a detection threshold-based approach, and it is performed according to the following steps:

1. compute the power received on a given channel and in a given pixel (600 m × 600 m) by a receiving antenna mounted at a specific height above ground level. This antenna is assumed to be omnidirectional with a 0 dBi gain. By using database information containing ERP values and positions of each DVB-T transmitter covering West Piedmont, this computation is performed applying the ITU-R Recommendation P.1546 [72];
2. compare the received power with a properly defined detection threshold;
3. if the received power is lower than the detection threshold, the channel is considered as vacant;
4. iterate steps 1-3 for all the channels in the 470-790 MHz (*i.e.* channel from 21 to 60) and for all the pixels which describe the considered area.

As at the time of this analysis only some of the Italian regions completed the digital switch-over process, *i.e.* Lazio, Sardinia, Aosta Valley, Campania, and West Piedmont, the above depicted procedure was applied to the latter region, which is shown in Figure 6.1.
It should be noted that PMSE devices were not considered in this study. Furthermore, in Italy some channels were already assigned to the Digital Dividend, which will start as soon as the switch-over process is completed. In regions like West Piedmont where this process was already completed, DVB-T services were not allowed to use these frequencies anymore, so at the moment of the study they should have resulted as vacant. However, as neighbouring regions were not all digital yet, transmitters covering these areas were still using the Digital Dividend channels, and thus

Figure 6.1: West Piedmont map.

simulations show them as occupied (with low signal levels) even if they should not be such.

6.1.2 Numerical Results

In this section, the simulation results are provided with the detection threshold (DT) set to -114 dBm and -120 dBm. These two values were chosen in accordance with the guidelines provided by FCC and UK Ofcom at the time of the study. Moreover, the receiving antenna was mounted at 1.5 m, 10 m and 30 m.

Figures 6.2-6.4 show the amount of channels potentially available for each pixel. Referring to Figure 6.1, which shows the topography of the analyzed area, it can be easily noticed that the areas where the cognitive devices actually have channels to operate on are mainly rural, in correspondence of mountains and valleys. More populated areas, near big cities like Turin or Cuneo, have little or no spectrum available. This is a consequence of the Italian DVB-T deployment, as the 470-790 MHz band is heavily used by broadcasting services, making it difficult to actually find some potential white spaces. Furthermore, it can be also noticed that the spectrum potentially available is deeply dependent on the considered detection threshold. As a matter of facts, with DT= -120 dBm at 1.5 m the percentage of pixels where there is at least 1 available channel is approximately 47%, while raising DT to -114 dBm increases this percentage to more than 55%.

As previously stated, the results provided in this section probably do not represent the exact amount of spectrum available as white space. Actually, they are most likely an overestimation, because even if a cognitive device detects a channel as va-

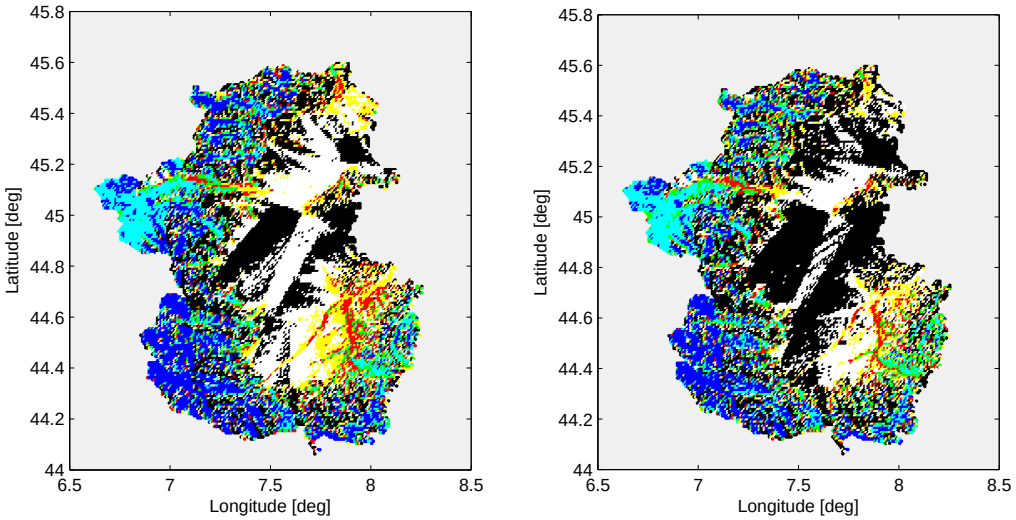

(a) Threshold = -114 dBm

(b) Threshold = -120 dBm

Figure 6.2: Channels potentially available as white space in West Piedmont with receiving antennas at 1.5 m. Black: 0, white: 1-2, yellow: 3-5, red: 6-10, green: 11-20, cyan: 21-30, blue: 31-40.

cant, it might not be allowed to use it due to interference issues. In particular:

- the cognitive device might generate harmful interference on an adjacent channel which is occupied;
- the interference generated by all the cognitive devices detecting a channel as available might be too high on an adjacent channel in the same pixel or on the same channel in adjacent pixels, or both;
- even if the hidden node problem is taken into account through a margin within the detection threshold, situations might still occur where the cognitive device experiences a shadowing higher than the margin itself, thus performing an erroneous spectrum monitoring.

However, cooperation among the cognitive devices or the implementation of a sensing technique combined with the information provided by a geolocation database might allow them to use a higher detection threshold, thus counter-balancing or even overwhelming the reduction of available channels due to the above listed interference issues. For instance, if the gain due to cooperation was 15 dBm (DT= -105

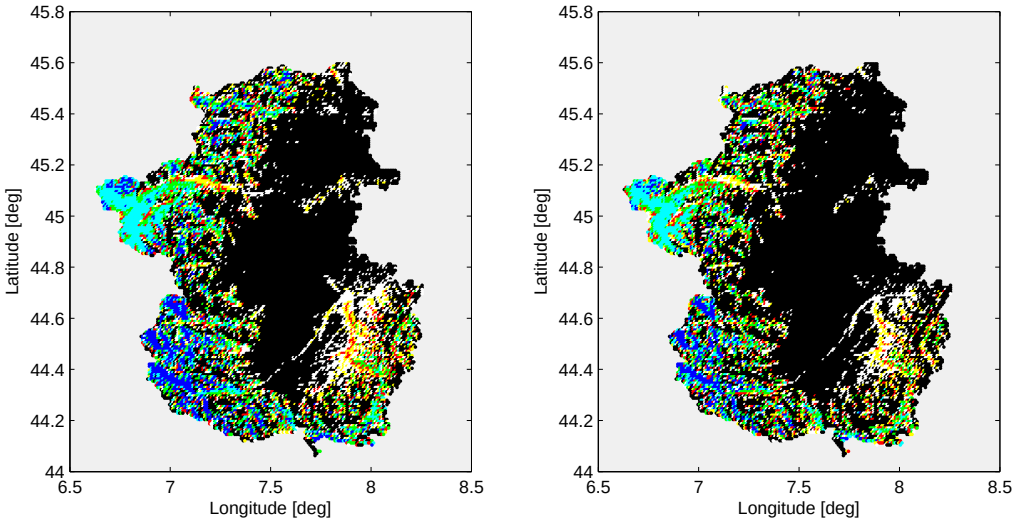

(a) Threshold = -114 dBm (b) Threshold = -120 dBm

Figure 6.3: Channels potentially available as white space in West Piedmont with receiving antennas at 10 m. Black: 0, white: 1-2, yellow: 3-5, red: 6-10, green: 11-20, cyan: 21-30, blue: 31-40.

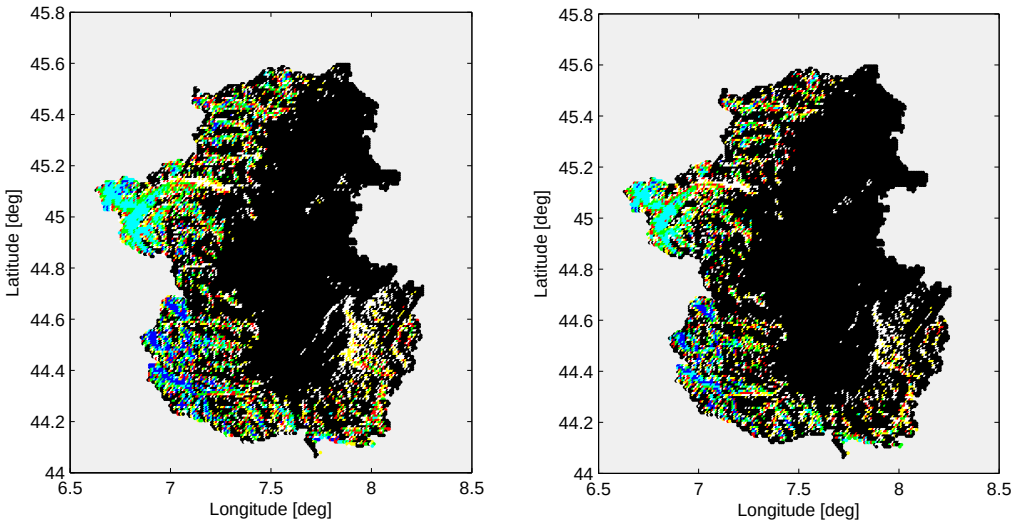

(a) Threshold = -114 dBm (b) Threshold = -120 dBm

Figure 6.4: Channels potentially available as white space in West Piedmont with receiving antennas at 30 m. Black: 0, white: 1-2, yellow: 3-5, red: 6-10, green: 11-20, cyan: 21-30, blue: 31-40.

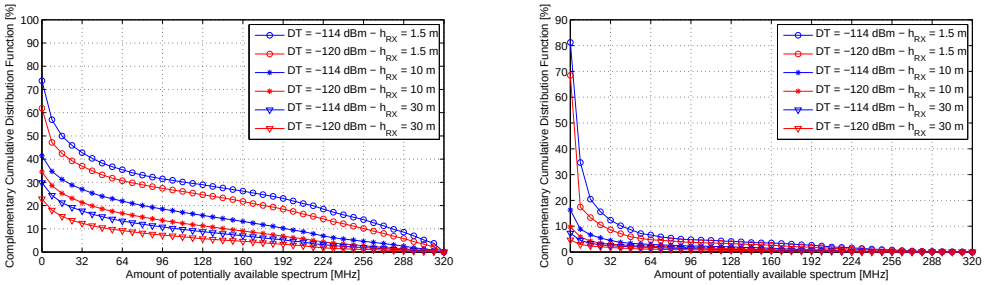

(a) Location (b) Population

Figure 6.5: Amount of spectrum potentially available as white space per location (a) and population (b) in West Piedmont.

dBm), the percentage of pixels where there is at least 1 available channel would become approximately 77%.

Figure 6.5 shows the CCDF of the estimated amount of available spectrum, in terms of both the percentage of locations (pixels) and population. These two plots actually confirm the point that the areas where there are more available channels are mainly rural, as the CCDF referring to the population percentage is extremely fast in going to values under $5-10\%$, while the CCDF referring to the location percentage has a smoother slope. For instance, while nearly 20% of locations have more than 64 MHz available with DT$= -120$ dBm at 10 m, only 2% of the population would actually have the possibility to exploit such opportunity.

6.2 Analysis of the Hidden Node Problem

In order to avoid harmful interference towards primary services, CRs must be able to identify the vacant channels. To this aim, they can be assisted by several cognitive techniques, as described in Appendix C. When using a single-device spectrum monitoring approach, there are several technological challenges to be overcome. In this section, the Hidden Node problem for cognitive radio systems is addressed in real environments.

6.2.1 Problem Statement

Most of the single-device spectrum monitoring techniques rely on the power estimated at the CR in order to decide whether a certain channel is available or not. However, according to this paradigm, the following situation might occur, as de-

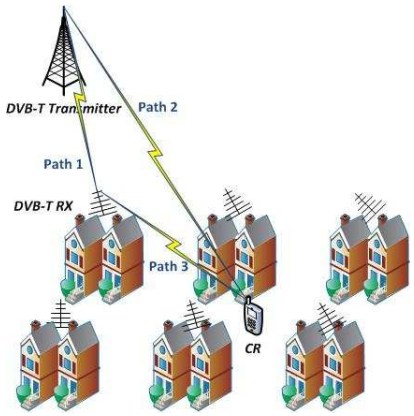

Figure 6.6: Hidden Node problem.

picted in Figure 6.6:

- a DVB-T receiving antenna receives the intended signal using a rooftop directional Yagi antenna mounted clear of surrounding objects (path 1);

- a nearby cognitive device attempts to detect the primary signal at street level, but it is blocked by surrounding buildings (path 2), and thus it might receive a significantly lower signal level;

- the cognitive device, performing a single-device spectrum sensing algorithm, might erroneously identify the specific channel as vacant, and thus transmit causing harmful interference towards the primary DVB-T receiver (path 3).

In order to take into account this effect when using single-device monitoring techniques, the detection threshold has to be properly set. In particular, an additional margin, called *Hidden Node Margin* (HNM), representing the estimate of the difference in signal level that might be caused by the hidden node problem, shall be added to the threshold.
In [75], the HNM is defined as the difference between field strength levels received at the location of the cognitive device and the DVB-T receiving antenna, taking into account the statistical distribution of these signals. This margin depends on several parameters, such as the DVB-T reception mode (*e.g.* fixed rooftop, portable indoor, portable outdoor, mobile TV) and the environment (*e.g.* urban, rural, etc.). In this work, the focus will be on the fixed rooftop reception.

6.2.2 Hidden Node Margin Estimation

The HNM can be evaluated according to two possible approaches, by applying either a deterministic or a statistical propagation model. Furthermore, experimental measurements might be used to validate the simulation results.

6.2.2.1 Deterministic Approach

This methodology is based on ray tracing simulations performed in several environments. The Hidden Node Margin is calculated as the difference between field strength values at the DVB-T receiving antenna and at the CR for several heights. Simulations provide statistics for the HNM values, which are then employed to obtain the desired protection of the DVB-T service, typically 99% or 99.9%. This approach was performed by using a sophisticated ray tracing tool developed by the University of Bologna [76, 77], and applied to real scenarios in the city of Bologna. In particular, several areas were considered in order to identify the dependence of this margin on topological parameters, as the building density and the street width.

6.2.2.2 Statistical Approach

The second methodology is described in [75], and is based on the ITU-R Recommendation P.1546 [72]. In particular, the HNM is computed as follows:

$$\mathrm{HNM} = \mathrm{E}_{\mathrm{med,DVB-T}} - \mathrm{E}_{\mathrm{med,CR}} + \mu_{\mathrm{x}}\sigma_{\mathrm{S}} \tag{6.1}$$

where $\mathrm{E}_{\mathrm{med,DVB-T}}$ and $\mathrm{E}_{\mathrm{med,CR}}$ denote the median field strength value at the DVB-T receiving antenna and CR heights respectively, μ_x is the Gaussian location correction factor (which has to be properly determined for adequate protection of the primary service) with x being the chosen percentage of protection (*e.g.* 99% or 99.9%), and σ_{S} is the standard deviation of the lognormal fading.

6.2.2.3 Simulation Setup

As previously stated, the HNM was evaluated for DVB-T fixed reception in several areas of the city of Bologna. In particular, the three environments shown in Figure 6.7 were considered thanks to a database containing all the buildings data:

- *Dense Urban* (2165 points): a 16 km^2 square area, which includes also the city center. This area is characterized by narrow streets with radial orientation,

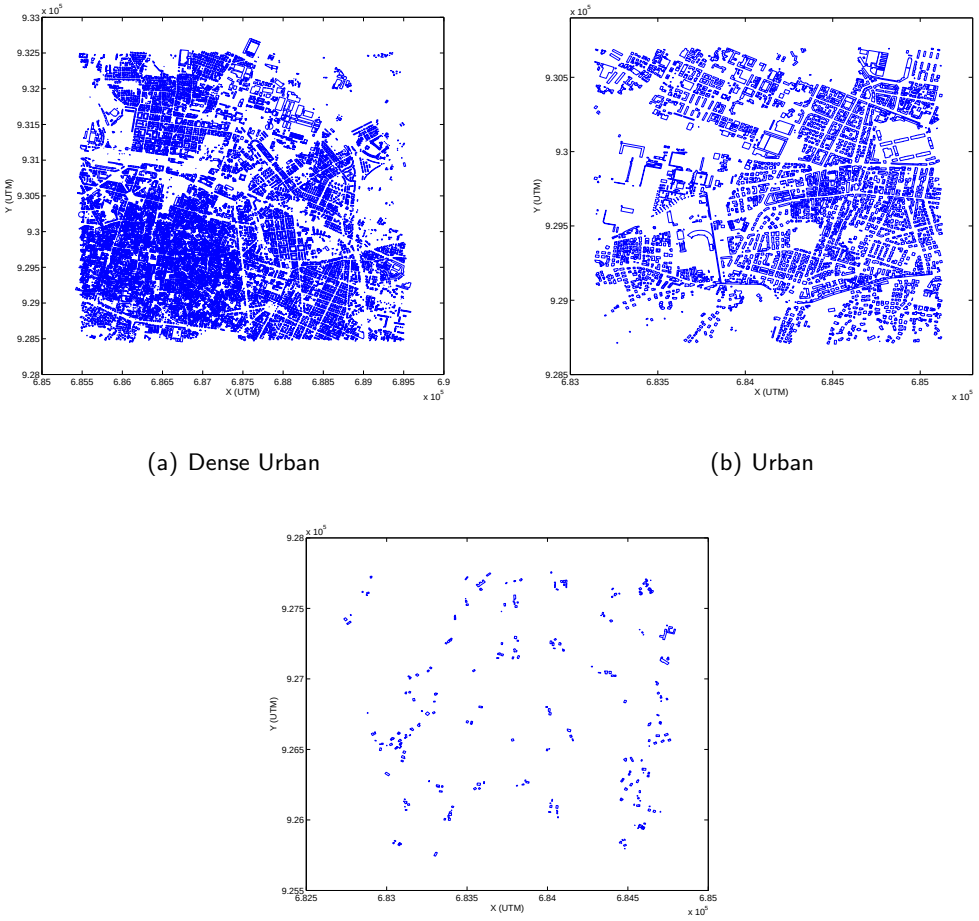

(a) Dense Urban

(b) Urban

(c) Rural Open

Figure 6.7: Analyzed areas in Bologna for the Hidden Node Margin.

and some medieval towers and churches are present. The average building height is 12.2 m;

- *Urban* (1765 points): a 4 km^2 square area, characterized by 2-6 storey high buildings with an average height of 10.5 m;

- *Rural Open* (3313 points): a km^2 square area, with houses typically 2-3 storey high and an average height of 6 m. In particular, this area is the closest to the DVB-T transmitter.

Cognitive devices were deployed at 1.5 m (street level) and 10 m in both urban and dense urban scenarios, while only at 1.5 m in the rural open one. On the other hand, the DVB-T receiveing antennas were mounted at 10 m and 30 m in all scenarios.

Frequency	690 MHz
Bandwidth	8 MHz
ERP	81.11 dBm
Height	335 m a.s.l.
Distance from simulated points	Dense Urban: 3.4-6.1 km
	Urban: 3.4-4.7 km
	Rural Open: 2.5-3.9 km

Table 6.1: DVB-T transmitter parameters.

Relative Permittivity	5
Relative Permeability	1
Conductivity	0.01 S/m

Table 6.2: Electromagnetic parameters for the ray tracing tool.

In each of the three considered environments, the HNM was evaluated along several outdoor paths with 1 m spaced measurement points, where in each of these points the DVB-T signal was measured at the DVB-T receiving antenna and CR heights. Furthermore, as DVB-T transmitter a real installation was considered, with parameters provided in Table 6.1.

For the deterministic approach, the ray tracing tool allows to consider diffractions, reflections, and diffuse scattering, while transmission through walls was disregarded in the employed software version [77]. Losses due to the interaction of the electromagnetic field with walls were computed assuming the electromagnetic parameters in Table 6.2, and they are the result of the validation of this software propagation tool through measurements [76]. With reference to the statistical methodology, both urban and dense urban scenarios were mapped as urban environment for the propagation analysis with ITU-R Recommendation P.1546, and the standard deviation of the lognormal fading was set to 5.5 dB as proposed in [75].

6.2.3 Numerical Results

In this section, the HNM values computed through the two methodologies introduced in the above sections are provided. It is worthwhile noting that, in some cases, these values were negative, *i.e.* the propagation conditions were more favourable for cognitive devices rather than for the DVB-T system. This was mainly due to the propagation model based on the ray tracing tool, where the coherent combination of rays corresponding to different paths actually increases the measured field strength level. These negative values of the HNM basically denote situations in which the

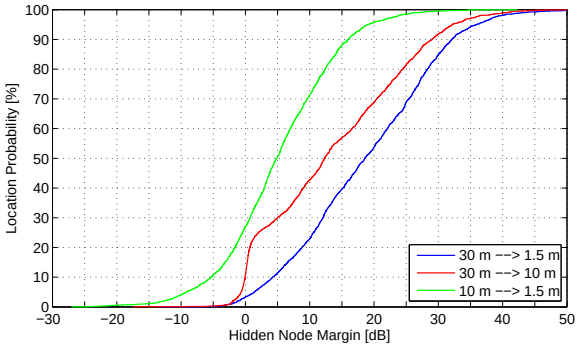

(a) CDF

Configuration DVB-T/CR	HNM at 99%	HNM at 99.9%
30 m / 1.5 m	43.38 dB	54.55 dB
10 m / 1.5 m	27.05 dB	34.80 dB
30 m / 10 m	40.36 dB	46.99 dB

(b) Values at 99% and 99.9%

Figure 6.8: Hidden Node Margin in the Dense Urban scenario.

Scenario	Configuration	Deterministic HNM [dB]	Statistical HNM [dB]
Dense Urban	30 m / 1.5 m	43.38	39.66
	10 m / 1.5 m	27.05	15.53
	30 m / 10 m	40.36	36.92
Urban	30 m / 1.5 m	40.93	39.85
	10 m / 1.5 m	32.99	18.27
	30 m / 10 m	31.30	34.36
Rural Open	10 m / 1.5 m	4.64	28.43

Table 6.3: Comparison of the HNM values with deterministic and statistical approaches for a 99% protection level of the DVB-T service.

Hidden Node problem does not occur. Thus, these cases were considered in order to obtain proper statistics, but they should be considered only as situations in which the Hidden Node problem is not present.

6.2.3.1 HNM Estimation

In Figures 6.8-6.10, the CDFs for the three analyzed environments are shown together with the values of HNM for 99% and 99.9% of protection of the DVB-T service, obtained with the deterministic methodology. In particular:

- Dense Urban (Figure 6.8): in this scenario the HNM is strongly dependent on

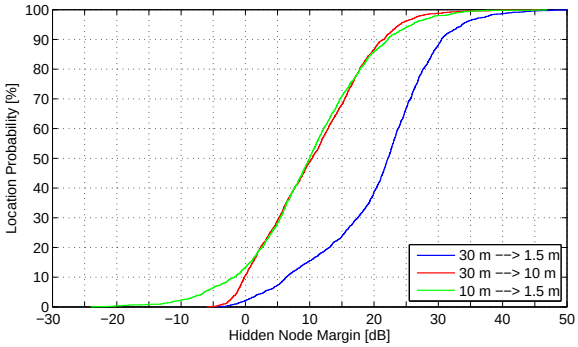

(a) CDF

Configuration DVB-T/CR	HNM at 99%	HNM at 99.9%
30 m / 1.5 m	40.93 dB	48.03 dB
10 m / 1.5 m	32.99 dB	46.44 dB
30 m / 10 m	31.30 dB	39.98 dB

(b) Values at 99% and 99.9%

Figure 6.9: Hidden Node Margin in the Urban scenario.

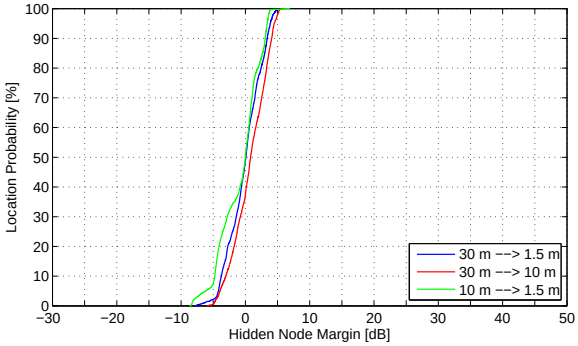

(a) CDF

Configuration DVB-T/CR	HNM at 99%	HNM at 99.9%
30 m / 1.5 m	4.64 dB	4.99 dB
10 m / 1.5 m	3.39 dB	5.06 dB
30 m / 10 m	3.08 dB	5.91 dB

(b) Values at 99% and 99.9%

Figure 6.10: Hidden Node Margin in the Rural Open scenario.

the difference between the DVB-T receiving antenna height and that of the cognitive device, and quite high values of the HNM are required, as expected.

Scenario	Configuration	Deterministic HNM [dB]	Statistical HNM [dB]
Dense Urban	30 m / 1.5 m	49.82	43.86
	10 m / 1.5 m	34.80	19.73
	30 m / 10 m	46.99	41.12
Urban	30 m / 1.5 m	48.03	44.05
	10 m / 1.5 m	46.44	22.48
	30 m / 10 m	39.98	38.57
Rural Open	10 m / 1.5 m	4.99	32.63

Table 6.4: Comparison of the HNM values with deterministic and statistical approaches for a 99.9% protection level of the DVB-T service.

It can be noticed that highest margins were obtained for the DVB-T at 30 m and the cognitive device at 1.5 m. On the other hand, lower values resulted from the deployment of the DVB-T receiver at 10 m, as this corresponds to deeper obstruction with respect to a receiving antenna at 30 m;

- Urban (Figure 6.9): in this environment, the configuration requiring higher HNM values is still the one with the DVB-T receiver deployed at 30 m and the cognitive device at street level (1.5 m), while the other two cases basically show the same behaviour. It can be noticed that as the buildings density and their mean height decrease, the margin distributions tend to be similar, as expected;

- Rural Open (Figure 6.10): in this scenario, the HNM values are very similar for all configurations, and very low as well, as the both the DVB-T receiver and the cognitive device are likely to be in Line of Sight (LOS) propagation conditions (see Figure 6.7). However, considering that this is a rural scenario, only the case with the DVB-T receiving antenna at 10 m will be considered in the following, as it is the most meaningful case. As a matter of facts, in rural areas it is unlikely to have buildings with 30 m height.

The HNM values obtained applying the statistical approach are reported in Tables 6.3-6.4 together with those obtained in the deterministic case. In the dense urban and urban scenarios, the two methodologies provide similar results in the 30 m / 1.5 m and 30 m / 10 m configurations, while more attention shall be paid in the third deployment. In the 10 m / 1.5 m configuration, the results are quite different. Consider the dense urban and urban scenarios. The ITU-R Recommendation P.1564 propagation model provides the field strength received at a default height of 30 m

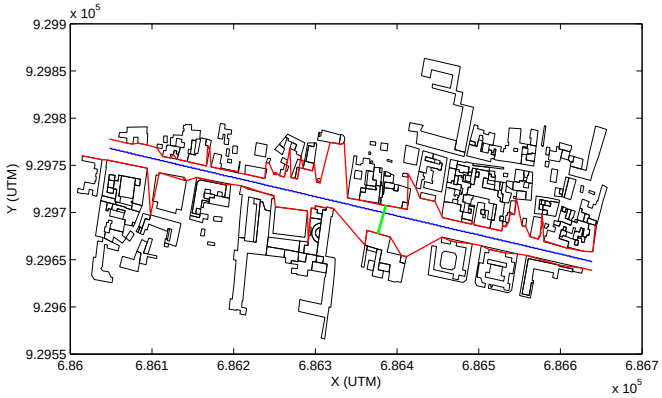

Figure 6.11: Example of road width (green line). Red and blue lines represent the modeling of the road sides and the measurement path respectively.

and 20 m respectively. Thus, when assuming the DVB-T receiving antenna at 10 m, a significant height loss margin has to be applied to the received signals. However, the deterministic approach suggests that such margin is far too large for dense urban and urban environments, which is mainly due to the actual average height of the buildings, *i.e.* 12.2 m and 10.5 m respectively. When considering the open scenario, the 1546 model assumes that the receiving antenna is at 10 m, and thus the margin loss is applied only to the cognitive device reception. Furthermore, in the open scenario taken into account, the cognitive devices were often in LOS conditions, and thus the HNM values with the deterministic approach are significantly lower than those provided by the statistical model.

6.2.3.2 Topology Parameters

The definition of HNM and the methodologies applied for its evaluation suggest that it could be considered as a height loss factor. As such, it can be characterized in terms of several topological parameters. In this section, the results of this analysis are provided taking into account the street width and the rooftop diffraction angle:

- *street width*: Figure 6.12(a) shows the linear regressions of the HNM values as a function of the street width, which for each measurement point is given by the distance between the two nearest buildings on an appropriate direction. A graphical representation on this distance is provided in Figure 6.11, while the equations of the linear regressions are provided in Table. It is worthwhile

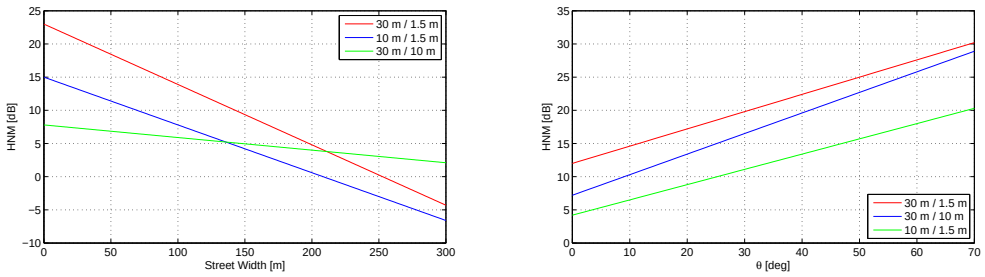

(a) Street width (b) Rooftop diffraction angle

Figure 6.12: Linear regressions of the HNM values as a function of the street width and the rooftop diffraction angle.

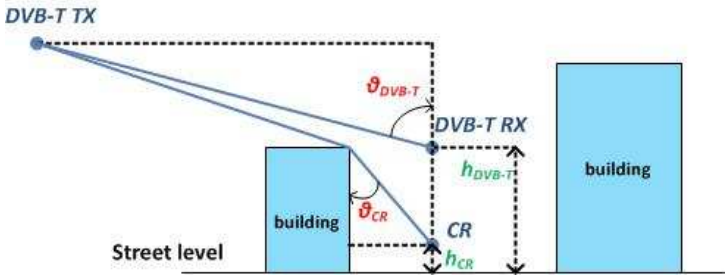

Figure 6.13: Rooftop diffraction angle.

highlighting that, due to the distance definition and to the lack of database information, also open areas (*e.g.* gardens, squares, etc.) were considered as belonging to a street, and this is reflected in the large range of street width values (0-300 m). The dependence on the street width is straightforward to be explained: as the street width increases, the propagation conditions are more favourable to the cognitive devices, and in some cases it even reaches a LOS condition, thus decreasing the difference between its received signal level and that measured at the DVB-T antenna. As a consequence, the regression lines show a steeper slope in those scenarios where a LOS condition of the cognitive device introduces the highest gain, *i.e.* dense urban and urban scenarios;

- *rooftop diffraction angle*: this angle is defined as:

$$\theta_{diff} = \theta_{DVB-T} - \theta_{CR} \tag{6.2}$$

where θ_{DVB-T} and θ_{CR} are graphically represented in Figure 6.13. As in the street width case, the regression lines of the HNM values as a function of this parameter are considered, as shown in Figure 6.12(b). It can be noticed that,

Configuration	Street width	Rooftop diffraction angle
30 m / 1.5 m	$y = -0.091x + 23$	$y = 0.26x + 12$
30 m / 10 m	$y = -0.072x + 15$	$y = 0.31x + 7.2$
10 m / 1.5 m	$y = -0.019x + 7.8$	$y = 0.23x + 4.2$

Table 6.5: Expression of the linear regressions.

considering a fixed value of θ_{DVB-T}, when θ_{diff} decreases also θ_{CR} decreases, meaning that the cognitive device gets closer to the nearby building. As a consequence, the height loss is increased, and consequently the HNM increases as well.

Chapter 7

Cognitive Hybrid Satellite-Terrestrial Systems

Satellite broadcasting and mobile satellite systems covering air and sea are well established markets. On the other hand, satellite systems have not been shown to compete with terrestrial service provision yet. Only in rural Digital Divide area the satellite is actually used for broadband wireless services, with terrestrial mobile systems controlling all the other market niches. However, as stated in the previous sections, mobile terrestrial systems are experiencing a lack of spectrum resources with consequent coverage issues, and satellite systems have one significant advantage: wide area coverage. Thus, cooperation and integration between satellite and terrestrial systems seems to be an attractive solution, leading to Hybrid Satellite-Terrestrial Systems (HSTS) [78–80].

Of course, most of the current terrestrial communications are deployed without considering the requirements for such hybrid systems. Furthermore, modifying the existing terrestrial communication systems to suit these requirements seems not to be feasible, due to both cost and technical issues. In order to cope with thee limitations, and to exploit the satellite advantages providing wider coverage, Cognitive Radio based satellite ground terminals were introduced in [14, 21]. Such systems need to integrate and coexist with other terrestrial systems by efficiently sharing frequency, time and spatial resources, leading to the concept of Cognitive Satellite Terrestrial Radios (CSTR), which are presented in this chapter.

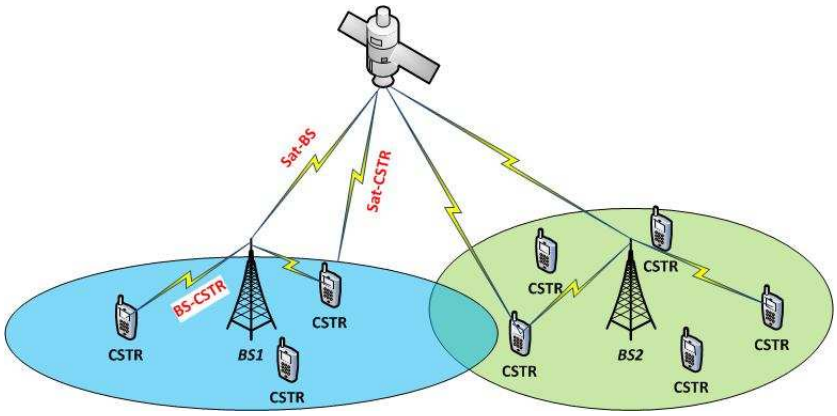

Figure 7.1: IEEE 802.22 WRAN based HSTS systems with cognitive satellite terrestrial radios.

7.1 Application Scenarios

In the proposed Cognitive HSTS, two scenarios are considered: (i) the IEEE 802.22 CR based wireless regional area network (WRAN) for long range communications [81], the first CR standard for opportunistic access to TV broadcasting bands; and (ii) the CR based Ultra Wide Band (UWB) communication system for short range personal area networks (PAN). Based on these two possible applications, a satellite-WRAN and a satellite UWB for PANs systems are presented in this section.

7.1.1 Hybrid Satellite-IEEE 802.22 System for WRANs

The IEEE 802.22 Standard addresses DSA for long range communications using the VHF and UHF bands allocated to the TV broadcasting service in the frequency range between 54 MHz and 862 MHz, while avoiding interference towards the primary users of this service. The typical coverage range envisaged in the standard is a radius between 10 km and 30 km from the cognitive BS depending on its ERP and antenna height. However, the MAC is also able to accommodate user terminals located as far as 100 km with proper scheduling of the traffic when exceptional propagation conditions are present. With the PHY implemented in this standard, WRAN systems are able to cover up to 30 km without special scheduling.
The proposed hybrid satellite-IEEE 802.22 scenario is shown in Figure 7.1. The IEEE 802.22 WRAN uses a cell structure, with the possibility of employing multiple satellites. The downlink transmissions from the satellite cover the BS and the CSTRs, while uplink transmissions are performed only by the BSs.

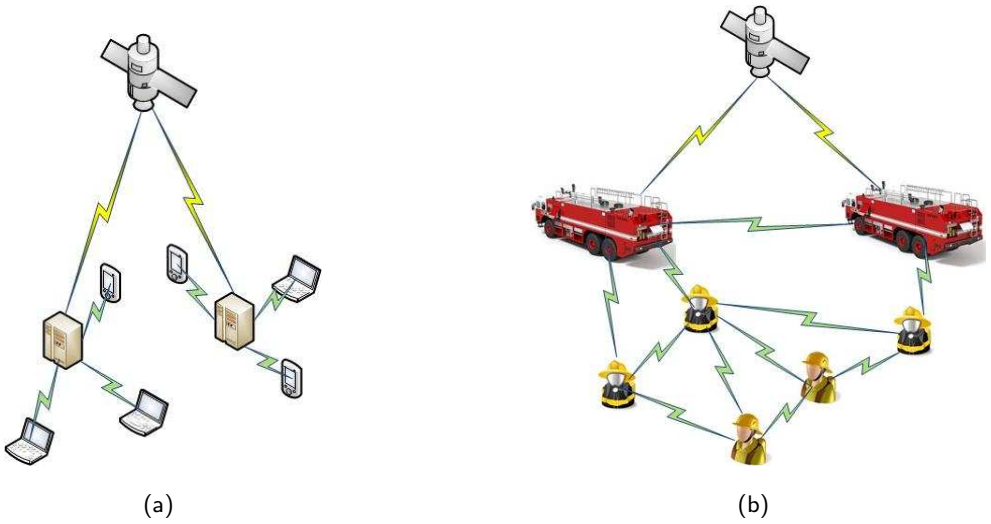

Figure 7.2: UWB PAN-based HSTS with UWB cognitive satellite terrestrial radios (a) for low data rate (emergency services) applications and (b) for high data rate applications.

7.1.2 Hybrid Satellite-UWB System for PANs

UWB systems in the frequency band ranging from 3.1 GHz to 10.6 GHz are perfect candidates for the introduction of cognitive techniques, considering their implicit requirements for coexistence with other wireless services. The following two UWB-based application scenarios can be envisaged: (i) a high rate, short distance communication system; and (ii) a low rate, medium distance communication one, combined with ranging and positioning. The former led to the definition of the Wi-Media UWB industrial standard, with an OFDM-based physical layer which is capable of guaranteeing data rates in the order of 500 Mbps for distances up to 10 m. The second scenario was investigated within the IEEE 802.15.4a Task Group, where an Impulse Radio UWB (IR-UWB) physical layer was outlined. This layer allows to provide data rates up to 25 Mbps and accurate ranging information as well, required for positioning [82–85].

As high rate and low rate UWB systems pose difficult challenges for the coexistence with primary systems, both of them will be taken into account in the following. In particular, Figure 7.5(a) shows a possible high data rate scenario, with several information storage stations equipped with UWB devices send information to mobile devices, which can be PDAs, laptops, etc. On the other hand, Figure 7.5(b) depicts a typical low rate hybrid satellite-terrestrial application, consisting of an emergency

network with UWB devices exchanging data and performing ranging, in order to help the emergency management through proper outdoor/indoor communications and positioning.

7.2 Cognitive Functionalities in HSTS

Satellite and terrestrial systems are capable of exploiting several realtime information, in order to maximize the efficiency of spectrum usage and to improve the communication performance. Thus, some of the cognitive functionalities that a network planner might think of are already implemented in these systems.

7.2.1 Satellite Communications

Aiming at providing the required QoS, satellite systems already make use of some realtime information, and some of them can be listed as follows:

- *satellite orbital knowledge*, *i.e.* information on the satellite orbits, which can be Low Earth Orbit (LEO), Medium Earth Orbit (MEO), Geostationary Earth Orbit (GEO), polar, elliptical, etc.;
- *link knowledge*, like rain fading conditions, in order to have adaptive coding and modulation at the receiver;
- *Doppler knowledge*, for frequency synchronization and Doppler-assisted satellite tracking;
- *network constellation knowledge*, for operations like handover mechanisms;
- *satellite service*, *i.e.* the knowledge on the required service, which might be broadcasting, voice, etc.

7.2.2 Terrestrial Communications

Coexistence analysis for terrestrial systems is a well investigated subject. The first standards related to this topic provided methods for measuring and mitigating interference through manual coordination [86]. Later, people realized that many of these techniques could be automatically performed by the network entities, thus leading to Dynamic Frequency Selection (DFS) and Power Control (PC). Thus, even before the advent of CR and DSA, several information are already available at the terrestrial network components. Some of them are *channel knowledge*, in order to aid channel

selection, or *Channel State Information (CSI)*, which includes all the information on the wireless link, in order to perform link adaptation, etc. However, the future CR-based wireless systems require a higher level of intelligence, which includes (but is not limited to) the following information:

- *radio knowledge*, *i.e.* information on the existing systems and their operating frequency bands. This information shall also be updated realtime, in order to continuously monitor the primary operations, avoiding harmful interference towards the licensed services;
- *location*, as knowing the position of the PUs might help in defining the effect of secondary operations on their performance. Furthermore, knowledge on the CRs positions would allow to exploit this information in order to perform better cooperative algorithms for spectrum monitoring or sharing;
- *interference temperature knowledge*, *i.e.* the total amount of interference generated on the PUs, from which appropriate transmission characteristics of the CRs can be deduced (see Section C.4).

7.2.3 Hybrid Satellite-Terrestrial System Communications

The knowledge examples provided in the previous section form the core part of a CR network. However, in a HSTS system they can be included in the terrestrial ground transmissions only. The satellite downlink can not adopt them, due to several practical limitations in controlling the satellite transmissions. First of all, the wide satellite coverage area, which makes particularly challenging a dynamic spectrum sharing: even with a spot beam for the satellite downlink, with a 100 km radius, incorporating these cognitive functionalities seems to be quite difficult, due to the potential interference on primary terrestrial services on such a wide area. Thus, in the proposed Cognitive HSTS architecture, only the satellite uplink will be taken into account for cognitive approaches, as it cause a lower level of interference to terrestrial systems thanks to highly directional upward transmissions and low elevation angles, while the satellite downlink will operate without DSA capabilities.

7.3 CSTR Architecture

The proposed architecture consists of both the satellite and terrestrial radios associated with it. Terrestrial communications, as well as satellite uplink transmissions,

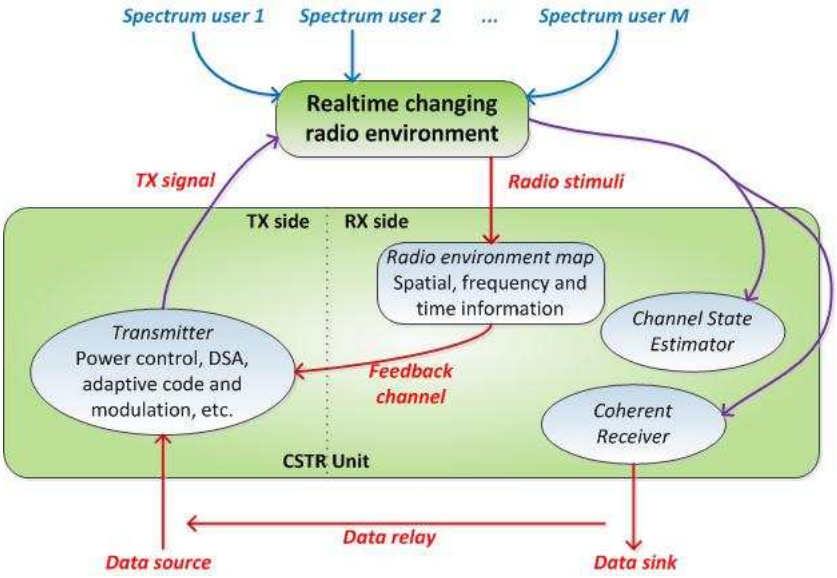

Figure 7.3: Architecture model of the Cognitive Satellite Terrestrial Radio for HSTSs.

incorporate cognitive functionalities, while the satellite downlink has no DSA capabilities. It is worthwhile reminding that the uplink transmissions towards the satellite are managed through the BSs, and never from the mobile terminals, while the satellite downlink can be received by both BSs and CSTRs.
A typical cognitive engine follows the so called *cognitive cycle* to continuously monitor the spectrum and learn form the surrounding environment, in order to properly modify its behaviour. Reminding to Section C.3 for further details, the tasks performed during the cognitive cycle are:

- spectrum monitoring, *i.e.* periodically sense the frequency spectrum in order to identify vacant channels and change operating frequency in case a PU requires the licensed spectrum;
- spectrum analysis, which schedules and plans proper spectrum access for the unlicensed users;
- spectrum decision, which basically acts as a cognitive MAC layer;
- reconfiguration, for the proper modification of the transmission parameters, which of course shall be completed seamlessly to the users.

The above cognitive features led to the definition of the CSTR system model shown in Figure 7.3 [87], where the additional functionalities for the required level of intelli-

gence are also provided. The HSTS on the ground has a manifold user environment, and all of them are assumed to implement DSA techniques. Sophisticated strategies are required for opportunistic spectrum sharing in such an environment. It is worthwhile noting that, though the sharing is increased when the number of users increases, resulting in a reduction of the effective throughput per channel, there are also benefits for the cognitive network as described in the following.

7.3.1 Spectrum Monitoring Module

Spectrum monitoring and PUs detection are crucial functionalities in a cognitive network (see Section C.4). CSTR nodes have to detect any PU in the radio environment in order to both exploit unused spectrum resources and avoid harmful interference. In the last years, a plethora of spectrum monitoring techniques have been proposed, ranging from blind to non-blind methods [88–90]. In this section, the energy detection blind method is described [91–93].

According to an energy detection approach, the CSTR estimates the signal level in the radio stimuli on a certain channel, and makes a decision on the presence or not of a PU by comparing this measured level with a predefined threshold. The main drawback of this method is that low power signals can easily lead to miss detection, or, on the other hand, there could be false alarm triggered by the noise power. Miss detection events could lead to harmful interference towards the licensed users. The signal sensed by the i-th cognitive node, $i = 1, 2, \ldots, M$, at time t is given by equation (C.1):

$$r_i(t) = \begin{cases} n_i(t), & H_0 \\ h_i(t) \cdot s(t) + n_i(t), & H_1 \end{cases}$$

where $r_i(t)$ is the received signal at the CR front-end, $s(t)$ is the eventually transmitted PU signal, $h_i(t)$ the channel gain, and $n_i(t)$ the AWGN with zero mean and variance σ_i^2. The test statistic the detection at the i-th node, θ_i, is then given by:

$$\theta_i = \int_{t_1}^{t_2} r_i(t)\tilde{r}_i(t)\mathrm{d}t, \ t_1, t_2 \in \mathbb{R}^+ \tag{7.1}$$

where $\tilde{r}_i(t)$ is the complex conjugate of $r_i(t)$. The performance of the energy detector depends on the time-bandwidth product, which corresponds to the number of observed samples. For increasing values of this number, more energy/power is measured at the cognitive node, and thus the performance is better. However, increasing

too much the time-bandwidth product could lead to unacceptable observation periods, considering that PU detection shall be performed as rapidly as possible. The decision at the i-th node on the presence/absence of PU transmissions is:

$$\widehat{b}_i = \begin{cases} \widehat{H}_0, & \theta_i < \mu_i \\ \widehat{H}_1, & \theta_i \geq \mu_i \end{cases} \tag{7.2}$$

where μ_i is the detection threshold used by the i-th CSTR. Considering the manifold user environment, the CR network can make use of all the decisions made by each CSTR to collectively decide whether an PU is present or not. The BS fuses the data to perform cooperative decisions on the presence of a licensed user. For cooperation, it should be underlined that signalling from CRs to the BS is not granted in general.

7.3.2 Location Assisted Systems

The possibility of exchanging position-related information about both primary and cognitive users is a key aspect in the deployment of cognitive systems, as Radio Environment Maps (REM) [94]. Whenever available, GPS is definetly the simplest manner to obtain position information. However, hardware limitations or bad propagation conditions (*e.g.* indoor or dense urban scenarios) might make it difficult to use this system, either for some or all the network nodes. In this case, cooperation among the terminals is required.

In the literature, several solutions rely on the combination of distributed positioning algorithms, for gathering relative locations of nodes within the network, and absolute position information, provided by a subset of terminals in known positions (the so called *anchor terminals*). The former algorithms are based on the capability of the cognitive nodes to evaluate their mutual distances, thus requiring information exchange between them in order to build a network map by solving a triangulation problem. The performance of these algorithms is deeply affected by the accuracy of the distance estimation, and thus an accurate distance measurement technology such as the UWB one proposed in Figure 7.5(b) might significantly improve the localization performance.

7.3.3 Manifold Access and Interference Temperature

Access to the available spectrum resources identified by the spectrum monitoring engine is performed by means of either cooperation or competition among the cog-

nitive terminals, as outlined in the following. In particular, the focus will be on the latter strategy:

- *cooperative access*: the manifold access problem has a direct solution where a set of protocols are defined, in order to allow efficient and fair resource reutilization by all the nodes in the network;

- *competition-based access*: all the nodes compete for the radio resources, thus requiring a sophisticated mechanism to avoid collisions and provide fare spectrum sharing. In the recent years, several solutions have been proposed to the competition problem. For instance, such problem can be considered as a *game theoretic problem* with a five-tuple *stochastic game* defined by $\{\mathcal{N}, \mathcal{S}, \overline{\mathcal{A}}, \mathcal{P}, \overline{\mathcal{R}}\}$ where: $\mathcal{N}$ is the set of active players, $i = 1, 2, \ldots, M$, $\mathcal{S}$ is the set of possible states, $\overline{\mathcal{A}}$ is the joint action set available to all the players of the game, $\mathcal{P}$ the transition probability function related to the joint actions, and $\overline{\mathcal{R}}$ is a function of $\overline{\mathcal{A}}$ related to the payoff to each player. Given finite action set for the CSTR supposed to act, an action profile is reached, given by the best response to all the other players' action, leading to the Nash Equilibrium state [95]. Finally, the CSTR adapts its transmission power, and other characteristics, according to the resulting action strategy.
  Unfortunately, the Nash Equilibrium is not always reached, depending on temporal variations, bandwidth requirements, interference map, etc. In such cases, a possible solution is to introduce a referee with the power to dive and take spectral resources.

Before concluding this section, an important remark shall be made. The multiple transmissions performed by all the cognitive nodes in the network might lead to high level of aggregate network interference, either on frequency adjacent primary services or in the cognitive network itself. In order to cope with this challenge, FCC introduced the Interference Temperature Model [96]. According to this paradigm, all the CSTRs shall be able to estimate the noise-plus-interference level from all sources of signals at each primary receiver. This information, and the choice of a proper interference limit level at the PU, would lead to the selection of a transmission power that does not generate harmful interference at the primary receiver.

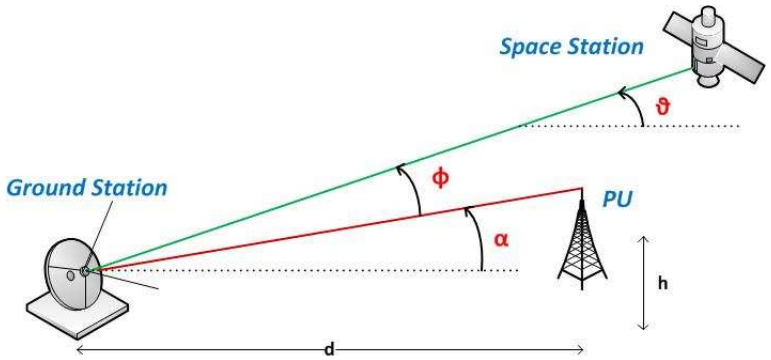

Figure 7.4: 3D spectrum monitoring model considering the Ground Station.

7.4 3D Spectrum Reutilization

The proposed Cognitive Satellite Terrestrial System architecture allows to introduce a 3rd dimension in the spatial frequency reutilization, as depicted in Figure 7.4. Considering the satellite-WRAN HSTS scenario, the satellite ground terminal acts as a CSTR, facilitating frequency sharing with the other terrestrial systems. The terrestrial primary transmitter (*e.g.* a DVB-T transmitter) has the same azimuth angle as the satellite, with respect to the Ground Station (GS). Furthermore: θ is the satellite elevation angle; α is the PU elevation angle; and ϕ is the angle between the antenna main-lobe axis and the direction of the PU transmitter. In particular, it can be noticed that $\phi = \theta - \alpha$. It is also worthwhile noting that the case where $\alpha > 0$ is considered, which might not be true for all the possible scenarios.
In order to opportunistically access the spectrum in the depicted 3rd dimension, the CSTR performs spectrum monitoring to detect any PUs on a certain channel. Since the GS typically deploys parabolic dish antennas, with highly directive gains, the detection of any neighbouring PU on the ground becomes particularly challenging with lower antenna heights (at higher values of ϕ). In order to evaluate the performance in terms of complementary Receiver Operating Characteristics (ROC), the antenna gain requirements for the GS with parabolic antenna are provided by [97]:

$$G[dBi] = \begin{cases} G_0 - 25\log_{10}\phi, & 1^\circ \leq \phi < 48^\circ \\ -10, & 48^\circ \leq \phi < 180^\circ \end{cases} \tag{7.3}$$

where $G_0 = 32$ dBi. Furthermore, in the simulations the signal power at the GS front-end and the receiver noise power are assumed to be respectively $P_A = 0$ dBm and $P_N = 6$ dBm.

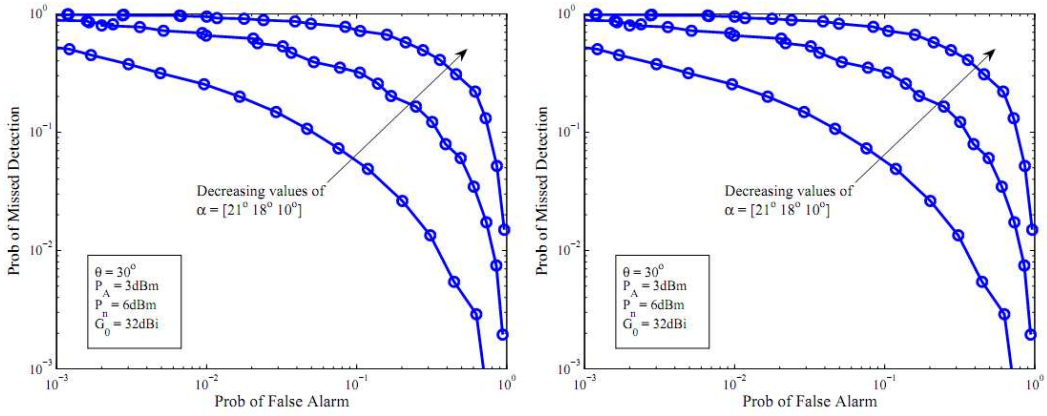

(a) PU elevation angle (b) Satellite elevation angle

Figure 7.5: Complementary ROC curves for 3D spatial spectrum reutilization as a function of the PU elevation angle (a) and the satellite elevation angle (b).

7.4.1 Numerical Results

Using the energy detector depicted in Section 7.3.1, some simulation results are now provided on the PU detection performed by the GS. In Figure 7.5(a) the complementary ROC is shown for several values of α. It can be noticed that, due to the directional radiation pattern of the parabolic antenna, the detection performance becomes worse when α decreases, as for a fixed probability of correct detection the probability of false alarm is higher. On the other hand, in Figure 7.5(b), the performance are worse for increasing values of θ. Therefore, considering the 3rd spatial dimension, the detection accuracy on the ground becomes harder depending on the directional antenna patterns, as both increasing θ and decreasing α consequently makes the GS receive the PU transmissions in correspondence of low antenna radiation pattern gains. However, it shall also be noted that such highly directional antennas also produce less interference in the direction of the primary transmitter.

Appendix A

Basic Properties of the Poisson Point Process

In this Appendix the definitions, properties, and theorems which will be referred to in Part I are introduced. More detailed information on Point Process theory, or on Poisson Point Processes, can be found in [24, 26, 98].

A.1 Point Process Theory

Consider a d-dimensional Euclidean space $\mathbb{R}^d$ and the set S of all the possible sequences of points in it, such that any sequence ϕ belonging to S:

- is finite, *i.e.* the number of points in any bounded subset of $\mathbb{R}^d$ is finite;
- is simple, *i.e.* $x \neq y,\ \forall x, y \in \phi$.

From an informal point of view, a Point Process (PP) Φ on the Euclidean space $\mathbb{R}^d$ is a random variable whose values are the "point patterns" ϕ taken from the set S. Thus, a realization of the Point Process $\phi \in \Phi$ is a finite and simple subset of the Euclidean space $\mathbb{R}^d$. A Point Process Φ can also be thought of as a *counting measure*. Consider a subset $A \subset \mathbb{R}^d$, the process Φ can be decomposed as follows:

$$\Phi(A) = \sum_{x_i \in \Phi} \delta_{x_i}(A)$$

where $\delta_x(A)$ is the Dirac measure at the point x, *i.e.* $\delta_x(A) = 1$ if $x \in A$ and $\delta_x(A) = 0$ otherwise. Thus, $\Phi(A)$ gives the number of points of the Poisson Point Process belonging to the subset A.

A useful property of simple Point Processes is that they are completely characterized by their *void probabilities* on compact subsets of $\mathbb{R}^d$, $\mathbb{P}\{\Phi(A) = 0\}$, *i.e.* the probability that there are no points of the process belonging to a given compact subset $A \in \mathbb{R}^d$. To verify the equivalence of two simple Point Processes, it is thus sufficient to check the equality of their void probabilities on all compact subsets of the Euclidean space $\mathbb{R}^d$.

A.2 Poisson Point Process

In the following, the focus will be on Poisson Point Processes (PPP), as they provide the best tools for a proper modeling of next-generation networks, like cognitive radio networks. Consider a finite non-null measure Λ on the Euclidean space $\mathbb{R}^d$:

Definition A.1. A Poisson Point Process (PPP) of density measure Λ is defined by means of its finite-dimensional distributions:

$$\mathbb{P}\{\Phi(A_1) = n_1, \Phi(A_2) = n_2, \ldots, \Phi(A_k) = n_k\} = \prod_{i=1}^{k} e^{-\Lambda(A_i)} \frac{\Lambda(A_i)^{n_i}}{n_i!} \tag{A.1}$$

for every $k = 1, 2, \ldots$ and all bounded, mutually disjoint sets A_i, $i = 1, 2, \ldots, k$. If $\Lambda(\mathrm{d}x) = \lambda \mathrm{d}x$ is a multiple of the Lebesgue measure (*i.e.* volume) in $\mathbb{R}^d$, Φ is a *homogeneous* Poisson Point Process with density λ.

The void probability of a Poisson Point Process over the subset $A \in \mathbb{R}^d$ is given by $\exp(-\lambda|A|)$, where $|A|$ is the Lebesgue measure of A. Furthermore, following from Definition (A.1), Φ is a PPP if and only if for every $k = 1, 2, \ldots$ and all bounded, mutually disjoint sets $A_i \subset \mathbb{R}^d$, $i = 1, 2, \ldots, k$, $[\Phi(A_1), \Phi(A_2), \ldots, \Phi(A_k)]$ is a vector of independent Poisson random variables with density measures $\Lambda(A_1), \ldots, \Lambda(A_k)$ respectively. In particular, $\mathbb{E}\{\Phi(A)\} = \Lambda(A)$ for all $A \subset \mathbb{R}^d$.

Spatial invariance properties and multinomial distribution

As stated in the introduction to this Part, Poisson Point Processes are particularly attractive due to their spatial randomness and independence qualities. Some of these properties, together with the definition of multinomial distribution, are provided in this section.

- *Stationarity*: a PPP Φ is stationary if its distribution is invariant under a translation through any vector $v \in \mathbb{R}^d$, *i.e.* if

$$\mathbb{P}\{(v+\Phi) \in \Gamma\} = \mathbb{P}\{\Phi \in \Gamma\}, \ \forall v \in \mathbb{R}^d \text{ and } \forall \Gamma \subset \mathbb{R}^d$$

  where $v + \sum_{x_i \in \Gamma} \delta_{x_i}(\Gamma) = \sum_{x_i \in \Gamma} \delta_{v+x_i}(\Gamma)$. If Φ is stationary, then its density measure is given by $\Lambda(A) = \lambda|A|$. It is worthwhile noting that, according to Definition (A.1), a stationary PPP is also homogeneous;

- *Isotropy*: a PPP Φ is isotropic if its distribution is invariant under a rotation around the origin, *i.e.* if $\mathcal{O}\Phi = \{\mathcal{O}x : x \in \Phi\}$ has the same distribution as Φ for any rotation $\mathcal{O}$ around the origin;

- *Motion-invariance*: a Point Process which is both stationary and isotropic is defined as motion-invariant;

- *Multinomial distribution*: let W be a bounded observation window and let $A_1, A_2, \ldots, A_k$, $k = 1, 2, \ldots$ be some partition of this window: $A_i \bigcap A_j = \emptyset$ for $i \neq j$ and $\bigcup_i A_i = W$. For all $n, n_1, n_2, \ldots, n_k \in \mathbb{N}$ with $\sum_{i=1}^{k} n_i = n$, the multinomial distribution of the PPP Φ is given by:

$$\begin{aligned} &\mathbb{P}\{\Phi(A_1) = n_1, \Phi(A_2) = n_2, \ldots, \Phi(A_k) = n_k | \Phi(W) = n\} = \\ &= \frac{n!}{n_1! n_2! \cdots n_k!} \frac{1}{\Lambda(W)^n} \prod_{i=1}^{k} \Lambda(A_i)^{n_i} \end{aligned} \tag{A.2}$$

The last property shows that given that there are n points in the observation window W, these points are independently and identically distributed (i.i.d.) in W with probability of belonging to A_i equal to $\frac{\Lambda(A_i)}{\Lambda(W)}$. From another point of view, consider a density measure Λ and a bounded subset of the space $W \subset \mathbb{R}^d$, and take into account the independent random objects $\{N, X_1, X_2, \ldots\}$. Thus:

- N is a Poisson random variable with parameter $\Lambda(W)$.

- $X_1, X_2, \ldots$ are i.i.d. vectors (points) taking values in $W \subset \mathbb{R}^d$ with probability $\mathbb{P}\{X_j \in A_i\} = \Lambda(A_i)/\Lambda(W)$.

Consequently, the simulation of an infinite Poisson Point Process in a compact set A is extremely simple, as it is sufficient to uniformly distribute N points over a truncated set [32]. As an example, consider a compact set $A \subset \mathbb{R}^2$ and a homogeneous PPP Φ. In order to simulate an infinite PPP truncating the plane to a closed disk

$b(o,s)$ (where o is the origin and s the radius), one only has to generate a Poisson random variable $N \sim Poisson(\lambda\pi s^2)$[1], which determines the number of points to be deployed in $b(o,s)$, and to uniformly place these points in $b(o,s)$. More details on the truncation radius and simulation complexity are provided in Section 1.3.5.

Laplace Functional

A complete characterization of the distribution of a Point Process is given by its Laplace functional, which plays a similar role as the characteristic function for random variables.

Definition A.2. The Laplace functional of a Point Process Φ is defined by the following formula:

$$\mathcal{L}_\Phi(f) = \mathbb{E}_\Phi\left\{e^{-\int_{\mathbb{R}^d} f(x)\Phi(\mathrm{d}x)}\right\} \tag{A.3}$$

where f runs over the set of all non-negative functions on $\mathbb{R}^d$.

Consider a function $f(x) = \sum_{i=1}^{k} t_i \mathbf{1}(x \in A_i)$, where $\mathbf{1}(n)$ is the unit function[2]. The Laplace functional is given by:

$$\mathcal{L}_\Phi(f) = \mathbb{E}_\Phi\left\{e^{-\sum\limits_{i=1}^{k} t_i\Phi(A_i)}\right\}$$

which is the joint Laplace transform of the random vector $[\Phi(A_1), \Phi(A_2), \ldots, \Phi(A_k)]$. In case $A_1, A_2, \ldots, A_k$ run over all the possible subsets of the space $\mathbb{R}^d$, a complete characterization of all finite-dimensional distributions of the PP is obtained.

Proposition A.1. *The Laplace functional of a Poisson Point Process Φ with density measure Λ is given by:*

$$\mathcal{L}_\Phi(f) = e^{-\int_{\mathbb{R}^d}\left(1-e^{-f(x)}\right)\Lambda(\mathrm{d}x)} \tag{A.4}$$

---

[1] The density measure of the points on the disk $b(o,s)$ is given by $\Lambda(b(o,s)) = \lambda|b(o,s)| = \lambda\pi s^2$.

[2] $\mathbf{1}(n) = 1$ if $n = 1$, 0 otherwise.

Proof. Consider a non-negative function $f(x)$ and the function $g(x) = f(x)\mathbf{1}(x \in A)$, where A is a bounded subset belonging to the σ-algebra of $\mathbb{R}^d$. The Laplace functional on the subset A is given by:

$$\mathcal{L}_\Phi(g)|_A = \mathbb{E}_\Phi\left\{e^{-\int_{\mathbb{R}^d} g(x)\Phi(\mathrm{d}x)}\right\} = \mathbb{E}_\Phi\left\{e^{-\int_A f(x)\Phi(\mathrm{d}x)}\right\}$$

Writing the PPP as the counting measure $\Phi(A) = \sum_{x_i\in\Phi}\delta_{x_i}(A)$ yields to:

$$\mathcal{L}_\Phi(g)|_A = \mathbb{E}_\Phi\left\{e^{-\sum_{x_i\in A} f(x_i)}\right\}$$

where averaging over the PPP Φ denotes the mean over the locations of the points x_i. This can be re-written as the mean on the distribution of points in A conditioned to the number of points in this set, and then deconditioned on the number of points which is a Poisson random variable. As previously shown, the points in A are i.i.d. and uniformly distributed according to the law $\mathbb{P}\{x \in \cdot\} = \Lambda(\cdot)/\Lambda(A)$, and thus:

$$\mathcal{L}_\Phi(g)|_A = \underbrace{e^{-\Lambda(A)}\sum_{n=0}^{\infty}\frac{\Lambda(A)^n}{n!}}_{\mathbb{P}\{\Phi(A)=n\}}\overbrace{\int_A\cdots\int_A}^{n} e^{-\sum_{i=1}^{n} f(x_i)}\frac{\Lambda(\mathrm{d}x_1)}{\Lambda(A)}\cdots\frac{\Lambda(\mathrm{d}x_n)}{\Lambda(A)}$$

where each point in A is distributed according to the probability density function (pdf) $\Lambda(\mathrm{d}x)/\Lambda(A)$. Writing the exponential of a summation as the product of the exponentials, and thanks to the independence property of the points:

$$\begin{aligned}
\mathcal{L}_\Phi(g)|_A &= e^{-\Lambda(A)}\sum_{n=0}^{\infty}\frac{\Lambda(A)^n}{n!}\frac{1}{\Lambda(A)^n}\left[\int_A e^{-f(x)\Lambda(\mathrm{d}x)}\right]^n \\
&= e^{-\Lambda(A)}\sum_{n=0}^{\infty}\frac{1}{n!}\left[\int_A e^{-f(x)\Lambda(\mathrm{d}x)}\right]^n \\
&\overset{(a)}{=} e^{-\Lambda(A)}e^{\int_A e^{-f(x)}\Lambda(\mathrm{d}x)} \\
&= e^{-\int_A\left(1-e^{-f(x)}\right)\Lambda(\mathrm{d}x)}
\end{aligned}$$

where (a) follows from the well known series expansion $\sum_{n=0}^{\infty}\frac{t^n}{n!} = e^t$. The proof is concluded by considering an increasing sequence of bounded subsets $A_k \to \mathbb{R}^d$ and using the monotone convergence theorem:

$$\mathcal{L}_\Phi(g)|_{A_k} = e^{-\int_{A_k}\left(1-e^{-f(x)}\right)\Lambda(\mathrm{d}x)} \underset{\left(A_k\to\mathbb{R}^d\right)}{\longrightarrow} e^{-\int_{\mathbb{R}^d}\left(1-e^{-f(x)}\right)\Lambda(\mathrm{d}x)} = \mathcal{L}_\Phi(f)$$

□

Probability Generating Functional

The Probability Generating Functional (PGFL) is the equivalent of the Moment Generating Functional for Point Processes.

Definition A.3. Let $\nu(x) : \mathbb{R}^d \to [0, +\infty)$ be a measurable function. The PGFL of a Point Process Φ is defined as:

$$\mathcal{G}[\nu] = \mathbb{E}_\Phi \left\{ \prod_{x \in \Phi} \nu(x) \right\} \tag{A.5}$$

Proposition A.2. *The Probability Generating Functional of a Poisson Point Process Φ with density measure Λ is given by:*

$$\mathcal{G}[\nu] = \exp\left[- \int_{\mathbb{R}^d} (1 - \nu(x))\, \Lambda(\mathrm{d}x) \right] \tag{A.6}$$

Proof. The procedure is similar to that used for the Laplace functional. Given that there are n points in Φ, from Definition (A.3) the PGFL can be written as:

$$\mathcal{G}^{(n)}[\nu] = \mathbb{E}_\Phi \left\{ \prod_{i=1}^{n} \nu(x_i) \right\}$$

and thus considering that the points of the PPP are i.i.d. and uniformly distributed, it is possible to sum over all possible values of n and then decondition on the uniform distribution $\mathbb{P}\{x \in \cdot\} = \Lambda(\cdot)/\Lambda(A)$, with $A \subset \mathbb{R}^d$:

$$\mathcal{G}[\nu] = \sum_{n=0}^{\infty} \mathcal{G}^{(n)}[\nu] = \sum_{n=0}^{\infty} \int_{\mathbb{R}^d} \cdots \int_{\mathbb{R}^d} \prod_{i=1}^{n} \nu(x_i) \mathbb{P}(\mathrm{d}x_1) \cdots \mathbb{P}(\mathrm{d}x_n)$$

Now consider a function $f(x) = \nu(x)\mathbf{1}(x \in A)$:

$$\begin{aligned}
\mathcal{G}[f]|_A &= \sum_{n=0}^{\infty} \int_A \cdots \int_A \prod_{i=1}^{n} \nu(x_i) \mathbb{P}(\mathrm{d}x_1) \cdots \mathbb{P}(\mathrm{d}x_n) \\
&= e^{-\Lambda(A)} \sum_{n=0}^{\infty} \frac{\Lambda(A)^n}{n!} \frac{1}{\Lambda(A)^n} \int_A \cdots \int_A \prod_{i=1}^{n} \nu(x_i) \Lambda(\mathrm{d}x_1) \cdots \Lambda(\mathrm{d}x_n) \\
&= e^{-\Lambda(A)} \sum_{n=0}^{\infty} \frac{1}{n!} \left[\int_A \nu(x) \Lambda(\mathrm{d}x) \right]^n = \exp\left[- \int_A (1 - \nu(x))\, \Lambda(\mathrm{d}x) \right]
\end{aligned}$$

The proof is concluded by considering an increasing sequence of bounded subsets $A_k \to \mathbb{R}^d$ and using the monotone convergence theorem:

$$\mathcal{G}[f]|_{A_k} = \exp\left[-\int_{A_k}(1-\nu(x))\,\Lambda(\mathrm{d}x)\right] \underset{\left(A_k\to\mathbb{R}^d\right)}{\longrightarrow} \exp\left[-\int_{\mathbb{R}^d}(1-\nu(x))\,\Lambda(\mathrm{d}x)\right] = \mathcal{G}[\nu]$$

□

The PGFL is extremely useful for evaluating the Laplace transform of the sum $\sum_{x\in\Phi} f(x)$:

$$\mathcal{L}_f(s) = \mathbb{E}_\Phi\left\{e^{-s\sum_{x\in\Phi} f(x)}\right\} = \mathbb{E}_\Phi\left\{\prod_{x\in\Phi} e^{-sf(x)}\right\} = \mathcal{G}\left[e^{-sf}\right] \tag{A.7}$$

PPP-invariant Operations

The most attractive property of a Poisson Point Process is that many transformations and operations on it preserve the Poisson law. The concepts of superposition and thinning of a PPP are now introduced, concluding this section with the mapping theorem which involves the transformation of the Point Process from one Euclidean space to another one.

Definition A.4. The superposition of different Point Processes is defined as the sum $\Phi = \sum_k \Phi_k$, and it is still a Point Process if $\sum_k \mathbb{E}\{\Phi_k(\cdot)\}$ is a locally finite measure.

When considering the superposition of two PPPs, the following Proposition applies:

Proposition A.3. *The superposition of independent Poisson Point Processes with density measures Λ_k is a Poisson Point Process with density measure $\sum_k \Lambda_k$ if and only if the latter is a locally finite measure.*

Proof. By definition of PPP, the densities Λ_k are all locally finite, and thus the superposition is still a Point Process. Its Laplace functional can be evaluated as:

$$\begin{aligned}
\mathcal{L}_{\Phi}(f) &= \mathbb{E}_{\Phi_k}\left\{e^{-\sum_k \int_{\mathbb{R}^d} f(x)\Phi_k(\mathrm{d}x)}\right\} = \mathbb{E}_{\Phi_k}\left\{\prod_k e^{-\int_{\mathbb{R}^d} f(x)\Phi_k(\mathrm{d}x)}\right\} \\
&= \prod_k \mathbb{E}_{\Phi_k}\left\{e^{-\int_{\mathbb{R}^d} f(x)\Phi_k(\mathrm{d}x)}\right\} \\
&= \prod_k e^{-\int_{\mathbb{R}^d}\left(1-e^{-f(x)}\right)\Lambda_k(\mathrm{d}x)} \\
&= e^{-\int_{\mathbb{R}^d}\left(1-e^{-f(x)}\right)\sum_k \Lambda_k(\mathrm{d}x)}
\end{aligned}$$

and thus $\Phi = \sum_k \Phi_k$ is still a PPP with density measure $\Lambda = \sum_k \Lambda_k$. □

The invariant properties of the Poisson Point Processes allow to easily model some behaviours of the nodes in a cognitive network. From an informal point of view, the following thinning theorem states that the application of a certain function p to a PPP with density measure Λ transforms this process into another PPP with density measure $p\Lambda$. As an example, this makes the modeling of an ALOHA MAC protocol very simple, as it is sufficient to multiply the density measure Λ by the transmission probability of the protocol p.

Definition A.5. The thinning of a Point Process Φ with the retention function p is a Point Process given by:

$$\Phi^p(A) = \sum_k \varepsilon_k \delta_{x_k}(A) \tag{A.8}$$

where the random variables $\{\varepsilon_k\}_k$ are independent given Φ with $\mathbb{P}\{\varepsilon_k = 1|\Phi\} = 1 - \mathbb{P}\{\varepsilon_k = 0|\Phi\} = p(x_k)$ and $A \subset \mathbb{R}^d$.

Proposition A.4. *The thinning of a PPP with density measure Λ with the retention function p is a PPP having density measure $p\Lambda$ with $(p\Lambda)(A) = \int_A p(x)\Lambda(\mathrm{d}x)$.*

In conclusion, the mapping theorem is now provided. This theorem shows how, under certain conditions, the transformation from a space $\mathbb{R}^d$ to another space $\mathbb{R}^s$ still preserves the Poisson law.

Theorem A.1. ***Mapping Theorem.*** *Consider an inhomogeneous Poisson Point Process Φ on $\mathbb{R}^d$ with density measure Λ, and a measurable function $f : \mathbb{R}^d \to \mathbb{R}^s$ such that $\Lambda\left(f^{-1}(y)\right) = 0,\ \forall y \in \mathbb{R}^s$. If*

$$\mu(A) = \Lambda\left(f^{-1}(A)\right) < \infty$$

for all bounded subsets A, then $f(\Phi)$ is an inhomogeneous Poisson Point Process on $\mathbb{R}^s$ with density measure μ.

Furthermore, if the PPP Φ is stationary with density λ and $\mathbf{A}$ is a non-singular linear mapping, then $\mathbf{A}\Phi = \{\mathbf{A}x : x \in \Phi\}$ is still a stationary PPP with density $\lambda \det\left(\mathbf{A}^{-1}\right)$.

A.3 Palm Distributions

Palm distributions are the counterparts to the conditional distributions for Point Processes, and they arise when the Point Process is conditioned to have a point at $x \in \mathbb{R}^d$. They are thus particularly useful in cognitive networks, for example when the intent is to calculate the outage probability, as it requires conditioning on either the transmitter or the receiver location. In order to properly define Palm distribution, the concept of reduced Campbell measure has to be introduced first:

Definition A.6. The reduced Campbell measure of a Point Process Φ is the measure:

$$C^!\left(A \times Y\right) = \mathbb{E}_{\mathbb{P}}\left\{\int_A \mathbf{1}\left(\Phi \setminus \{x\} \in Y\right) \Phi(\mathrm{d}x)\right\} = \mathbb{E}_{\mathbb{P}}\left\{\sum_{x \in \Phi \bigcap A} \mathbf{1}\left(\Phi \setminus \{x\} \in Y\right)\right\} \tag{A.9}$$

for any Borel set $A \subset \mathbb{R}^d$ and $Y \in \mathcal{S}$.

In the above definition, $\mathcal{S}$ is the smallest σ-algebra such that the maps $\phi \to \phi(A)$ are measurable for all Borel subsets $A \subset \mathbb{R}^d$, and the expectation is performed over the Point Process distribution $\mathbb{P}$. With reference to the density measure of Φ, $\Lambda(A) = \mathbb{E}_{\mathbb{P}}\{\Phi(A)\} = \int_A \Phi(x)\mathbb{P}(\mathrm{d}x)$, the meaning of the reduced Campbell measure is easy to understand. While the density measure is the mean number of points of Φ in A, $C^!(A \times Y)$ is the refinement of this mean measure: it gives the expected number of points of Φ in A such that when removing a specific point from Φ, the resulting configuration satisfies property Y. An immediate consequence of this definition is the following theorem:

Theorem A.2. ***Mecke's Theorem.*** *Let $f(x, \phi)$ be a measurable function on $\mathbb{R}^d \times \mathcal{S}$. Then:*

$$\mathbb{E}_{\mathbb{P}}\left\{\sum_{x\in\Phi} f(x, \Phi \setminus \{x\})\right\} = \int_{\mathbb{R}^d}\int_{\mathcal{S}} f(x,\phi)C^!(\mathrm{d}x, \mathrm{d}\phi) \tag{A.10}$$

The above theorem states that the expected value of a measurable function (*e.g.* the path-loss law) over a Point Process cleared of a specific point is equivalent to averaging this function over all the values of x and all the possible sequences of points, with the mean computed through the reduced Campbell measure evaluated over the whole space, *i.e.* evaluated removing once a time each point of the process, and for each point we remove all possible sequences of points are taken into account. If $C^!(\cdot \times Y)$ is absolutely continuous with respect to the density measure Λ, then it is possible to re-write the reduced Campbell's measure as:

$$C^!(A \times Y) = \int_A \mathbb{P}^{!x}(Y)\Lambda(\mathrm{d}x) \tag{A.11}$$

where $\mathbb{P}^{!x}$ is the so called *reduced Palm distribution* of the Point Process Φ given a point at x, and it can be seen as the conditional distribution of the process given that x is a point which is not counted.

Slivnyak's theorem

This chapter is concluded with Slivnyak's theorem and the non-reduced Campbell's measure and Palm distribution. In particular, the former is fundamental for the

characterization of a Poisson Point Process, and has deep implications on the computational complexity for the evaluation of the aggregate interference or other performance metrics (*e.g.* coverage probability, rate, etc.) as will be shown in the following chapters.

Theorem A.3. ***Slivnyak's theorem****. For a Poisson Point Process* Φ*, the reduced Palm distribution equals the distribution of the process itself for all* $x \in \mathbb{R}^d$*, i.e.:*

$$\mathbb{P}^{!x} \equiv \mathbb{P}$$

This theorem provides a complete characterization of the PPP. It states that removing a point x does not change the distribution of the other points of the PPP Φ as long as this point of the process was not counted. The computational implication of this theorem is crucial. The complexity of interference calculations is $\mathcal{O}\left(N^2\right)$, with N being the number of nodes in the network. This happens because usually the interactions between each pair of nodes, *i.e.* the contribution of each node i to the overall interference seen by node j [32], has to be computed. However, thanks to Slivnyak's theorem, only the computation of the performance metrics as seen by a "typical" receiver in a given location, *e.g.* the origin, is required. If Φ is a stationary PPP, Mecke's theorem allows to write the following expectation:

$$\mathbb{E}_{\mathbb{P}}\left\{\sum_{x\in\Phi} f\left(x, \Phi \setminus \{x\}\right)\right\} = \lambda \int_{\mathbb{R}^d} \mathbb{E}_{\mathbb{P}}\left\{f(x,\Phi)\right\} \mathrm{d}x$$

i.e. the mean of a function (*e.g.* the path-loss law) over a stationary PPP is given by the mean of this function over the PPP distribution in the whole Euclidean space $\mathbb{R}^d$, multiplied by the process density λ.

In conclusion, the non reduced expression of the Campbell measure and the Palm distribution can be defined as follows:

$$C\left(A \times Y\right) = \mathbb{E}_{\mathbb{P}}\left\{\sum_{x\in\Phi} \mathbf{1}\left(\Phi \in Y\right)\right\} = \int_A \mathbb{P}^x(Y)\Lambda(\mathrm{d}x) \tag{A.12}$$

Another important result of Palm theory is the following theorem, which allows to compute the mean of a measurable function on the PPP thanks to its density function, $\Lambda(x)$:

Theorem A.4. ***Campbell's theorem.*** *Let $f : \mathbb{R}^d \to [0, +\infty)$ be a measurable function, then:*

$$\mathbb{E}_{\mathbb{P}}\left\{\sum_{x\in\Phi} f(x)\right\} = \int_{\mathbb{R}^d} f(x)\Lambda(\mathrm{d}x) \tag{A.13}$$

Proof. Interpreting Φ as the counting measure, the sum over the Point Process is given by:

$$\sum_{x\in\Phi} f(x) = \int_{\mathbb{R}^d} f(x)\Phi(\mathrm{d}x)$$

and taking the average on both sides:

$$\begin{aligned}
\mathbb{E}_{\mathbb{P}}\left\{\sum_{x\in\Phi} f(x)\right\} &= \mathbb{E}_{\mathbb{P}}\left\{\int_{\mathbb{R}^d} f(x)\Phi(\mathrm{d}x)\right\} \\
&\overset{(a)}{=} \int_{\mathsf{S}}\int_{\mathbb{R}^d} f(x)\phi(\mathrm{d}x)\mathbb{P}(\mathrm{d}\phi) \\
&\overset{(b)}{=} \int_{\mathbb{R}^d} f(x)\int_{\mathsf{S}} \phi(\mathrm{d}x)\mathbb{P}(\mathrm{d}\phi) \\
&\overset{(c)}{=} \int_{\mathbb{R}^d} f(x)\mathbb{E}_{\mathbb{P}}\left\{\Phi(\mathrm{d}x)\right\} \\
&\overset{(d)}{=} \int_{\mathbb{R}^d} f(x)\Lambda(\mathrm{d}x)
\end{aligned}$$

where (a) is the average written as a function of the distribution of the PPP, integrating over the set of point sequences; (b) results by switching the integration order (which is essentially an application of Fubini's theorem); (c) follows by rewriting the inner integral as an expectation (which is the inverse step of (a)); and (d) follows from the definition of density measure. □

Appendix B

Stable Distributions

In this Appendix, some information on Stable distributions are provided. For further detail, the reader might refer to [58]. Stable distributions are a direct generalization of Gaussian distributions, and include other probability density functions with heavier tails. They share many properties with Gaussian distributions, like the stability property and the generalized central limit theorem. A stable random variable is defined as follows:

Definition B.1. Let X_1 and X_2 be two independent copies of a random variable X. X is said to be *stable* if for some $a, b, c \in (0, \infty)$ and $d \in \mathbb{R}$:

$$a\mathrm{X}_1 + b\mathrm{X}_2 = c\mathrm{X} + d \tag{B.1}$$

The only known stable distributions with closed-form probability density functions are the Gaussian, the Cauchy and the Lévy (see Section 1.4) distributions. The characteristic function of a stable random variable is given by:

$$\mathbb{E}_{\mathrm{X}}\left\{e^{jtx}\right\} = \begin{cases} \exp\left[jt\mu - \gamma|t|^{\delta}\left(1 - \beta\mathrm{sign}(t)\tan\left(\frac{\pi\delta}{2}\right)\right)\right], & \delta \neq 1 \\ \exp\left[jt\mu - \gamma|t|^{\delta}\left(1 + j\frac{2\beta}{\pi}\mathrm{sign}(t)\log\left(|t|\right)\right)\right], & \delta = 1 \end{cases} \tag{B.2}$$

where

- $\mu \in \mathbb{R}$ is the *location parameter* or *center*;

- $\beta \in [-1, 1]$ is the *skew parameter*. The cases where $\beta < 0, \beta = 0, \beta > 0$ correspond to a pdf which is skewed to the left, symmetric around the center μ, and skewed to the right respectively;

- $\gamma \in [0, \infty)$ is the *dispersion parameter*, which has the same meaning as the variance;

- $\delta \in (0, 2]$ is the *characteristic exponent*, and controls the heaviness of the pdf tail. If $\delta = 2$, then $\mathrm{X} \sim \mathcal{N}(\mu, 2\gamma)$. Moreover, the p-th moment of X with $\delta < 2$ is finite if and only if $p < \delta$.

According to the above parameters, a stable random variable is denoted as $\mathrm{X} \sim \mathcal{S}(\delta, \beta, \gamma, \mu)$. When $\beta = \mu = 0$, X is said to be *Symmetric Stable*. Furthermore, if $\mathbf{X}$ is a Complex stable random variable, it is said to belong to a *Spherically Symmetric (SS) Stable distribution*, whose characteristic function is $\mathbb{E}_{\mathbf{X}}\left\{e^{jt\mathbf{X}}\right\} = \exp\left(-\gamma|\mathbf{x}|^{\delta}\right)$. It is also worthwhile noting that in this case, each component of $\mathbf{X}$ is distributed as a stable distribution $\mathcal{S}(\delta, 0, \gamma)$.
Two useful properties of Stable distributions are listed below:

- *Scaling*: let $\mathrm{X} \sim \mathcal{S}(\delta, \beta, \gamma, 0) = \mathcal{S}(\delta, \beta, \gamma)$ with $\delta \neq 1$, and let k be a non-zero real constant. Then:
$$k\mathrm{X} \sim \mathcal{S}(\delta, \mathrm{sign}(k)\beta, |k|^{\delta}, \gamma) \tag{B.3}$$

- *Decomposition*: let $\mathrm{X} \sim \mathcal{S}(\delta, 0, \gamma)$. Then X can be decomposed as:
$$\mathrm{X} = \sqrt{\mathrm{V}}\mathrm{G} \tag{B.4}$$
where $\mathrm{V} \sim \mathcal{S}\left(\frac{\delta}{2}, 1, \cos\left(\frac{\pi\delta}{4}\right)\right)$ and $\mathrm{G} \sim \mathcal{N}\left(0, 2\gamma^{2/\delta}\right)$. In addition, V and G are two independent random variables.

When $\delta < 1$ and $\beta = 1$, which is the case encountered in Section 1.4 for the aggregate interference power, X can be described by means of its Laplace transform, which is given by:
$$\mathcal{L}_{\mathrm{X}}(s) = \mathbb{E}_{\mathrm{X}}\left\{e^{-s\mathrm{X}}\right\} = \exp\left[-\frac{\gamma s^{\delta}}{\cos\left(\frac{\pi\delta}{2}\right)}\right] \tag{B.5}$$

Appendix C

Cognitive Radio Fundamentals

In this Appendix, the main aspects of Cognitive Radios (CRs) are described, together with the main challenges to be coped with for their proper implementation. For further details, the reader might refer to [88, 99–101].

C.1 Definition

In order to meet the spectrum resource demands, due to the increasing request for multimedia wireless communications, both regulatory bodies and administrations are expanding the unlicensed usage of spectrum through *Dynamic Spectrum Access* (DSA) techniques. These techniques allow a device to adaptively and dynamically transmit and receive data, modifying their operating behaviour according to the varying wireless environment, and thus allow to exploit the temporarily/locally unused spectrum resources. These available resources are the so called *spectrum holes* [87], an example of which is shown in Figure C.1.

Among all the possible technologies proposed with this intent, Cognitive Radios, introduced for the first time in [62], are probably the most known. Many definitions have been proposed for this novel communication paradigm, and not all of them in agreement with each other [87, 99–102]. In order to provide a clear and common understanding of this novel technology, the first standard published by IEEE on CRs, IEEE Std. 1900.1, lists all the definitions of concepts related to CRs and flexible spectrum usage [103]. Thus, in the following, the adopted definition is that provided by IEEE, according to which a Cognitive Radio is "*a type of radio in which communication systems are aware of their environment and internal state and can make decisions about their radio operating behavior based on that information and*

predefined objectives." In the most simple case, this implies that CRs shall at least have the following capabilities [88]:

- detect the spectrum holes and analyze them in order to select the best frequencies to meet specific user communication requirements and spectrum regulatory policies;
- access the identified spectrum resources without generating harmful interference towards the Primary Users (PUs), *i.e.* the licensed users;
- share the spectrum holes in an efficient and fair manner with other CR devices/networks.

It is worthwhile highlighting the importance of the second "cognitive capability": CR devices/networks are allowed to access licensed spectrum bands in an opportunistic (dynamic) way *if and only if* they do not cause harmful interference to the users of the licensed service on that band, which obviously have the priority to utilize it.

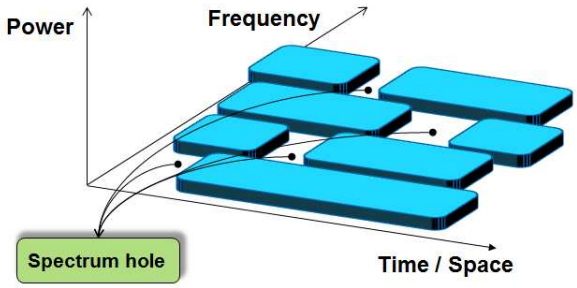

Figure C.1: Spectrum hole.

C.2 Cognitive Network Architecture

The components of a Cognitive Network are typically classified in two subnetworks: the primary network and the cognitive (or secondary) network, as depicted in Figure C.2 [88]. The former is a network infrastructure with exclusive right to use the considered frequency bands, *e.g.* the DVB-T signal between 470 MHz and 790 MHz. This network is composed by PUs, who shall not be affected at any level by the operation of the secondary network, and the Primary BSs, which represent any fixed infrastructure component providing the connection to the PUs. It is worthwhile noting that the primary BSs might have the capability to communicate with CRs, as an optional feature. On the other hand, the secondary/cognitive network

does not have the license to access the intended spectrum bands, and it thus has to operate in a dynamic manner. This network can be either infrastructure-less or with infrastructure, and its components can be usually classified into: (i) Secondary Users (SUs); (ii) Cognitive BSs or Access Points (APs), which provide opportunistic single-hop connections to the SUs; and (iii) a spectrum broker, a central entity that acts as a spectrum manager (provides information on the spectrum occupancy, or even takes decisions and communicates them to the SUs/secondary BSs). Please note that the presence of a Spectrum Broker is optional, depending on the level of centralization according to which the secondary network shall be managed.
According to the depicted network architecture, the cognitive users might access the spectrum according to the three following categories:

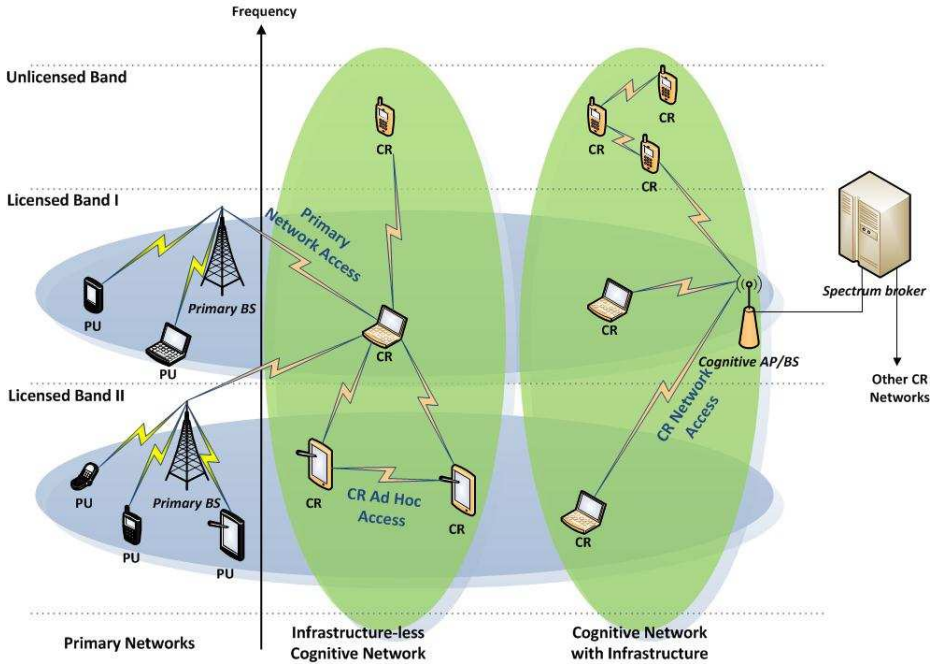

Figure C.2: Cognitive network architecture.

- *Primary Network Access*: CRs access the primary BSs on the licensed band, basically acting as Primary Users;

- *CR/Secondary Network Access*: CRs access their own BSs/APs, both on licensed and unlicensed bands. In this case the network coordinator, a role played either by the BS or by the Spectrum Broker, needs to know the spectrum occupancy and is in charge of creating/managing the secondary network;

- *CR Ad Hoc Access*: CRs communicate among them without an infrastructure, both on licensed and unlicensed bands. According to these paradigm, CRs are responsible of monitoring the spectrum and take appropriate decisions on opportunistic spectrum access.

Different requirements have to be met by the CRs according to the spectrum they would like to access. In particular, if the intent is to access unlicensed spectrum bands, all the network entities have the same right to access the spectrum, and thus efficient and fair contention-based spectrum management protocols and algorithms have to be implemented. On the other hand, if the CRs are willing to access licensed spectrum bands, tha main requirements is that of accurately detecting the presence of PUs, as avoiding interference towards primary services is the main aspect. Moreover, if a PU requests a band which is currently being used by a CR, the last one has to immediately release it and change operating frequency.

C.3 The Cognitive Cycle

The major functions of a Cognitive Radio, which permit to meet the requirements listed in the previous sections, can be represented as a *cognitive cycle* [62, 88, 101], as shown in Figure C.3. The functional blocks of the cognitive cycle satisfy the following tasks:

- *spectrum monitoring*: the aim of this block is to periodically monitor the spectrum bands, in order to determine the status of the spectrum and to identify the eventually available spectrum holes. The main goal to be achieved is that of ensuring that the transmission of PUs is not interfered by unlicensed spectrum access;

- *spectrum analysis*: by using the report provided by the spectrum monitoring engine, the spectrum analyzer schedules and plans proper spectrum access for the unlicensed users. During spectrum analysis, several characteristics are estimated in order to have the most complete knowledge on spectrum holes as possible before making any decision, *e.g.* interference level, expected availability time, attenuation, etc. Finally, thanks to this knowledge and monitoring reports, and by taking into account the available information on user requirements and spectrum regulatory policies, the spectrum analyzer makes optimal decisions on spectrum access. Different techniques can be used to find the

optimal solution. For instance, optimization theory might be used when the system can be modeled as a single entity with a single objective, whereas game theory principles might be applied when the system is composed by multiple entities, each one with its own objective;

- *spectrum access*: after the decision on the spectrum bands to be used is made, these available resources are accessed by the unlicensed users. This operation is performed by the spectrum access block, which basically acts as a cognitive Medium Access Control (MAC) layer. In particular, the main goal is not only that of avoiding collisions with Primary Users, but with other unlicensed users as well, as CRs are supposed to efficiently share the spectrum holes;

- *reconfiguration*: finally, the only operation which is left is the reconfiguration of the cognitive device. In particular, the reconfiguration can be performed not only at the beginning of a transmission, but also during the transmission. As a matter of facts, a PU might request the channel used by the CR, and thus it has to switch to another vacant band (the so called *spectrum handoff*), or the user's requirements might need a change in the transmission protocol. All these operations must be performed seamlessly to the unlicensed users.

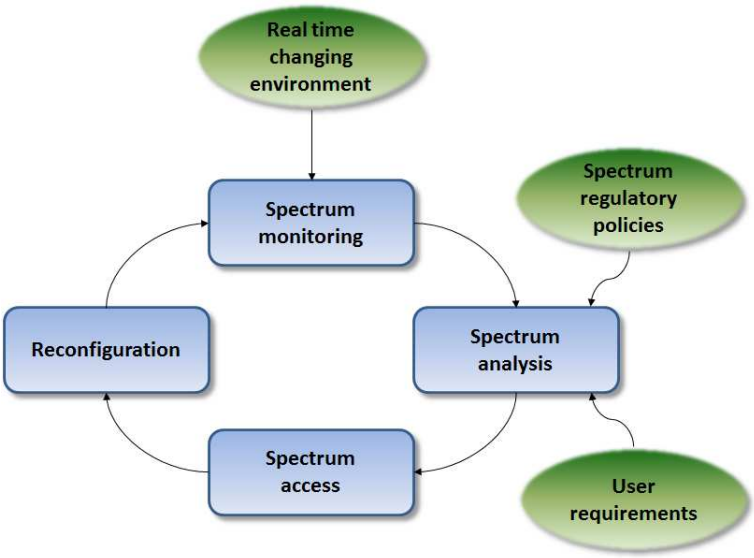

Figure C.3: Cognitive cycle.

C.4 Main Cognitive Features

In this section, the main features, capabilities and challenges for the realization of proper DSA through Cognitive Radios are depicted, according to the functional blocks of the cognitive cycle previously described.

Monitoring

The goal of this block is to monitor the spectrum bands and identify the eventually available spectrum holes, in order to provide a complete report to the spectrum analyzer. Most of the spectrum monitoring techniques can be categorized as: (i) single-device sensing; (ii) cooperative sensing; (iii) interference-based sensing; and (iv) geolocation database-based sensing.

Single-device sensing

In this case, the CR autonomously monitors the spectrum in order to understand whether a PU is present or not. The common model for such detection problem is as follows [104]:

$$r(t) = \begin{cases} n(t), & H_0 \\ h \cdot s(t) + n(t), & H_1 \end{cases} \tag{C.1}$$

where $r(t)$ is the received signal at the CR front-end, $s(t)$ is the eventually transmitted PU signal, h the channel gain, and $n(t)$ the AWGN. Furthermore, H_0 and H_1 denote the absence or presence of the PU transmission respectively. Typically, the performance of sensing techniques is evaluated in terms of Probability of Correct Detection (P_D) and probability of False Alarm (P_{FA}), which are defined respectively as the probability of correctly detect a PU signal assuming it is present ($\mathbb{P}\{\widehat{H}_1|H_1\}$), and the probability of detecting the presence of a PU signal when it is not present ($\mathbb{P}\{\widehat{H}_1|H_0\}$).
During the last years, an outstanding number of techniques have been proposed in order to perform efficient single-device sensing [105]. However, almost all of these techniques can be basically summarized according to the following methods:

- *Matched Filter/Coherent Detection*: when the information on the PU signal is known, the optimal detector is given by the matched filter [106], since it maximizes the received SNR [107]. Since this technique consists in comparing the received signal with a known template at the CR (coherent detection), the

detection requires less time. However, this technique requires the knowledge of the PU signal, such as modulation type, packet format, etc., which is not likely to be available for a CR;

- *Energy Detection*: if the CR does not have sufficient information on the PU signal, the simplest solution is to realize an energy detector [91–93]: this detector basically treats the PU signal as noise, and decides on the presence or absence of a PU based on the energy of the observed signal. This technique does not need *a priori* knowledge, and thus it is robust to the variation of the PU signal. Furthermore, the computational complexity is limited. However, this detector is highly susceptible to uncertainty in noise power, as a particularly high level of noise might easily lead to false alarm, and it is not able to discern among signal types, with the false alarm being led by secondary transmissions as well;

- *Cyclostationary Feature Detection*: this detector exploits the implicit periodicity of modulated signals, which is given by sine carriers, pulse trains, hopping sequences, cyclic prefixes, etc., by analyzing the periodicity of their mean and autocorrelation, the so called cyclostationarity [108,109]. Such a periodic pattern allows to distinguish the PU signal from noise, which is a wide-sense stationary signal with no correlation. Moreover, this approach also allows to discern among the different modulated signals, thus permitting to distinguish between primary and secondary transmissions. The disadvantage of this technique is that it requires long observation periods, and the detection is quite complex.

Cooperative Sensing

Multipath fading and shadowing pose a major challenge for proper spectrum sensing. If the primary signal is deeply faded or even blocked by large obstacles in the environment (the so called *Hidden Node problem*), the power of the primary signal at the CR might be too weak to be detected. In order to improve the performance in these situations, the CRs might be allowed to cooperate [104,110–112]. Such cooperation allows to exploit the spatial diversity in Cognitive networks, improving the performance of spectrum sensing. Cooperative spectrum sensing can be either centralized, *i.e.* there is a central network entity which collects the sensed data and then informs the CRs about the spectrum occupancy, or distributed, *i.e.* the CRs communicate

among them and decide on the presence or absence of primary signals without a centralized control. As for single-device sensing, many techniques have been proposed for proper cooperation among CRs. In particular, it was demonstrated that cooperation improves the detection performance [104], relax the sensitivity requirements [113], and decrease the required detection time [114, 115].
While cooperative sensing provides the above benefits, it also poses several challenges. Firstly, the communication among CRs, or between CRs and the central entity, introduces additional operations and traffic overhead, which is particularly problematic in resource-constrained networks. Moreover, the hidden node problem, due to the unknown location of the PUs, is still unsolved.

Interference-based Sensing

According to this approach, proposed by FCC in [96], the CR shall sense the noise plus interference level from all sources of signals at the primary receiver. This information, and the choice of a proper interference limit level at the PU, would lead to the selection of a transmission power that does not generate harmful interference at the primary receiver[1]. Unlike the traditional transmitter-centric approach, this technique allows to manage the interference at the receiver, which actually is the location where it occurs. Though such approach seems attractive, it has a strong limitation: the location of the PUs is unknown, and thus it is not possible to evaluate the interference level generated by CRs at the front-end. Further details on this technique can be found in [116, 117].

Geolocation Database

With geolocation database-based sensing, the CR determines its location and accesses a database containing several information for not causing harmful interference. In its simplest implementation, this information consists in which frequencies can be used at its location, and the transmission power limits to be respected. Higher level databases might store more detailed information on dynamic spectrum access, like the codes to be used in the presence of CDMA-based primary system, or information depending on the primary traffic pattern. This approach is based on accurate position estimation by the CR, and on its tracking while the CR moves, and an

[1]This approach leads to the so called *underlay* spectrum sharing: a CR transmits as long as its transmission is seen as noise by the licensed users. In *overlay* spectrum sharing, a CR access a licensed band which is not used by PUs.

inaccurate estimation of these location would have severe impact on the protected services. Moreover, this approach should be implemented for indoor usage as well, and this poses severe challenges for the CR localization.

Before concluding this section, some comments are worth being made. At the beginning of their activities, most of the regulatory and standardization bodies were interested in single-device sensing, thus focusing their efforts on accurate primary signal detection for a single CR. After realizing that this approach would have not led to significant results, due to current state-of-the-art technologies, the attention was turned on cooperative sensing and geolocation databases. In particular, as also stated by several administrations[2], cooperative detection is the best solution in the long term, while from a medium term point of view geolocation databases are the optimal approach, as they can already be realized. Of course, the implementation of a geolocation database poses some important, and barely technical, challenges, like the decision on which body should be in charge of collecting the spectrum occupancy information and on its protection: from an operator point of view, the information on its spectrum utilization is extremely valuable, and making it available for competitors would have deep economical consequences.

Analysis

The available spectrum holes identified by the spectrum monitor show different characteristics, which may also vary over time. The aim of the spectrum analyzer is that of providing a complete estimation of these characteristics to the spectrum decision engine, in order to perform a proper opportunistic access to licensed bands, and/or to fairly share the spectrum resources with other CRs. Apart from operating frequency and bandwidth, other important parameters to be estimated might be the following:

- interference: the interference level of certain bands is higher with respect to less used ones. This affects the maximum allowed transmission power for a CR, or the overall power to be used by several CRs, which provides the channel capacity that might be reached;
- path-loss: according to the operating frequency, the path-loss changes if the transmission power is kept fixed. Increased propagation distances provide a

[2]For instance, UK Office of Communication (Ofcom) in [118].

better secondary coverage, but might also let the CRs to interfere with primary services deployed on adjacent areas. It is worthwhile noting that a CR might decide to use a lower frequency in order to limit its interference range;

- link layer delay: to address different path-loss and interference, different protocols are required depending on the spectrum band. This results in different delays, and according to the users' requirements, proper evaluation of this delay is needed;

- holding time: the expected availability time of a licensed spectrum band for secondary transmission is a crucial parameter. By selecting a band which is less likely to be requested by a PU (*i.e.* higher holding time), a CR reduces the spectrum handoffs to be performed, thus preserving battery life and providing a better service to the user.

As the quality of the available spectrum is the fundamental aspect for this engine, learning algorithms (*e.g.* neural networks, swarm intelligence algorithms, genetic algorithms, etc.) seem to be the most appropriate candidates for accurate spectrum analysis, as they allow to iteratively reduce the estimation errors.

Access

This block deals with whether to transmit or not, taking into account also the fact that spectrum sensing report might be erroneous. Moreover, in case of transmission, this block also has to decide how to access the available spectrum bands. Thus, spectrum access decisions are basically optimization problems, which take into account not only the information gathered by the other blocks, but also user requirements, regulatory policies, and the transmission parameters to be used (*e.g.* modulation, subcarrier in OFDM-based systems, pulse shaping, etc.). This optimization can be performed according to the following approaches:

- *local optimization*: each CR is responsible for its own decision, without considering the consequences of this decision on other CRs. This approach has negligible communication requirements, and thus a low overhead. However, this might also result in a poor spectrum re-utilization;

- *centralized cooperative optimization*: a central server stores information on spectrum availability and access, providing coordinated spectrum sharing to the CRs;

- *distributed cooperative optimization*: this strategy relies on local actions taken by the CRs in order to optimize the spectrum re-utilization. This approach is particularly prone to hidden node problems and traffic overhead, due to control communications.

Of course, the main challenge in spectrum decision is the decision model, with both its accuracy and complexity being directly proportional to the number of parameters to be taken into account. Furthermore, in cooperative scenarios, the preferences of all the secondary users (and that of the primary ones, if they cooperate as well), affects the spectrum decision, and thus the complexity of the optimization problem to be solved considerably increases with the number of cooperating devices. Obviously, increasing this number provides better solutions. Another challenge is related to multiple band decision: CRs might use multiple bands for transmission, and these bands to not necessarily need to be adjacent. Thus, the above challenges related to a single spectrum band have to be considered in this multiple band scenario.

Reconfiguration

The reconfiguration block aims at efficiently change the operating parameters according to the decisions taken by the previous engines. Moreover, the required operations must be performed seamlessly to the user. The main challenge in the reconfiguration process is the so called spectrum handoff, *i.e.* switching between available frequency bands to provide smooth spectrum access without interruption to both application and service due to changes in the radio environment (as the arrival of a PU). With this aim, the CR has to continuously monitor the spectrum band, either on demand (*i.e.* when there is the need to switch frequency) or in a proactive manner (which reduces the latency, but increases the computational overhead) [119]. A very important challenge to be coped with is given by the synchronization between the secondary transmitter and receiver: when the CR needs to change operating frequency, its intended receiver must be notified as soon as possible. When there is not a Spectrum Broker as that depicted in Figure C.2, this challenge becomes crucial.

Conclusions

This thesis has addressed several spectrum management challenges and the introduction of Cognitive Radio systems in both terrestrial and satellite systems.

In the first part, the network interference generated by a cognitive network has been characterized by means of Poisson Point Process theory. In Chapter 1, the MGF of the aggregate interference power was obtained in closed-form for Rayleigh, Nakagami-m and non fading channel for several network configurations. This allowed to derive a closed-form of the coverage probability and a single-integral expression of the average achievable rate in Chapter 2 and Chapter 3 respectively. In Chapter 4, which concludes Part I, a simple single-integral expression of the ASEP for both synchronous and asynchronous networks has been computed. All these mathematical frameworks have been extensively substantiated through Monte Carlo simulations.

The second part has mainly dealt with regulatory aspects related to Cognitive Radio systems and coexistence challenges between mobile and broadcasting systems. In Chapter 5, a versatile methodology allowing to take into account the mutual co-channel interference between these two systems has been described. Moreover, the advantages of using the 800 MHz band have been provided. In Chapter 6, the amount of spectrum potentially available as white space has been estimated in the Italian region of West Piedmont, showing that most of the opportunities for DSA are actually in rural areas. Furthermore, the Hidden Node Margin has been characterized in real scenarios, analyzing its dependence on topological parameters, namely the street width and the rooftop diffraction angle. Finally, in Chapter 7, cognitive functionalities have been introduced in a hybrid satellite-terrestrial system, and a novel 3rd dimension, the elevation angle, has been exploited for better detection of primary terrestrial transmitters.

Personal Contributions

[1] A. Guidotti, M. Di Renzo, G. E. Corazza, and F. Santucci, "Simplified Expression of Coverage Probability and Average Rate of Cellular Networks Using Stochastic Geometry," *IEEE Transactions on Communications (to be submitted)*, 2012.

[2] A. Guidotti, M. Di Renzo, G. E. Corazza, and F. Santucci, "Simplified Expression of the Average Rate of Cellular Networks Using Stochastic Geometry," *IEEE International Conference on Communication 2012 (ICC 2012) (submitted)*, June 2012.

[3] C. Merola, A. Guidotti, M. Di Renzo, F. Santucci, and G. E. Corazza, "Average Symbol Error Probability in the Presence of Network Interference and Noise," *IEEE International Conference on Communication 2012 (ICC 2012) (submitted)*, June 2012.

[4] A. Guidotti, D. Guiducci, M. Barbiroli, C. Carciofi, P. Grazioso, and G. Riva, "Coexistence and Mutual Interference between Mobile and Broadcasting Systems," *IEEE Vehicular Technology Conference - Spring 2011 (VTC Spring 2011)*, May 2011.

[5] A. Guidotti, P. Grazioso, M. Barbiroli, C. Carciofi, D. Guiducci, and G. Riva, "Analysis of coexistence and mutual interference between mobile and digital television systems," *Systemas y Telematica (S&T)*, vol. 9, no. 19, pp. 9–30, October 2010.

[6] M. Barbiroli, A. Guidotti, P. Grazioso, and G. Riva, "Coexistence and mutual interference between mobile radio and broadcast systems - Preliminary simulation results," *COST 2100 TD(09)709*, February 2009.

[7] "WRC-12 AI 1.17 - Broadcasting versus mobile: theoretical analysis of mutual interference," Tech. Rep. CPGPTD(10)109, Italian Contribution to CPG PT-D - Agenda Item 1.17, Aug. 2010.

[8] "WRC-12 AI 1.17 - Options for method A1," Tech. Rep. CPGPTD(10)156, Italian Contribution to CPG PT-D - Agenda Item 1.17, Aug. 2010.

[9] "WRC-12 AI 1.17 - Options for method A1," Tech. Rep. CPGPTD(11)33, Italian Contribution to CPG PT-D - Agenda Item 1.17, Aug. 2011.

[10] M. Barbiroli, C. Carciofi, D. Guiducci, A. Guidotti, E. Tarantino, and G. Riva, "Advantages and disadvantages of the introduction of IMT systems in the 800 MHz band," *International Conference on Electromagnetics in Advanced Applications 2011 (ICEAA 2011)*, September 2010.

[11] "Availability of spectrum for white space devices in the band 470-790 MHz," Tech. Rep. SE43(10)22, Italian Contribution to CEPT SE43, Jan. 2010.

[12] "Calculation of the Hidden Node Margin in a real Italian scenario," Tech. Rep. SE43(10)123, Italian Contribution to CEPT SE43, Aug. 2010.

[13] M. Barbiroli, C. Carciofi, A. Guidotti, and D. Guiducci, "Evaluation and Analysis of the Hidden Node Margin for Cognitive Radio System Operation in a Real Scenario," *European Conference on Antennas and Propagation 2011 (EuCAP 2011)*, April 2011.

[14] S. Kandeepan, L. De Nardis, M.-G. Di Benedetto, A. Guidotti, and G. E. Corazza, "Cognitive Satellite Terrestrial Radios," *IEEE Global Communications Conference (GLOBECOM 2010)*, December 2010.

[15] "Enforcement issues related to the geolocation database approach," Tech. Rep. SE43(10)96, Italian Contribution to CEPT SE43, Jun. 2010.

[16] "Translation of the information provided to the geolocation database into elements of authorisation to the WSD," Tech. Rep. SE43(10)124, Italian Contribution to CEPT SE43, Aug. 2010.

[17] "Proposal of an application methodology to combine geo-location database and sensing," Tech. Rep. SE43(11)38, Italian Contribution to CEPT SE43, Jul. 2011.

[18] "Performance analysis of cooperative energy detection sensing," Tech. Rep. SE43(11)37, Italian Contribution to CEPT SE43, Jul. 2011.

[19] "Feasibility of autonomous operation of WSDs using sensing," Tech. Rep. SE43(11)62, Italian Contribution to CEPT SE43, Sep. 2011.

[20] "Consideration of coexistence between WSD and TETRA," Tech. Rep. SE43(11)39, Italian Contribution to CEPT SE43, Jul. 2011.

[21] R. Suffritti, G. E. Corazza, A. Guidotti, V. Petrini, D. Tarchi, A. Vanelli-Coralli, and M. Di Renzo, "Cognitive hybrid satellite-terrestrial systems," *International Conference on Cognitive Radio and Advanced Spectrum Management 2011 (CogART 2011)*, October 2011.

Bibliography

[22] J. G. Andrews, F. Baccelli, and R. K. Ganti, "A tractable approach to coverage and rate in cellular networks," *IEEE Transactions on Commununications (submitted)*, February 2010. [Online]. Available at: http://arxiv.org/abs/1009.0516.

[23] M. Z. Win, P. C. Pinto, and L. A. Shepp, "A Mathematical Theory of Network Interference and its Applications," *Proceedings of the IEEE*, vol. 97, no. 2, pp. 205–230, February 2009.

[24] M. Haenggi and R. K. Ganti, *Interference in Large Wireless Networks*, Foundations and Trends in Networking, 2009.

[25] J. G. Andrews, R. K. Ganti, M. Haenggi, N. Jindal, and S. Weber, "A primer on spatial modeling and analysis in wireless networks," *IEEE Communications Magazine*, vol. 48, no. 11, pp. 156–163, November 2010.

[26] F. Baccelli and Blaszczyszyn, *Stochastic Geometry and Wireless Networks, Part I: Theory, Part II: Applications*, Now Publishers, 2009.

[27] J. Venkataraman, M. Haenggi, and O. Collins, "Shot Noise models for outage and throughput analyses in Wireless Ad Hoc Networks," *IEEE Military Communications Conference 2006 (MILCOM 2006)*, October 2006.

[28] A. Ghasemi and E. S. Sousa, "Interference aggregation in spectrum sensing cognitive wireless networks," *IEEE Journal on Selected Topics in Signal Processing*, vol. 2, no. 1, pp. 41–56, February 2008.

[29] A. Rabacchin, T. Q. S. Quek, H. Shin, and M. Z. Win, "Cognitive Network Interference," *IEEE Journal on Selected Areas in Communications*, vol. 29, no. 2, pp. 480–493, February 2011.

[30] E. Salbaroli and A. Zanella, "Interference analysis in a Poisson field of nodes of finite area," *IEEE Transactions on Vehicular Technology*, vol. 58, no. 4, pp. 1776–1783, May 2009.

[31] S. Srinivasa, *Modeling interference in uniformly random Wireless Networks: theory and applications*, Master degree thesis, University of Notre Dame, Indiana (US), December 2007.

[32] S. Weber and M. Kam, "Computational complexity of outage probability simulations in mobile ad hoc networks," *Conference on Information Sciences and Systems 2005 (CISS'05)*, March 2005.

[33] K. Gulati, B. L. Evans, J. G. Andrews, and K. R. Tinsley, "Statistics of Co-Channel Interference in a Field of Poisson and Poisson-Poisson Clustered Interferers ," *IEEE Transactions on Signal Processing*, vol. 58, no. 12, pp. 6207–6222, December 2010.

[34] R. K. Ganti and M. Haenggi, "Interference and outage in clustered wireless ad hoc networks," *IEEE Transactions on Information Theory*, vol. 55, no. 9, pp. 4067–4086, September 2009.

[35] T. M. Apostol, *Mathematical Analysis*, Addison-Wesley, Reading, 2nd ed., 1974.

[36] M. K. Simon and M.-S. Alouini, *Digital Communication over Fading Channels*, John Wiley & Sons, Inc., 1st ed., 2000.

[37] S. B. Lowen and M. C. Teich, "Power-law Shot Noise," *IEEE Transactions on Information Theory*, vol. 36, no. 6, pp. 1302–1318, November 1990.

[38] M. Abramowitz and I. A. Stegun, *Handbook of Mathematical Functions with Formulas, Graphs, and Mathematical Tables*, National Bureau of Standards, 1964.

[39] Y.-C. Ko, M.-S. Alouini, and M. Simon, "Outage probability of diversity systems over generalized fading channels," *IEEE Transactions on Commununications*, vol. 48, no. 11, pp. 1783–1787, November 2000.

[40] I. S. Gradshteyn and I. M. Ryzhik, *Table of Integrals, Series, and Products*, Academic Press, 5th ed., 1994.

[41] A. Erdélyi, W. Magnus, F. Oberhettinger, and F. G. Tricomi, *Higher Trascendental Functions*, McGraw-Hill Book Company, Inc., 1953.

[42] A. P. Prudnikov, Yu. A. Brychkov, and O. I. Marichev, *Integrals and Series - Vol. 3: More Special Functions*, ISBN 5-9221-0325-3, 2003.

[43] M. Di Renzo, F. Graziosi, and F. Santucci, "Channel capacity over generalized fading channels: A novel MGF-based approach for performance analysis and design of wireless communication systems," *IEEE Transactions on Vehicular Technologies*, vol. 59, no. 1, pp. 127–149, January 2010.

[44] F. Yilmaz and M.-S. Alouini, "A unified MGF-based capacity analysis of diversity combiners over generalized fading channels," *IEEE Transactions on Commununications (submitted)*, December 2010. [Online]. Available at: http://arxiv.org/abs/1012.2569.

[45] M. Di Renzo, F. Graziosi, and F. Santucci, "A unified framework for performance analysis of CSI-assisted cooperative communications over fading channels," *IEEE Transactions on Commununications*, vol. 57, no. 9, pp. 2552–2557, September 2009.

[46] M. Di Renzo, F. Graziosi, and F. Santucci, "A comprehensive framework for performance analysis of dual-hop cooperative wireless systems with fixed gain relays over generalized fading channels," *IEEE Transactions on Wireless Communications*, vol. 8, no. 10, pp. 5060–5074, October 2009.

[47] A. M. Mathai and R. K. Saxena, *Generalized Hypergeometric Functions with Applications in Statistics and Physical Sciences*, Lecture Notes in Mathematics, vol. 348, Springer-Verlang, 1973.

[48] K. A. Hamdi, "Capacity of MRC on correlated Rician fading channels," *IEEE Transactions on Commununications*, vol. 56, no. 5, pp. 708–711, May 2008.

[49] K. A. Hamdi, "A useful lemma for capacity analysis of fading interference channels," *IEEE Transactions on Commununications*, vol. 58, no. 2, pp. 411–416, February 2010.

[50] S. Ambike, J. Ilow, and D. Hatzinakos, "Detection for binary transmission in a mixture of gaussian noise and impulsive noise modeled as an alpha-stable process," *IEEE Signal Processing Letters*, vol. 1, no. 3, pp. 55–57, March 1994.

[51] G. A. Tsihrintzis and C. L. Nikias, "Performance of optimum and suboptimum receivers in the presence of impulsive noise modeled as an alpha-stable process," *IEEE Transactions on Commununications*, vol. 43, no. 2/3/4, pp. 904–914, Feb./Mar./Apr. 1995.

[52] Y. Shobowale and K. A. Hamdi, "A unified model for interference analysis in unlicensed frequency bands," *IEEE Transactions on Wireless Commununications*, vol. 8, no. 8, pp. 4004–4013, August 2009.

[53] P. C. Pinto and M. Z. Win, "Communication in a Poisson field of interferers - Part I: Interference distribution and error probability," *IEEE Transactions on Wireless Commununications*, vol. 9, no. 7, pp. 2176–2186, July 2010.

[54] S. Niranjayan and N. C. Beaulieu, "The BER optimal linear rake receiver for signal detection in symmetric alpha-stable noise," *IEEE Transactions on Commununications*, vol. 57, no. 12, pp. 3585–3588, December 2009.

[55] S. Niranjayan and N. C. Beaulieu, "BER optimal linear combiner for signal detection in symmetric alpha-stable noise: Small values of alpha," *IEEE Transactions on Wireless Commununications*, vol. 9, no. 3, pp. 886–890, March 2010.

[56] J. Lee and C. Tepedelenlioglu, "Space-time coding over fading channels with stable noise," *IEEE Transactions on Wireless Commununications (to appear)*, February 2010. [Online]. Available at: http://arxiv.org/abs/1102.3392.

[57] A. Rajan and C. Tepedelenlioglu, "Diversity combining over Rayleigh fading channels with symmetric alpha stable noise," *IEEE Transactions on Wireless Commununications*, vol. 9, no. 9, pp. 2968–2976, September 2010.

[58] G. Samorodnitsky and M. S. Taqqu, *Stable Non Gaussian Random Processes: Stochastic Models with Infinite Variance*, Chapman & Hall/CRC, 1994.

[59] M. Di Renzo, F. Graziosi, and F. Santucci, "Further results on the approximation of log-normal power sum via Pearson type IV distribution: A general formula for log-moments computation," *IEEE Transactions on Communications*, vol. 57, no. 4, pp. 893–898, April 2009.

[60] M. Di Renzo and H. Haas, "A general framework for performance analysis of space shift keying (SSK) modulation for MISO correlated Nakagami-m fading

channels," *IEEE Transactions on Communications*, vol. 58, no. 9, pp. 2590–2603, September 2010.

[61] "Notice of proposed rule making and order," Tech. Rep. FCC ET Docket no. 03-222, Federal Communications Commission, Dec. 2003.

[62] J. Mitola and G. Q. Maguire, "Cognitive radios: making software radios more personal," *IEEE Personal Communications*, vol. 6, no. 4, pp. 12–18, August 1999.

[63] "Opinion of the RSC pursuant to Article 4.2 of Radio Spectrum Decision 676/2002/EC," Tech. Rep. RSCOM08-06final, European Commission - Information Society and Media Directorate-General, Radio Spectrum Committee (DG-INFSO), Apr. 2008.

[64] 3GPP TR 36.942 v8.1.0 (2008-12), *Evolved Universal Terrestrial Radio Access (E-UTRA); Radio Frequency (RF) system scenarios; (Release 8)*, Dec. 2008.

[65] K. Šakić, M. Gosta, and S. Grgić, "Cross-border interference between broadcasting and mobile services," *IEEE Conference on Electronics in Marine 2009 (ELMAR 2009)*, September 2009.

[66] "WRC-12 AI 1.17 - Broadcasting versus mobile: cumulative effect of the base stations (theoretical analysis)," Tech. Rep. CPGPTD (10)036, French Contribution to CPG PT-D - Agenda Item 1.17, Apr. 2010.

[67] D. Setiawan, D. Gunawan, and D. Sirat, "Interference Analysis of Guard Band and Geographical Separation between DVB-T and E-UTRA in Digital Dividend UHF Band," *International Conference on Instrumentation, Communications, Information Technology and Biomedical Engineering 2009 (ICICI-BME 2009)*, November 2009.

[68] F. Khan, *LTE for 4G Mobile Broadband - Air Interface Technologies and Performance*, Cambridge University Press, 2009.

[69] Recommendation ITU-R BT.419-3, *Directivity and polarization discrimination of antennas in the reception of television broadcasting*, 1992.

[70] ITU, *Final Acts of the Regional Radiocommunication Conference 2006 (RRC-06)*, 2006.

[71] ITU-R JTG 5-6, *Studies on the use of the band 790-862 MHz by mobile applications and by primary services.*

[72] Recommendation ITU-R P.1546-4, *Method for point-to-area predictions for terrestrial services in the frequency range from 30 MHz to 3000 MHz*, 2009.

[73] L. Ferreira, M. Kuipers, C. Rodrigues, and L. M. Correia, "Characterisation of Signal Penetration into Buildings for GSM and UMTS," *IEEE International Symposium on Wireless Communication Systems 2006 (ISWCS 2006)*, September 2006.

[74] "A preliminary assessment of the feasibility of fitting new/future applications/services into non-harmonised spectrum of the digital dividend (namely the so-called "white spaces" between allotments)," Tech. Rep. CEPT Report 24 - Report C from CEPT to the European Commission, CEPT, Jun. 2008.

[75] "Technical and operational requirements for the possible operation of Cognitive Radio systems in the white spaces of the frequency band 470-790 MHz," Tech. Rep. ECC Report 159, CEPT, Jan. 2011.

[76] V. Degli Esposti, D. Guiducci, A. de' Marsi, P. Azzi, and F. Fuschini, "An advanced field prediction model including diffuse scattering," *IEEE Transactions on Antennas and Propagation*, vol. 52, no. 7, pp. 1717–1728, July 2004.

[77] F. Fuschini, H. El-Sallabi, V. Degli Esposti, L. Vuokko, D. Guiducci, and P. Vainikainen, "Analysis of Multipath Propagation in Urban Environment Through Multidimensional Measurements and Advanced Ray Tracing Simulation," *IEEE Transactions on Antennas and Propagation*, vol. 56, no. 3, pp. 848–857, March 2008.

[78] B. Evans, M. Werner, E. Lutz, M. Bousquet, and G. E. Corazza, "Integration of satellite and terrestrial systems in future multimedia communications," *IEEE Wireless Communications*, vol. 12, no. 5, pp. 72–80, May 2005.

[79] G. E. Corazza, P. Britten, I. Buret, N. Chuberre, A. Davies, N. Dimitriou, M. Neri, A. Polydoros, A. Vanelli-Coralli, and A. Bolea-Alamanac, "Defining the role of satellite communications in 4G," *World Wireless Congress 2007 (WWC07)*, May 2007.

[80] G. E. Corazza, *Digital Satellite Communications*, Springer, 2007.

[81] IEEE Std. 802.22, *IEEE Standard for Information Technology - Telecommunications and information exchange between systems. Wireless Regional Area Networks (WRAN) - Specific requirements, Part 22: Cognitive Wireless RAN Medium Access Control (MAC) and Physical Layer (PHY) Specifications: Policies and Procedures for Operation in the TV Bands.*, 2011.

[82] IEEE Std. 802.15.4a 2007, *Wireless medium access control (MAC) and physical layer (PHY) specifications for low-rate wireless personal area networks (LR-PANs).*, 2007.

[83] L. De Nardis and M.-G. Di Benedetto, "Overview of the IEEE 802.15.4/4a standards for low data rate Wireless Personal Data Networks," *Workshop on Positioning, Navigation and Communication 2007 (WPNC 2007)*, March 2007.

[84] A. Bastra, S. Lingam, and J. Balakrishnan, "Multi-band OFDM: A Cognitive Radio for UWB," *IEEE International Symposium on Circuits and Systems 2006 (ISCAS 2006)*, May 2006.

[85] D. Cabric, M. S. W. Chen, D. A. Sobel, J. Yang, and R. W. Brodersen, "Future Wirless Systems: UWB, 60 GHz and Cognitive Radios," *IEEE Custom Integrated Circuits Conference 2005 (CICC 2005)*, September 2005.

[86] M. Sherman, A. N. Mody, R. Martinez, C. Rodriguez, and R. Reddy, "IEEE Standards Supporting Cognitive Radio and Networks, Dynamic Spectrum Access, and Coexistence," *IEEE Communications Magazine*, vol. 46, no. 7, pp. 72–79, September 2008.

[87] S Haykin, "Cognitive radio: brain-empowered wireless communications," *IEEE Journal on Selected Areas in Communications*, vol. 45, no. 2, pp. 67–73, February 2005.

[88] I. F. Akyildiz, W.-Y. Lee, M. C. Vuran, and S. Mohanty, "NeXt generation/dynamic spectrum access/cognitive radio wireless networks: a survey," *Computer Networks*, vol. 50, pp. 2127–2159, May 2006.

[89] S. Kandeepan, A. Giorgetti, and M. Chiani, "Time-Divisional Cooperative Periodic Spectrum Sensing for Cognitive Radio Networks," *IEEE International Conference on Communication 2010 (ICC 2010)*, May 2010.

[90] T. Yucek and H. Arslan, "A Survey of Spectrum Sensing Algorithms for Cognitive Radio Applications," *IEEE Communications Surveys and Tutorials*, vol. 11, no. 1, pp. 116–130, First Quarter 2009.

[91] H. Urkowitz, "Energy Detection of Unknown Deterministic Signals," *Proceedings of the IEEE*, vol. 55, no. 4, pp. 523–531, April 1967.

[92] F. F. Digham, M.-S. Alouini, and M. K. Simon, "On the energy detection of unknown signals over fading channels," *IEEE International Conference on Communications 2003 (ICC 2003)*, May 2003.

[93] R. Tandra and A. Sahai, "Fundamental limits on detection in low SNR under noise uncertainty," *IEEE International Conference on Wireless Networks, Communications and Mobile Computing 2005 (WIRELESSCOM 2005)*, June 2005.

[94] Y. Zhao, L. Morales, J. Gaeddert, K. Bae, J.-S. Um, and J. Reed, "Applying radio environment maps to cognitive wireless regional area networks," *IEEE International Symposium on New Frontiers in Dynamic Spectrum Access Networks 2007 (DySPAN 2007)*, April 2007.

[95] T. Bashar and G. J. Olsder, *Dynamic Noncooperative Game Theory*, Society for Industrial & Applied Mathematics,U.S.; 2nd Revised edition, Classics in Applied Mathematics, 1987.

[96] "Notice of inquiry and notice of proposed rulemaking," Tech. Rep. FCC ET Docket no. 03-237, Federal Communications Commission, Nov. 2003.

[97] Recommendation ITU-R S.465-6, *Reference radiation pattern for earth station antennas in the fixed-satellite service for use in coordination and interference assessment in the frequency range from 2 to 31 GHz*, 2010.

[98] D. Stoyan, W. S. Kendall, and J. Mecke, *Stochastic Geometry and its Applications*, John Wiley & Sons, Inc., 2nd edition, 1995.

[99] B. A. Fette and B. Fette, *Cognitive Radio Technology*, Newnes, 2006.

[100] F. H. P. Fitzek and M. D. Katz, *Cognitive Wireless Networks - Concepts, Methodologies and Visions Inspiring the Age of Enlightenment of Wireless Communications*, Springer, 2007.

[101] E. Hossain, D. Niyato, and Z. Han, *Dynamic Spectrum Access and Management in Cognitive Radio Networks*, Cambridge University Press, 2009.

[102] R. V. Prasad, P. Pawelczak, J. A. Hoffmeyer, and H. S. Berger, "Cognitive functionality in next generation wireless networks: standardization efforts," *IEEE Communications Magazine*, vol. 46, no. 4, pp. 72–78, April 2008.

[103] IEEE Std. 1900.1-2008, *Standard Definitions and Concepts for Dynamic Spectrum Access: Terminology Relating to Emerging Wireless Networks, System Functionality, and Spectrum Management*, 2008.

[104] A. Ghasemi and E. S. Sousa, "Collaborative spectrum sensing for opportunistic access in fading environment," *IEEE International Symposium on New Frontiers in Dynamic Spectrum Access Networks 2005 (DySPAN 2005)*, November 2005.

[105] J. Ma, G. Y. Li, and B. H. Juang, "Signal Processing in Cognitive Radio," *Proceedings of the IEEE*, vol. 97, no. 5, pp. 805–823, May 2009.

[106] A. Sahai, N. Hoven, and R. Tandra, "Some fundamental limits in cognitive radio," *Allerton 2004 Conference on Communications, Control and Computing*, October 2004.

[107] J. Proakis, *Digital Communications*, McGraw-Hill Book Company, Inc., 2000.

[108] A. V. Dandawate and G. B. Giannakis, "Statistical tests for presence of cyclostationarity," *IEEE Transactions on Signal Processing*, vol. 42, no. 9, pp. 2355–2369, September 1994.

[109] W. A. Gardner, "Exploitation of spectral redundancy in cyclostationary signals," *IEEE Signal Processing Magazine*, vol. 8, no. 4, pp. 14–36, April 1991.

[110] S. Shankar, "Spectrum agile radios: utilization and sensing architectures," *IEEE International Symposium on New Frontiers in Dynamic Spectrum Access Networks 2005 (DySPAN 2005)*, November 2005.

[111] G. Ganesan and Y. G. Li, "Cooperative spectrum sensing in cognitive radio networks," *IEEE International Symposium on New Frontiers in Dynamic Spectrum Access Networks 2005 (DySPAN 2005)*, November 2005.

[112] J. Zhao, H. Zheng, and G.-H. Yang, "Distributed coordination in dynamic spectrum allocation networks," *IEEE International Symposium on New Frontiers in Dynamic Spectrum Access Networks 2005 (DySPAN 2005)*, November 2005.

[113] S. M. Mishra, A. Sahai, and R. W. Brodersen, "Cooperative sensing among cognitive radios," *IEEE International Conference on Communications 2006 (ICC 2006)*, June 2006.

[114] G. Ganesan and Y. G. Li, "Cooperative spectrum sensing in cognitive radio - Part I: Two user networks," *IEEE Transactions on Wireless Communications*, vol. 6, no. 6, pp. 2204–2213, June 2007.

[115] G. Ganesan and Y. G. Li, "Cooperative spectrum sensing in cognitive radio - Part II: Multiuser networks," *IEEE Transactions on Wireless Communications*, vol. 6, no. 6, pp. 2214–2222, June 2007.

[116] T. X. Brown, "An analysis of unlicensed broadcast service bands," *IEEE International Symposium on New Frontiers in Dynamic Spectrum Access Networks 2005 (DySPAN 2005)*, November 2005.

[117] B. Wild and K. Ramchandran, "Detecting the primary receivers for cognitive radio applications," *IEEE International Symposium on New Frontiers in Dynamic Spectrum Access Networks 2005 (DySPAN 2005)*, November 2005.

[118] Uk Office of Communications (Ofcom), *Digital Dividend: cognitive access. Statement on license-exempting cognitive devices using interleaved spectrum*, 2009.

[119] H. Kim and K. G. Shin, "Efficient discovery of spectrum opportunities with MAC-layer sensing in cognitive radio networks," *IEEE Transactions on Mobile Computing*, vol. 7, no. 5, pp. 533–545, May 2008.

Acknowledgements

This thesis is the tangible result of a three years work, but not the only one. Thanks to the many people who where close to me, I had the possibility to grow from a professional and human point of view, much more than I thought I would have when I accepted this challenge.

I am deeply grateful to my supervisor, Professor Giovanni E. Corazza, who trusted in me and my work, giving me the possibility of undertaking this research path in my life. His passion and guidance were extremely inspiring, and allow me to say that he really is an incredible motivator, being able of exploiting the best from all the people working with him, in a perfect combination of cheerfulness and devotion to work.

I would also like to thank Ing. Guido Riva, my supervisor in Fondazione Ugo Bordoni, the body funding my research activity and hosting me for most of these three years. Few people would have given such a trust to a young researcher to be the Italian Administration representative in several European meetings. This, and his wise advices, gave me the possibility of improving my skills and helped me advancing on the path to professional growth.

A Ph. D. activity is not an easy road to be covered, but thanks to all my friends and colleagues it was a real pleasure even in the toughest moments. Some of them have chosen different paths, while some others are still working here. A special and sincere thanks goes to Alberto Candreva, Lina Deambrogio, Giulio Gabelli, Francesco Bastia, Valeria Petrini, Alice Masini, Stefano Rosati, Marco Papaleo, Claudio Palestini, and Valentina Pullano, who made the offices in DEIS and FUB a really fun place, and also gave an invaluable technical support whenever needed. There are so many people to mention, that I really hope to remember all of them: Alessandro Vanelli-Coralli, Stefano Cioni, Francesco Lombardo, Riccardo Baroni,

Ilaria Thibault, Daniele Tarchi, and Rosalba Suffritti in the Digicomm group, and Doriana Guiducci, Franco Fuschini, Paolo Grazioso, Claudia Carciofi, Fides Daltri, Maria Missiroli, Simona Valbonesi, Marina Barbiroli, Andrea Neri, Vittorio Degli Esposti, Gabriele Latte, Luna Pagani, Andrea Garzia, Francesco Morandi, Francesco Fortunato, and Enrico Tarantino in FUB. Thank you all.

My Ph. D. activity also allowed me to work for six months in SUPELEC (Paris), under the precious guidance of Dr. Marco Di Renzo. A very pleasant person, who taught me so many things that I can barely believe I actually learned them. He is always extremely helpful, and I am really glad to be both friend and colleague with him. I am sincerely looking forward to keep working with him.

During my stay in Paris, I also had the possibility to meet a lot of nice people, who gave me some very funny moments and made me feel at home. A special thanks goes to Lana Iwaza, a very kind and genuine person who is always ready to give very good advices and support, and to Cristina Merola, Michela Iezzi, Mael LeTreust, Nabil Mohammed El Korso, and all the other guys at SUPELEC for the nice moments they gave me.

I would like to express my gratitude also to Professor Gabriele Falciasecca, for allowing me to be his assistant in the course of Electromagnetic Propagation in the Master Degree course of Telecommunications Engineering.

A fundamental step for the proper finalization of a Ph. D. thesis is a thorough review of the assumptions, methodologies, and results which are proposed in it. Thus, a sincere thanks goes to Professor Moe Z. Win and Professor Jocelyn Fiorina, who kindly accepted to be the reviewers of my work.

Least, but definetly not last, my deepest gratitude goes to my parents, Marisa and Gianni, who always unconditionally supported me and my choices, giving me the possibility to pursue my dreams. Their warm and guidance made me the person who I am now. I would also like to thank from my heart my girlfriend Martina, for her love, help and patience during all these years together, and for facing all the difficulties in such a long path side-by-side.